© 2019 Yaqing Jin

# ON THE DYNAMICS OF RIGID AND FLEXIBLE STRUCTURES UNDER COMPLEX FLOWS

BY

YAQING JIN

DISSERTATION

Submitted in partial fulfillment of the requirements
for the degree of Doctor of Philosophy in Mechanical Engineering
in the Graduate College of the
University of Illinois at Urbana-Champaign, 2019

Urbana, Illinois

Doctoral Committee:

Assistant Professor Leonardo P. Chamorro, Chair
Professor Joseph Bentsman
Associate Professor Randy H. Ewoldt
Assistant Professor Jinhui Yan

# ABSTRACT

Fluid-structure interaction (FSI) is a ubiquitous phenomenon of high relevance in engineering systems. During the past decades, substantial efforts have been placed on characterizing the dynamics of structures under a wide range of flow. However, associated phenomena under turbulence are poorly understood. Quantitative description of the non-linear, multiscale interaction between structure dynamics and flow remains as an outstanding open problem in science and engineering. Uncovering the dominant mechanisms modulating the dynamics of flow and structures would allow to significantly improve the design, reliability and life span of a wide range of engineering systems. This thesis aims to contribute in that direction by presenting experimental and theoretical results of selected FSI problems, which addressed the role of structure geometry, stiffness and flow. They include the oscillations of slung prisms, passive and active splitter pitching in the wake of cylinders, the effect of directional stiffness, and the unsteady dynamics of wall-mounted flexible plates, which are briefly summarized as follows.

The pendulum-like oscillation and pitching patterns of cubic and rectangular slung prisms were inspected for two aspect ratios at various Reynolds numbers $Re$ under two freestream turbulence levels. The results show that the dynamics of the prisms can be characterized by two distinctive regions depending on the prism shape. Specifically, in the case of cubic prism the regions are defined by the growth rate of the pitching amplitude, whereas the dynamics of the rectangular prism is more sensitive to the angle of attack. In particular, when the large side initially faced the flow, the regions were defined by the synchronization between the vortex shedding and pure oscillations under very low turbulence. When the smaller side initially faced the flow, the regions were defined by the equilibrium pitching position. Regardless of the geometry of the prism and flow condition, the dominating oscillation frequency resulted close to the natural frequency of the small-amplitude

pendulum-like oscillation.

The distinctive pitching of hinged splitters in the trailing edge of elliptic cylinders was experimentally studied at various angles of attack ($AoA$) of the cylinder, Reynolds numbers and splitter lengths of the cylinder and freestream turbulence levels. Results show that the motions of the splitters contained dominating modes, $f_p$ and $f_v$, which were induced by the mean flow and wake dynamics. High background turbulence dampened the coherence of the regular vortex shedding leading to negligible $f_v$. For a sufficiently long splitter, namely twice the semimajor axis of the cylinder, dual vortex shedding mode occurred close to the leading and trailing edges of the splitter. In general, the splitters oscillated around an equilibrium position nearly parallel to the mean direction of the flow; however, a skewed equilibrium was also possible with a strong recirculation region.

The flow and drag induced by active pitching of plates in the wake of a cylinder of diameter $d$ were experimentally studied for various plate lengths $L$ as well as pitching frequencies $f_p$ and amplitudes $A_0$. Results show the distinctive effect of the active pitching on these quantities. In particular, flow recovery was significantly modulated by $L$, $f_p$ or $A_0$. Specific pitching settings resulted in the wake with dominant meandering patterns and faster flow recovery. We defined a modified version of the amplitude-based Strouhal number of the system $St_S$ to account for the effect of the cylinder in the active pitching. It characterized the drag coefficient $C_d$ across all the cases studied, and revealed two regions intersecting at a critical value of $St_S \approx 0.2$. Below this value, the $C_d$ remained nearly constant; however, it exhibited a linear increase with increasing $St_S$ past this critical point. Inspection of the integral momentum equation showed the dominant role of the velocity fluctuations in modulating $C_d$ past the critical $St_S$.

Flow-induced dynamics of flexible structures is, in general, significantly modulated by periodic vortex shedding. My work shows that for structures with directional stiffness, *Kármán* vortex shedding may dominate the wake of bodies governed by the natural frequency. This phenomenon can be a consequence of Kelvin-Helmholtz ($K-H$) instability, where the structural characteristics of the body dominate the oscillations. In addition to a single structure, the dynamics of two rectangular, flexible plates of low aspect ratio $h/b$ (height/width = 4) was experimentally investigated in tandem arrangements under uniform flows at various Cauchy numbers $Ca \in [15,\ 77]$, and spacing $s_x = \Delta x/h = 0.5,\ 1$ and 2. Results show that the oscil-

lations of the upstream plate were dominated by its natural frequency. However, the motions of the downstream plate were significantly modulated by the induced flow and coherent motions shed from the upstream structure. Despite that the intensity of the oscillations of the upstream plate increased monotonically with $Ca$, this was not the case for the downstream plate at $s_x = 1$ and 2 due to flow fluctuations, vortex shedding and large structure deformation. As a result, it exhibited a local minimum. Supported with measurements, a mathematical model was derived to quantitatively explain this behavior.

The unsteady dynamics of wall-mounted, flexible plates under inclined flows was fundamentally described using theoretical arguments and laboratory experiments under various Cauchy numbers $Ca = \rho_f b L^3 U_0^2/(EI) \in [8, 83]$ (where $\rho_f$ is the fluid density, $b$ and $L$ are the plate width and length, $U_0$ is the incoming velocity, $E$ is the Young's modulus and $I$ is the second moment of the area) and inclination angles $\alpha$. Three-dimensional particle tracking velocimetry and high-resolution force sensor were used to characterize the evolution of the plate dynamics and aerodynamic force. We show the existence of three distinctive, dominant modes of tip oscillations, which are modulated by the structure dynamic and flow instability. The first mode is characterized by small-amplitude, planar fluttering-like motions occurring under a critical Cauchy number, $Ca = Ca_c$. Past this condition, the motions were dominated by the second mode consisting on unsteady twisting superimposed to the fluttering patterns. The onset of this mode was characterized by a sharp increase of the force fluctuation intensity. At sufficiently high $Ca$ and $\alpha$, the plate may undergo a third mode given by large-scale tip orbits about the mean bending. Using the equation of motion and first-order approximations, we propose a formulation to estimate $Ca_c$ as a function of $\alpha$; it exhibits solid agreements with experiments.

*To my parents, wife and my child coming soon*

# ACKNOWLEDGMENTS

I would like to sincerely thank my advisor, Dr. Leonardo P. Chamorro, who encouraged me all the way during my Ph.D work, helped me establish my confidence to become a creative researcher and continue my research after graduation as a faculty. In addition to the knowledge and experimental skills, he always gave me the greatest trust and encouragement even I was in trouble to finish my first paper. Without him, I could not stick to my dream and become an assistant professor after graduation.

Many people contributed to the work, and I would like to express my gratitude to everyone involved. Thanks to all my labmates, especially my collaborators, Jin-Tae Kim, Ali Hamed, Nicolas Tobin, Sheng Ji, Boshen Liu, Huiwen Liu, Imran Hayat, Zhongyu Mao, Shifeng Fu, and many others not mentioned here. My work could not be finished without their help and support. I would like also to thank the help from many professors both in UIUC MechSE Department and other universities, who provided valuable guidance for my research work. I would like to thank for the support from Yee fellowship and Fluids travel award, which was great encouragement for my research. Thank you to my parents and my wife, who always gave me the greatest support when I encountered difficulties, and my child coming soon, who will illuminate my way forward.

# TABLE OF CONTENTS

# CHAPTER 1

# INTRODUCTION

Flow-induced motion (FIM) of rigid and flexible bodies has been the focus of numerous studies during the last decades due to its relevance in nature and various engineering fields. Particular examples include energy harvesting using passive flapping flat plates [1], plate tumbling under free flight [2], the control of rotations in rectangular prisms [3, 4], the reconfiguration of vegetation and its impact on mixing and transport processes [5, 6], among many others. During the past decades, substantial research has focused on characterizing the dynamics of structures under a variety of flows; however, the description of FIM under turbulence is far from being well understood. It is acknowledged that turbulence level can significantly modulate the loads on structures and, therefore, it may lead to unsteady motions with patterns substantially different from those under low turbulence [7, 8, 9]. Understanding the non-linear, multiscale mechanisms modulating the dynamics of flow and structures would allow to significantly improve the design, reliability and life span of a wide range of systems ranging from deep-sea pipelines [10] to wind farms [11], as well as environmental and industrial processes such as mixing and heat transfer [12], among others.

## 1.1 Motivation

This dissertation is motivated by the pressing needs to better characterize and quantify the FIM in problems related to:

1. The scale-to-scale interaction between turbulence and structure dynamics.
2. The multiscale oscillations of wall-mounted, flexible structures under complex flows.

Addressing the first problem may provide significant insight into the design of engineering structures facing unsteady flows. In nature and many engineering applications, turbulence plays a central role in modulating the unsteady forces on structures, in the wake mixing and heat-transfer enhancement. During the last decades, investigations have pointed out distinct effects in various scenarios. Early work by Lee [13] noted that the distribution of the surface pressure on a 2D square prism can be highly influenced by the incoming turbulence level. Later work by Tamura and Miyagi [7] found similar phenomenon for structures with other geometries, including square cylinders with various corner shapes and rectangular cylinders [8, 14]. They pointed out that the incoming turbulence level may alter the time-averaged lift or drag forces, and significantly change the unsteady forces and the vortex shedding. Figure 1.1 shows an example of the normalized streamwise velocity distribution of flow over an inclined elliptic cylinder under low and relatively high incoming turbulence. Despite the same structure geometry and Reynolds number, the turbulence leads to much faster wake recovery and, therefore, smaller recirculation region in the wake.

Due to the modulation of turbulence on the time-averaged and unsteady forces on structures, it is expected that turbulence also modulates the motion of flexible structures. This is the case of the vortex-induced vibrations of circular cylinders,

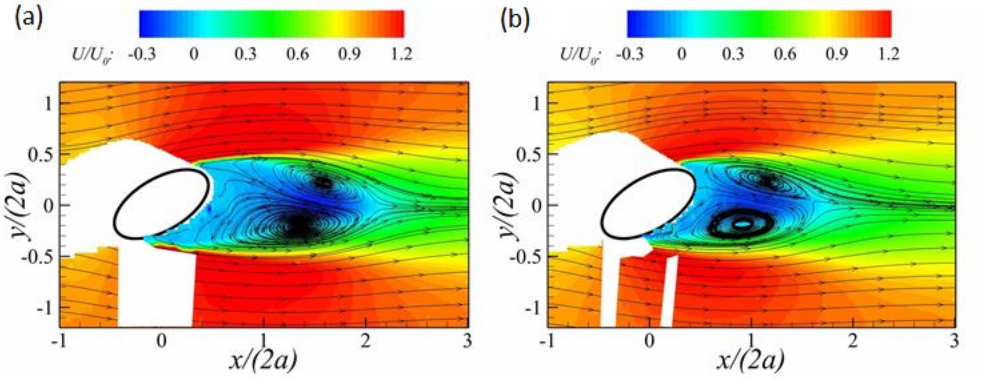

Figure 1.1: Normalized streamwise velocity distribution of flow over an inclined elliptic cylinder under incoming turbulence of a) $I_u = 0.2\%$; b) $I_u = 6.5\%$.

which are different under laminar and turbulent flows [9]. Structures may exhibit multiscale dynamics; in such cases, the role of turbulence remains unclear. Characterization turbulence effects may provide significant insight on the structure design and control strategies to reduce or increase the unsteady forces.

The second problem is related to the deformation and oscillation of vegetation-like structures under wind/water loads. Aquatic vegetation or flexible canopies increases wall resistance, promotes sedimentation and reduces erosion [15, 5]. These phenomena are highly coupled with the geometry, stiffness as well as the unsteady motions of the structures. Unlike rigid bodies, flexible structures may undergo significant deformation under sufficiently high flows (Figure 1.2). In such cases, the drag force and the wake characteristics may be very different from the rigid counterparts [16, 17, 18, 5]. Deformed canopies may, in return, alter the flow and transport of scalars (e.g., nutrients and sediments in the case of vegetation). During the last decades, extensive efforts have focused on predicting the mean deformation of wall-mounted flexible plates with various geometries and incoming flows. Particular effort has been placed in characterizing the so-called Vogel exponent in the drag-velocity

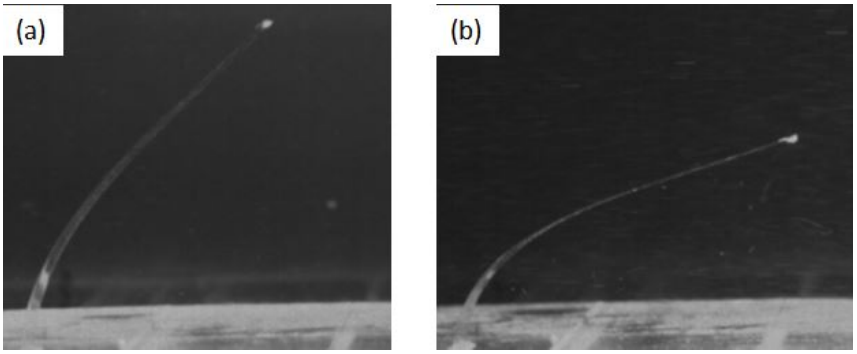

Figure 1.2: Raw image for the deformation of a flexible plate within NaI aqueous solution under incoming velocity of a) 0.24 m s$^{-1}$; b) 0.54 m s$^{-1}$.

relation.

In addition to the mean deformation, a flexible structure may oscillate around its bending equilibrium. Compared to the static structure bending, the oscillation may lead to accelerated material fatigue. The frequency and amplitude of structure oscillation are highly influenced by the structure stiffness, wake fluctuation intensity and frequency; such unsteady motions are also unclear.

## 1.2 Objectives and Overview

In this thesis, the distinct role of turbulence on the dynamics of rigid and flexible structures was systematically explored under a broad parameter space. Laboratory experiments were conducted to characterize the motion of various structures, the wake dynamics and the unsteady forces. Specific configurations included oscillations of slung loads and flexible plates as well as splitter pitching. Particle Image Velocimetry (PIV), Particle Tracking Velocimetry (PTV), telemetry, force balance and hotwire anemometry were used to investigate the structure motion and induced flow. Theoretical arguments are also included for completeness.

The thesis provides new fundamental understanding of selected problems of high relevance in engineering related to the dynamics of structures and associated wakes under turbulence. The uncovered phenomena complements our knowledge of related phenomena under laminar and negligible turbulence. The focus is placed on Reynold numbers $Re \sim \mathcal{O}(10^3 - 10^4)$, where the inertia dominantes over viscous forces. Analysis includes the inspection of first and second order statistics, turbulence kinetic energy budget and spectral analysis. Higher-order statistics and moments as well as inspection of modal decomposition is left for future works.

The thesis is organized as follows. Chapter 2 provides a literature review and discusses general problems in FIM. Chapter 3 describes the dynamics of three-dimensional slung loads. Chapter 4 and 5 discuss the passive and active pitching of cylinder-splitter assemblies. Chapter 6, 7 and 8 summarize the work on the FIM of wall-mounted flexible plates. Remarks and the path for the future work are given in Chapter 9.

# CHAPTER 2

# LITERATURE REVIEW

## 2.1 Flow-induced Oscillation, pitching and rotation of structures

Flow induced oscillation (FIO) and flow induced pitching (FIP) are two particular cases within the FIM set, where vortex shedding from the structure may play a major role on the dynamics. An example of FIO is the unsteady lift induced by the von *Kármán* vortices on cylinders [20, 21]. Structures with rectangular cross section may exhibit very complex patterns across angles of attack. Zhao [22] reported that for the oscillation of 2D rectangular cylinders under very low Reynolds numbers ($Re$ ~200), the thickness ratio can significantly influence the vortex shedding. Recent experiments conducted by Nemes *et al*. [23] and Zhao *et al*. [24] showed the distinctive vortex patterns on the FIO of a square cylinder (Figure 2.1), which vary as a function of angle of attack relative to the incoming flow. The FIP is induced by the net torque from the surface pressure distribution of structures facing the flow. This phenomenon has been explored in e.g., flat plates, airfoils and rectangular prisms. Early studies by Theodorsen [25] and Karman [26] investigated the small-amplitude pitching motions using potential flow theory. Recent work by Jantzen *et al*. [27] and Baik *et al*. [28] pointed out that the reduced frequency $k = \pi f_p c/U$, with $c$, $f_p$ and $U$ representing the chord length of plate, pitching frequency and in-

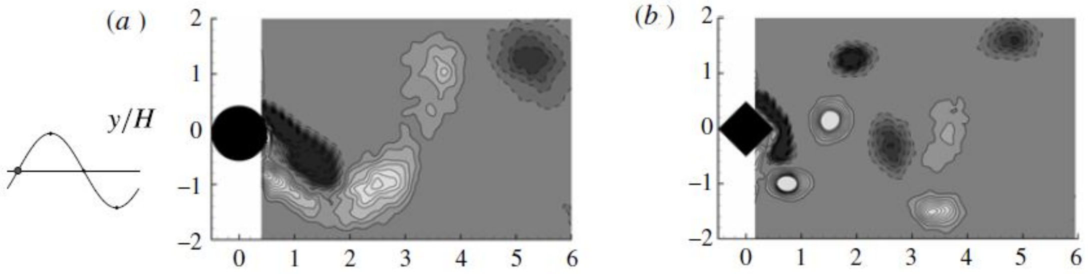

Figure 2.1: Comparison of vortex shedding modes between a circular cylinder (a) and a square structure (b); adapted from [29].

coming flow velocity, play a key role in the pitching and wake characteristics (Figure 2.2).

Most of the fundamental studies on FIM have focused on the dynamics of structures under very low turbulence, where low-order periodic oscillations/rotations dominate [30, 31, 32, 33]. Comparatively, the motion of structures under high-turbulence levels have received much less attention. As pointed out by various studies [34, 7, 35], turbulence can significantly influence the frequency and magnitude of the forces and the dynamic characteristics of the structures. So *et al.* [36] found that the vortex shedding frequency and the natural frequency of elastic cylinders dominate under freestream turbulence. Recent numerical studies on the oscillation of a rectangular cylinder suggest that turbulence can significantly diminish the amplitude of oscillation [37]. Akaydin *et al.* [38] investigated the potential of energy harvesting using a piezoelectric cantilever beam in a turbulent boundary layer. They reported that matching the predominant frequency of flow with the natural frequency of the structure can maximize the power output. Hobeck and Inman [39, 40] used the frequency domain to investigate the oscillation of flexible structures under turbulent flow.

Rotation under turbulence (RT) is another distinctive phenomenon within the

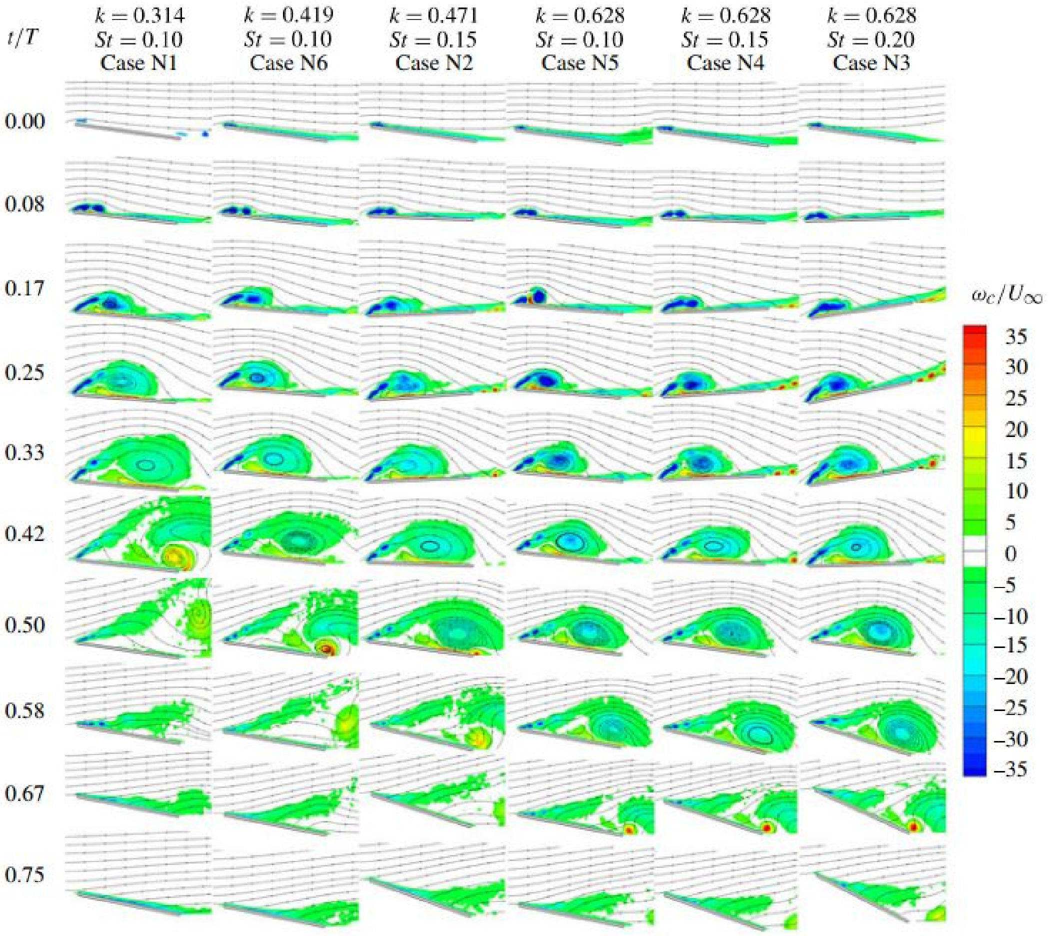

Figure 2.2: Normalized vorticity contours for pitching aerofoils at various conditions and instants; adapted from [28].

FIM set. Two common types of rotations are those with the axis of rotation either perpendicular or parallel to the mean flow. Cases with the axis perpendicular to the flow can be triggered via either the thrust generated from the aerodynamic forces, e.g. vertical wind turbines [41, 42], or via the vortex shedding from the edge of the structures, e.g. autorotations of flat plates [43, 44]. Among the most distinctive examples of structures rotating with axis parallel to the mean flow include the horizontal-axis wind turbines [45, 46]. Chamorro *et al.* [47] reported the nonlinear relationship of the energy cascade between the turbulence and the power output of a 2.5 MW wind turbine. Recently, a tuning-free model between the energy spectrum of the flow and power output was proposed by Tobin *et al.* [48], which was validated with turbine sizes ranging from laboratory models to MW scales. Milan *et al.* [49] investigated the power fluctuations of wind farm, showing that for large time scales, the power dynamics follow a turbulent energy cascade $\propto f^{-5/3}$ in the a frequency range. These studies offer insight into the response of rotational structures under turbulence and their relation with the turbulence energy cascade.

## 2.2 Flow-induced dynamics of slung prisms

Although substantial efforts have been placed on characterizing FIM on 2D structures, those on 3D bluff bodies has received comparatively much less attention. Complex motions with simultaneous flow-induced oscillations (FIO) and flow-induced pitching (FIP) are common in these cases, where the Strouhal number $St$ exhibits variability due to the local aspect ratio facing the flow [50]. Of particular interest in engineering is the case involving carrying slung loads by helicopters or cranes. Helicopters are widely used to move loads. Examples include fire-fighting, searching and rescuing, and transportation, among others (figure 2.3). Suspended loads

Figure 2.3: Flight test with full-scale slung loads; adapted from [52].

with various geometries and weights are commonly carried by cranes in harbors and construction sites. Due to the unsteady motions of helicopters and wind, suspended loads can impose distinct dynamic forces to the carriers, which accounts for more than 10% of helicopter accidents [51].

In general, suspended structures exhibit highly-coupled pitching and pendulum-like oscillations. Extensive efforts have focused on uncovering the mechanisms modulating the structure motions using wind tunnel and flight tests. Raz *et al*. [53] conducted both wind-tunnel and flight tests with a rectangular slugged container and analyzed the stability of the dynamics with passive vertical fins. Greenwell [3] measured the rotations of low-aspect-ratio rectangular prisms and reported the 'lock in' and hysteresis phenomena. Raz *et al*. [52] investigated the dynamics of slug cargoes from an helicopter and focused on the influence of helicopter motion and departure of the center of gravity. Cicolani *et al*. [4] used slow pitching motions as a mechanism to suppress the pendulum-like oscillations of slung loads. Using a numerical approach, Prosser and Smith [54] explored the 3D aerodynamics of prismatic bodies and circular cylinders, and pointed out that shear layer reattachment dominates the mean forces and moments of bluff bodies. Prosser and Smith [55]

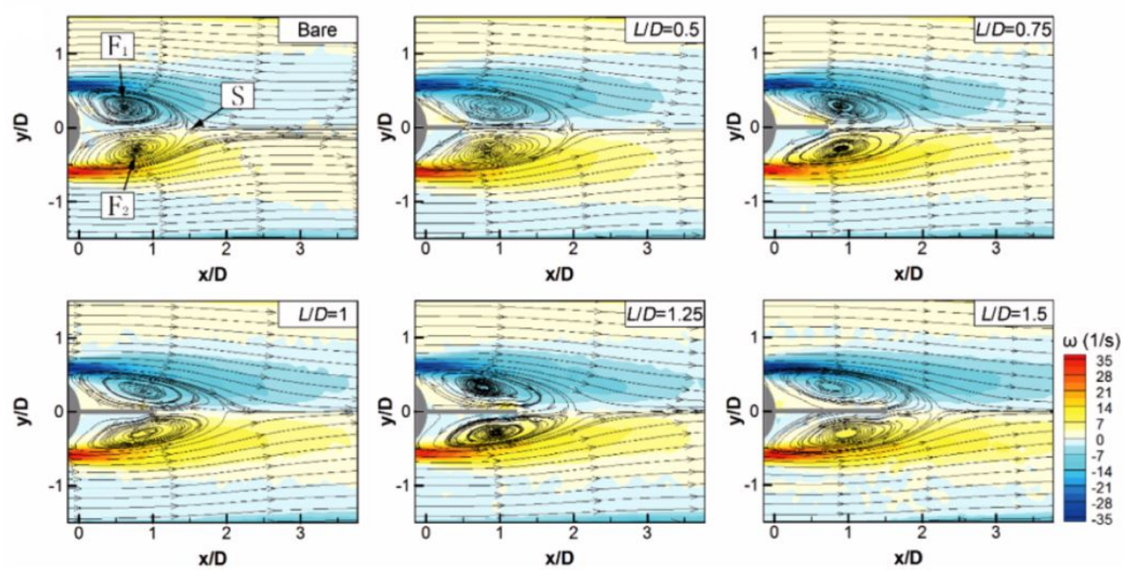

Figure 2.4: Time-averaged vorticity contours and streamlines downstream of a cylinder at $Re = 3000$; adapted from [56].

proposed a physical-based, reduced-order aerodynamics model for predicting the motions of bluff bodies.

## 2.3 Passive/active splitter pitching under complex flow

Quantitative characterization of the aerodynamic force on rigid and flexible bodies is undoubtedly of paramount importance in many engineering applications. A canonic, well-documented example is the flow around circular cylinders; there, unsteady lift and drag are modulated by periodic vortex shedding known as von *Kármán*. Such forcing usually results in vibrations and fatigue of structures [20, 21, 57], which lead to shorter life span. Consequently, damping of the vortex shedding is conceptually a good strategy to reduce the fluctuations of the lift and stress on structures.

Fixed splitters placed in the near wake of cylinders have been studied as a passive

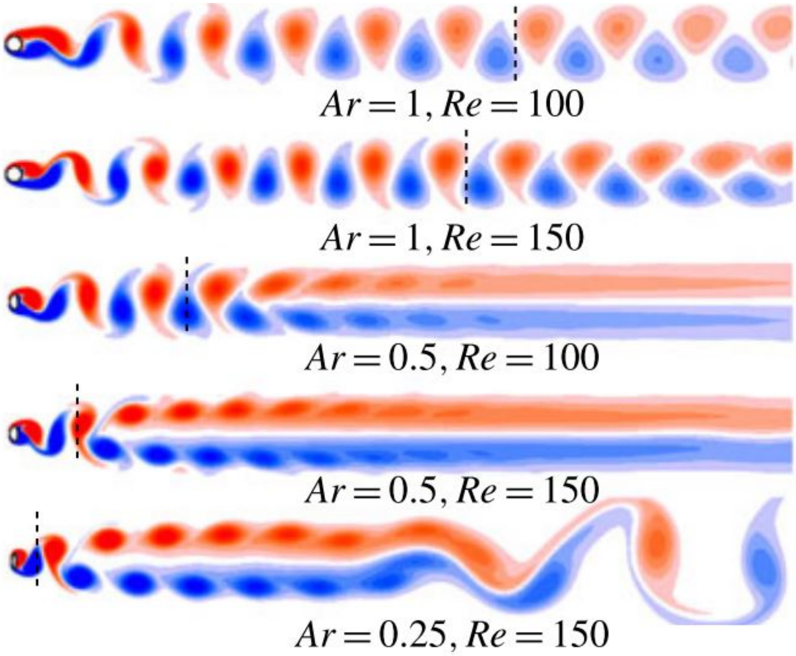

Figure 2.5: Instantaneous vortex distributions of flow over elliptic cylinders at various aspect ratios and $Re$; adapted from [58].

strategy to reduce vortex shedding. Early experimental investigation by Roshko [59] showed that a splitter with a length ($c$) of 5 times the diameter of a cylinder ($d$) is effective to significantly suppress the periodic vortices. Apelt & West [60] reported that the Strouhal number $St$ is sensitive to structures with splitters of $c/d \leq 2$. Numerical studies by Hwang and Yang [61] showed drag reduction and decrease of the stagnation pressure with dual splitter configuration; one located upstream and the other placed downstream of a circular cylinder. In addition to damping the unsteady force on cylinders, attached splitters modify the wake flow. Mat *et al.* [62] explored the effect of splitters near square cylinders at low Reynolds numbers $Re$. They showed that short splitters (say $c/h < 1$, where $h$ is the side length of the square cylinder) delay the formation of vortex street, whereas relatively long splitters ($1.25 < c/h < 4.75$) may induce secondary vortices near the splitter tip. Ogunremi & Sumner [63] investigated the wake recovery of a cylinder-splitter system, and found an increase of the velocity deficit with longer splitters at $x/d > 4$, where $x$ is the downstream distance from the cylinder. Recent experiments by Liu *et al.* [56] showed that splitter can influence the distributions of vortices and reduce the turbulence kinetic energy along the wake axis (figure 2.4).

Elliptic cylinders can be thought as intermediate geometries between flat plates and circular cylinders with aspect ratios $AR = b/a \in (0, 1)$, where $b$ and $a$ are the semi-minor and semi-major axes. The flow-induced force on these structures and associated wake characteristics are functions of $AR$ and angle of attack ($AoA$). Here, the vortex shedding from both leading and trailing edges can result in additional unsteadiness in the drag ($D$) and lift ($L$) forces [64]. Modi *et al.* [65] reported that for Reynolds numbers $Re \in O(10^4)$, the drag and lift coefficients, $C_d$ and $C_L$, remain nearly constant. A recent study by Thompson *et al.* [58] showed that with the major axis perpendicular to the flow, a decrease of AR leads to the occurrence of parallel vortex shedding closer to the cylinder (figure 2.5). The understanding of fluid-structure feedback mechanism of flow past elliptical bodies with splitters may provide insight on locomotion, control of dynamic loading in structures, pipeline design and flow mixing, among others.

In addition to modulating wake flows and drag, splitters may also induce lift/drift force via deflection with respect to the mean flow. The lift of an isolated plate in pre-stall condition is proportional to the inclination angle relative to the incoming flow [67, 68, 69]. When a deflected plate is placed in the wake of a circular cylinder, the symmetry of the surrounding flow is broken; this results in pressure difference between the lateral sides of the body-splitter assembly [70, 71]. Assi *et al.* [72] pointed out that a free-to-rotate splitter attached to a circular cylinder may induce

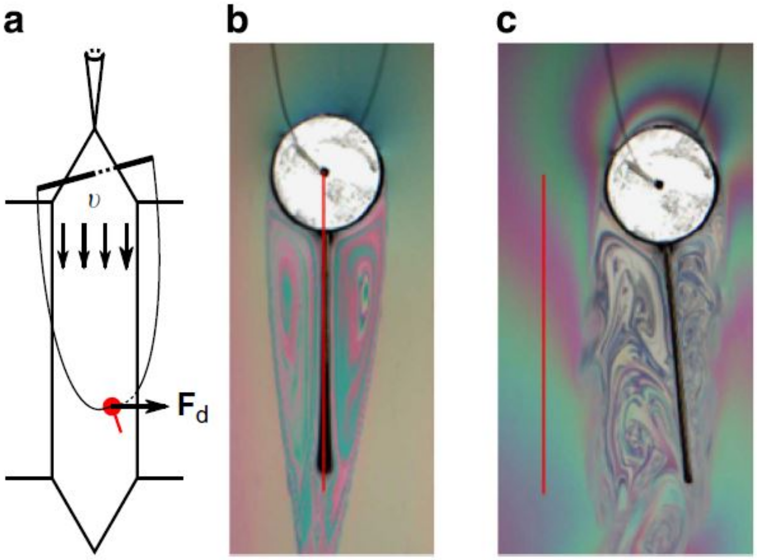

Figure 2.6: a) Schematic of the soap-film for flow over a freely hanging splitter in the wake of a circular cylinder; b) equilibrium plate position at wake centerline; c) same as b) but equilibrium at the right side of the cylinder; adapted from [66].

mean lift in the direction of the deflection. Bagheri *et al*. [73] showed that a passive filament hinged in the rear side of a bluff body immersed in a stream can generate a net lift without mean drag increase. Recent works reported that objects with a protrusion in a separated flow may drift sideways by exploiting a symmetry-breaking instability similar to that of an inverted pendulum [66, 74] (figure 2.6).

Unlike passive controls, active flow strategies may offer the possibility of local tuning of the flow to manipulate specific phenomena. One of those strategies has considered the forced oscillations on circular cylinders to reduce the mean drag, where the efficiency of this mechanism appears to be highly dependent on the Reynolds number *Re* [76, 77]. Other concepts aiming to control the vortex shedding and flow-induced force on cylinders include streamwise and transverse oscillations [78], suction and blowing [79] and synthetic jets [80]. Active pitching of plates has been used to induce propulsive force and locomotion. Wake and force resulting from ac-

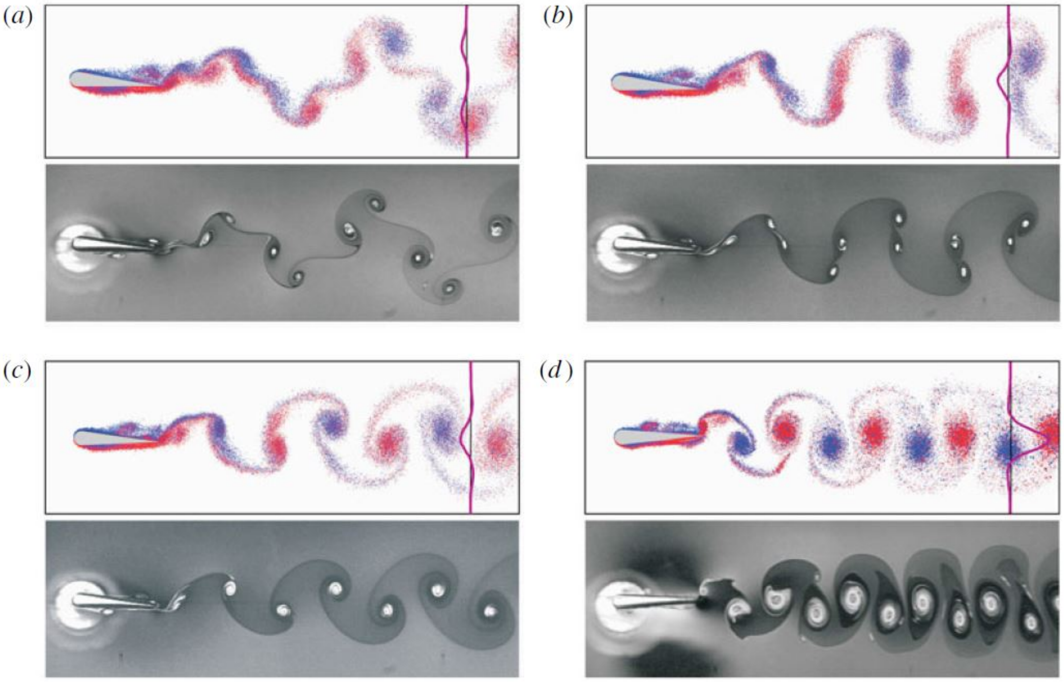

Figure 2.7: Numerical and experimental results for wakes of a pitching foil with various vortical patterns. a) 2P vortices; b) 2P vortices that evolve to von Kármán vortices; c) von Kármán vortices; d) inverted von Kármán vortices; adapted from [75].

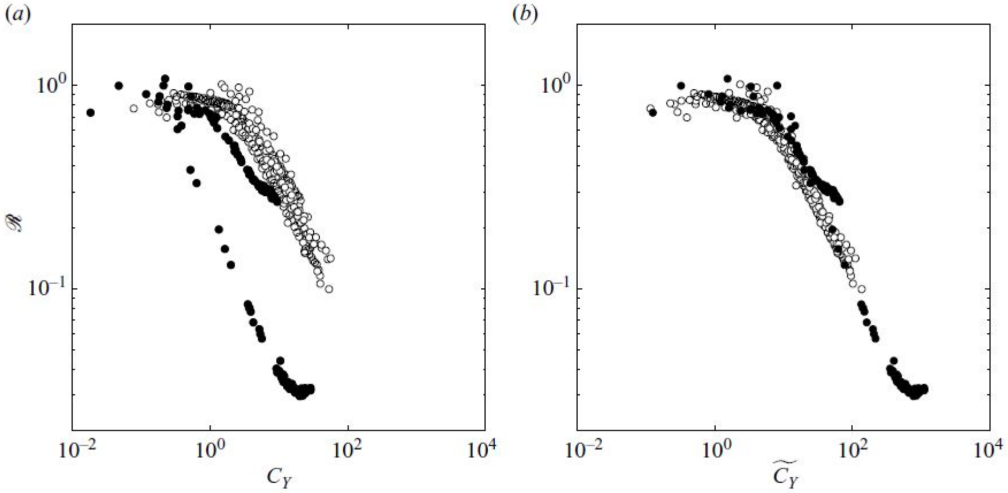

Figure 2.8: Evolution of drag coefficient versus Cauchy number (a) and scaled Cauchy number (b); adapted from [18].

tive pitching of airfoils have been explored numerically and experimentally. Bohl and Koochesfahani [81] showed that the time-averaged drag on such setups is highly influenced by the turbulence level in the wake. Mackowski and Williamson [82] pointed out that high-amplitude pitching may produce negative propulsive force at relatively low pitching frequencies; other studies reported that vortex shedding mode is a function of both pitching frequency and amplitude [83] and [75] (figure 2.7).

## 2.4 FIM of wall-mounted flexible structures

The deformation of wall-mounted, flexible structures under flow is also ubiquitous in nature and engineering. Potential applications in e.g., energy harvesting, structural design and flow mixing require a comprehensive understanding of this phenomenon. Uncovering the FIM mechanisms modulating such interaction is not trivial due to the significant fundamental challenges related to the multiscale coupling between structures and flow. Substantial experimental and theoretical studies have focused on the deformation of structures aver a range of stiffness and geometries. Alben *et at*. [16, 17] showed the changes of $U^2$-scaling for drag on plates to $U^{4/3}$ for structures under large flow velocity $U$, where the posture of structures presented quasi-parabolic deformation. Sand-Jensen [6] investigated the drag and reconfiguration in five species of freshwater macrophytes. He found that structures with large flexibility can significantly reduced the drag coefficient and result in values similar to very streamlined objects. Additional experimental work [18] studied two different flexible objects under flow, and reported that the drag collapsed when a scaled Cauchy number $Ca$ is used (figure 2.8). Luhar & Nepf [5] systematically investigated the influence of rigidity, geometry, mass ratio and flow speed on the deformation of flexible plates and associated drag changes. They found that for buoyancy-dominated structures with very low stiffness, a sub-linear increase in drag with velocity may occur. They also showed that the model based on beam bending theory is able to predict the deformation and drag of rectangular plates under uniform flows.

Structure flexibility may also modulate the motions induced by the incoming flow and wake. Previous work has primarily focused on the wave-induced motions. Mullarney & Henderson [85] developed a model to predict the wave-forced motions assuming small deflection of a single vegetation. This model was further improved by Luhar & Nepf [86], who included the influence of large-amplitude oscillations, buoyancy and added mass. In addition to the cases under wave-dominated flows, the dynamics of structures in the vicinity of others may exhibit significant coupling, which may also lead to distinctive oscillations and may alter the surrounding flow characteristics. Early work by Thom [87] reported that the drag force on a canopy is much smaller than that adding drag contributions from each structure. Similar

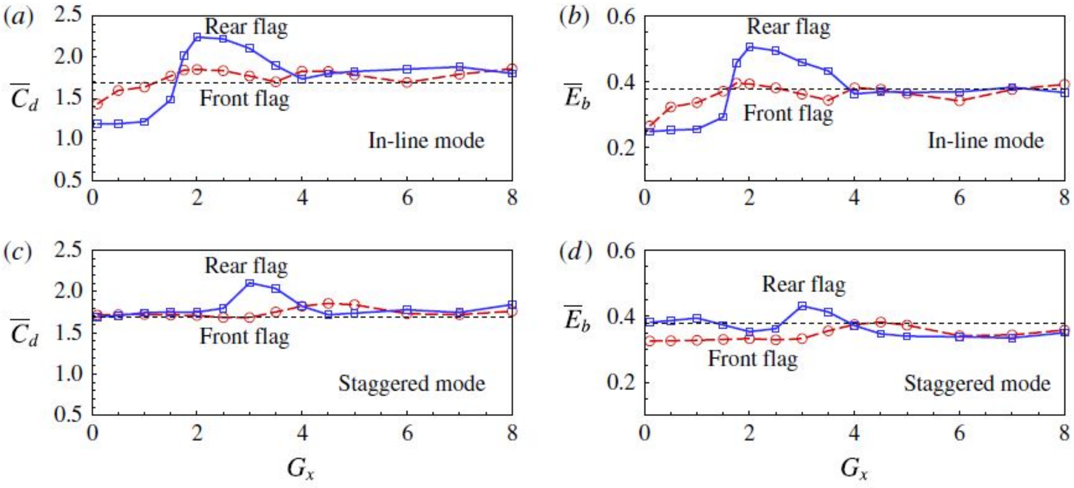

Figure 2.9: Mean drag coefficient, $\bar{C}_d$, and bending energy, $\bar{E}_b$, of inverted flags placed in (a,b) tandem and (c,d) staggered layouts; adapted from [84].

phenomenon was found by other works [88, 89], which highlighted the role of the cluster density. Recent experiments showed that the drag coefficient of aligned plates become sensitive to their separation only below a critical distance [90]. The upstream structures can also significantly influence the oscillations of downstream counterparts. Various experimental [91] and numerical [92] works have investigated the wake induced vibrations of circular cylinders in tandem. Wang *et at*. [93] found that the two cylinders may behave as a single-body with small separation; whereas with sufficient large gap, von K*á*rm*á*n vortex shedding from the upstream structure may impinge the downstream body. Other works [94, 95] studied flag motions in tandem and reported that the drag of the downstream flag may increase due to the large oscillation amplitude triggered from the upstream wake. A recent study pointed out that for inverted flexible flags in tandem, the flapping amplitude of the downstream flag may also increase significantly, whereas the dynamics of the upstream counterpart may remain nearly unchanged [84] (figure 2.9).

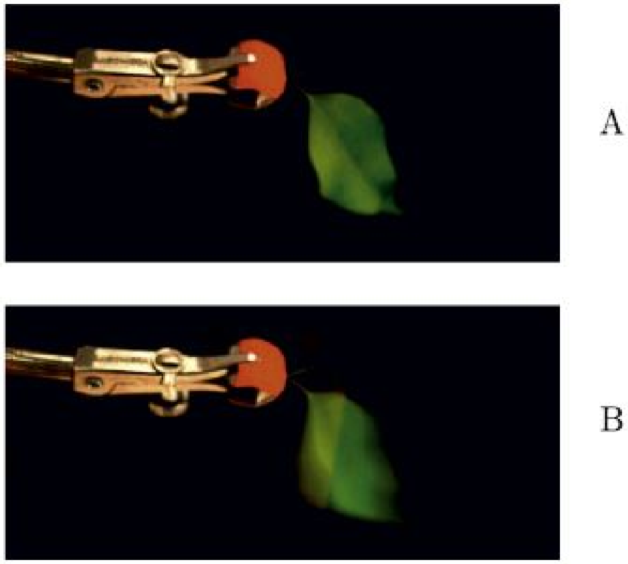

Figure 2.10: View of the leaf before (A) and after (B) the onset of flutter; adapted from [96].

In nature and engineering systems, structures can often be inclined with respect to the incoming flow. Aero/hydrodynamic loads and wake characteristics are significantly influenced by the angle of attack [67, 65, 69]. Experimental investigations [97, 98] showed the distinctive vortex shedding from inclined, rigid plates. Trailing edge vortices were found to induce more fluid circulation and production of Reynolds stress compared to the leading edge vortices. Inclined structures produce asymmetric wakes and net aero/hydrodynamic torque on plates, which may trigger complex rotations or pitching dependent on the incoming velocity, plate geometry and structure stiffness [44, 99, 33, 100]. Onoue *et at.* [33] reported that the pitching amplitude of a rigid flat plate may exhibit hysteresis and abrupt changes as a function of structure torsional stiffness. A recent work [96] pointed out the leaf flutter induced by torsional galloping under various angles of attack with experiments and model analysis (figure 2.10).

# CHAPTER 3

# DYNAMICS OF RECTANGULAR SLUNG PRISMS UNDER FREESTREAM TURBULENCE

This chapter is from the Journal article: Jin Y. and Chamorro L.P. "On the dynamics of three-dimensional slung prisms under very low and high turbulence flows". ***J Fluid Mech***, 816: 468-480, 2017.

## 3.1 Experimental Setup

The oscillation and pitching of two rectangular slung prisms were characterized and quantified under various flows and turbulence levels. The prisms were placed in the frestream region of the Talbot laboratory wind tunnel of the University of Illinois at Urbana-Champaign. The Eiffel-type wind tunnel has a test section of 0.914 m wide, 0.45 m high and 6.1 m long.

A cubic and a rectangular prisms were made with acrylic blocks and balsa material as outer casing. The prisms were $b = 75$ mm and 150 mm long, and shared the same thickness and height $a = 75$ mm. These dimensions led to negligible blockage ratio ($\leq 3\%$). Both prisms were suspended horizontally near the beginning of the test section by four thin 200 $\mu$m plastic lines such that the distance of the center of mass to the pivotal point is $l \approx 1.8a \approx 137.5$ mm (fig. 3.1a). The motion of the prisms were defined in terms of an absolute coordinate system $(x, y, z)$ fixed at the the wind tunnel, and a relative one $(x', y', z')$ centered at the center of mass of the prisms. (fig.

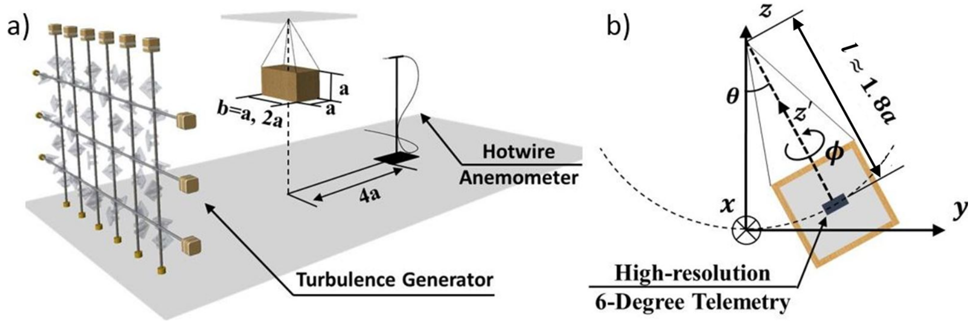

Figure 3.1: a) Schematic of the experimental setup; b) front view illustrating the coordinate systems.

7.1b). The weight of the prisms were 201.3 g and 302.5 g, which resulted in inertia $I$ about the $z'$ axis of $1.73{\times}10^{-4}$ kg m$^2$ and $6.84{\times}10^{-4}$ kg m$^2$. The dynamics of the prisms were characterized at various flow velocities ranging from $U$ =1.6 m s$^{-1}$ to 6.6 m s$^{-1}$ or Reynolds numbers $Re = Ub/\nu \in(0.8,\ 6.6){\times}10^4$, where $\nu$ is the kinematic viscosity of the air. For each flow velocity, the turbulence level was set to negligible (i.e., nearly laminar) to high intensity of $I_u = \sigma_u/U \approx 0.05\%$ and 9.3%. Here $\sigma_u$ denotes the standard deviation of the streamwise velocity fluctuations. An active turbulence generator ($TG$) was used to induce the high $I_u$, whereas the negligible $I_u$ was obtained without the $TG$. Specific details of the geometry and setting of the $TG$ are provided in Jin *et at.* [101].

The instantaneous motion of the prisms was tracked with a small, low weight wireless accelerometer embedded at the center of mass of the prisms at sampling frequency $f$ =256 Hz for periods longer than 360 s, where the last 120 s were used to avoid initial transient disturbances. Although minor, the effect of the mass and moment of inertia of the accelerometer was accounted in the prism assembly. This telemetry system was equipped with a combination of 3-axis gyroscope and 3-axis accelerometer of 16 bits and 12 bits with uncertainties of $0.07^o$ s$^{-1}$ and 0.02 m s$^{-2}$.

Complementary measurements of the flow in the wake of the prisms were obtained with a hotwire anemometer located $4a$ downwind of the center of the slung prisms set with no flow (fig. 3.1a). The probe is made of 5 $\mu$m tungsten wire and operated at a sampling frequency $f=$ 20 kHz for a period of 120 s, where the calibration was conducted against a pitot tube. Through the calibration and experiment, the temperature was kept within ± 0.5 $^o$C to avoid errors due to thermal drift of the voltage signal. Before each measurement, the static position of the prisms were set with the square and rectangular sides facing the flow, with no detectable motion indicated by the telemetry.

## 3.2 Results

In this section we summarize and discuss the dynamics of the slung rectangular prisms as a function of Reynolds number, turbulence levels and aspect ratio. Insight from the velocity fluctuations in the prisms wake is also included to aid the analysis.

### 3.2.1 Dynamics of the cubic prism

In general, the motion of the prism is dominated by two distinctive patterns; pitching about the $z'$ axis and pendulum-like oscillation in the $y-z$ plane across the $Re$ and $I_u$ indicated in §2. The amplitude of the pitching $\phi_m$ as a function of the non-dimensional incoming flow velocity $U^* = U/(lf_n)$ is shown in figure 3.2a for the two $I_u$. Here, $f_n = \frac{1}{2\pi}\sqrt{\frac{g}{l}}$ is the natural frequency of the pendulum-like oscillation under small amplitude, and $g$ is acceleration of gravity. The $\phi_m$ exhibits monotonic increase with $U^*$ and very regular trend under laminar flow. Two distinctive regions can be defined in terms of the amplitude growth rate $\partial\phi_m/\partial U^*= k$, with $k$ a characteristic constant. In the region 1 ($U^* \leq$ 19-20), $k \approx 2$; whereas in the region 2 ($U^* \geq$ 22-23), the growth rate of the pitching is much larger and still linear with $k = 15$ for the laminar flow. Although exhibiting fluctuations, this is roughly the case for the high $I_u$. [102] experimentally investigated the flow passing a free-to-rotate square cylinder under various $Re$, and defined a critical pitching amplitude $\phi_{cr} = 45^o$ that characterize the transition between small and large rotations. Here, similar $\phi_{cr}$ is obtained at the transition between the two regions. The corresponding dominating pitching frequencies $f_p$ normalized by $f_n$ are shown in figure 3.2b. Approximately constant $f_p/f_n \approx 0.2$ characterizes region 1, whereas a gradual decrease occurs in region 2. Inspection of the spectral content of the pitching velocity $\dot{\phi}$ reveals that high-order harmonics are generated in region 2 in the laminar and high $I_u$ flows. This is shown in figure 3.3 with the compensated spectrum of $\dot{\phi}$ normalized by its maximum, $f\Phi^*(= f\Phi_{\dot{\phi}}/[f\Phi_{\dot{\phi}}]_{max})$, for selected cases. It reveals secondary fluctuations, which are linked to the periodicity of the angle-dependent moment $M_\phi = A \sin 4\phi$ of the prism. Here, $A > 0$ is a constant and $\phi$ is the angle of attack [102, 103]. Previous work [102] has pointed out that sustained autorotation of a square cylinder occur for $Re \geq 4.7 \times 10^3$. Here, large-amplitude rotation with $\phi_m \geq 360^o$ were observed for $U^* \geq 36$ ($Re \approx 3.2 \times 10^4$); the suspension lines provide additional restoring moment that suppress the onset of prism autorotation.

It is worth pointing that $f_p \to f_n$ under laminar flow and low $U^*$ ($\approx$8). In this particular condition, the dynamics of the prism is fully dominated by the pendulum-like oscillation (hereon OD). This interesting phenomenon is also inferred from the negligible pitching amplitude in figure 3.2a and the comparatively high amplitude oscillation in figure 3.2c. Here, $\ddot{\theta}_m$ represents the maximum angular acceleration of the oscillation. Later, we will show that the OD involves a synchronization between

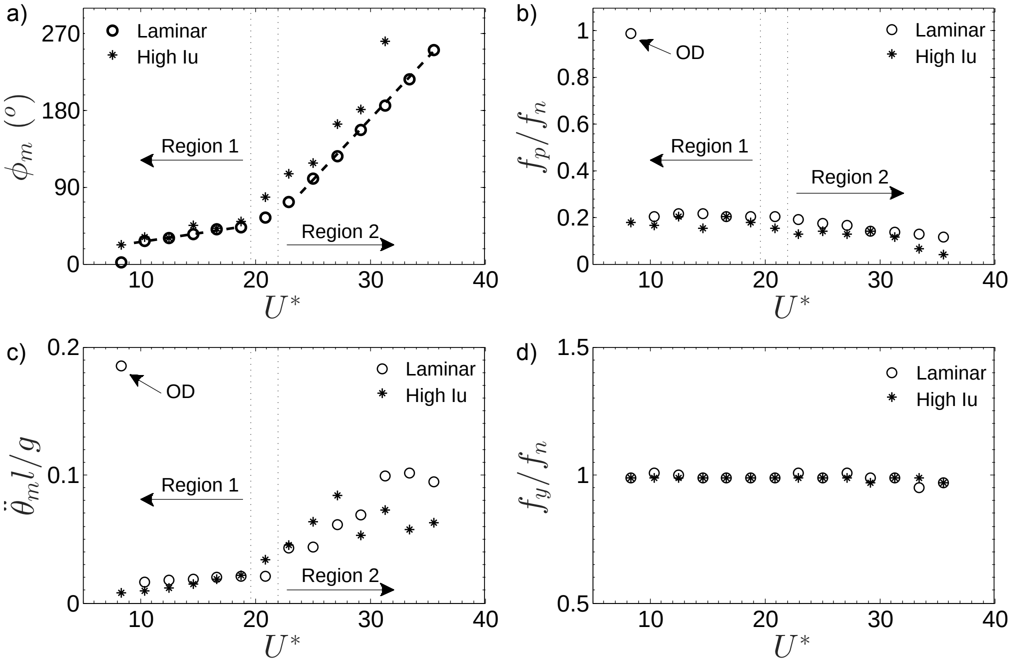

Figure 3.2: Dynamics of the cubic prism. a) Pitching amplitude $\phi_m$; b) dominating pitching frequency $f_p/f_n$; c) amplitude of pendulum-like oscillation $\ddot{\theta}_m l/g$; d) dominating frequency of oscillation $f_y/f_n$.

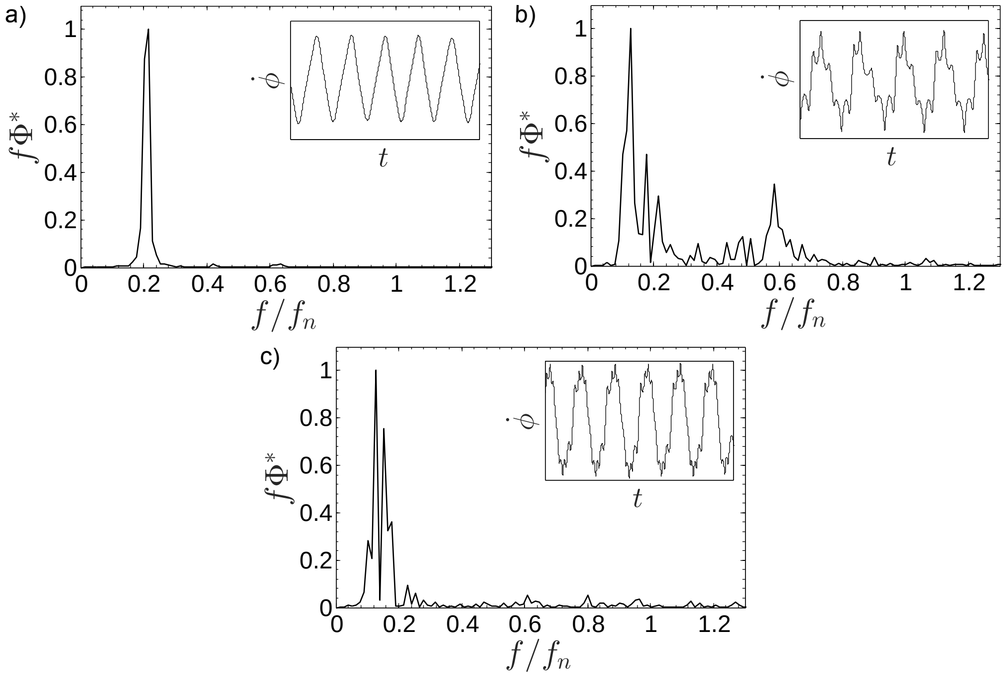

Figure 3.3: Compensated spectra of the angular velocity $f\Phi^* = f\Phi_{\dot{\phi}}/[\Phi_{\dot{\phi}}]_{max}$ of the cubic prism under laminar flow. a) $U^*$=16.7; b) $U^*$=25; c) $U^*$=33.4. Inset shows sample time series of $\dot{\phi}$.

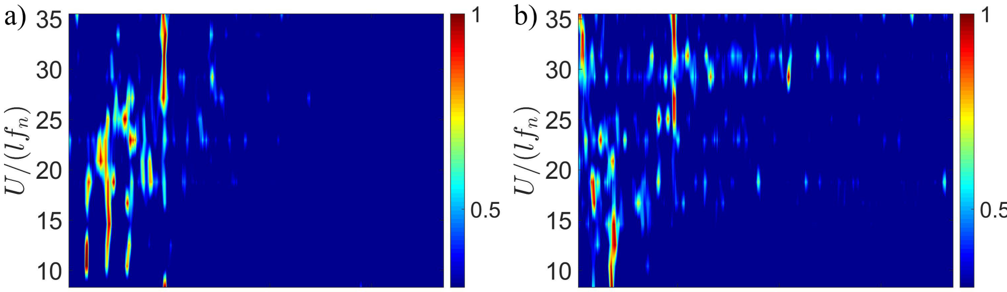

Figure 3.4: Velocity spectra $\Phi_u$ in the wake of the cubic prism. a) Laminar and b) high $I_u$ flow.

the vortex shedding and the body oscillations in the rectangular prism. Similar to the $\phi_m - U^*$ relationship, $\ddot{\theta}_m$ exhibits distinctive behavior in regions 1 and 2 with faster growth with $U^*$ in the region 2. However, it appears to plateau at a $U^*$ and level that depends on $I_u$. The corresponding oscillation frequencies $f_y$ are illustrated in figure 3.2d, which are locked in $f_n$ for all the cases. This suggests that the pendulum-like oscillation of the slung prism is not governed by a Strouhal vortex shedding relation.

Complementary measurements in the wake of the prism indicate a strong linkage between the velocity fluctuations and prism motion. The corresponding 2D spectra for various $U^*$ is shown in figure 3.4. It shows that, regardless of the turbulence, the flow carries the effects of the pitching frequency and harmonics within region 1 (except the OD case), while the pendulum-like oscillation become more distinctive in region 2. As expected, the spectrum of the high $I_u$ shows enhanced energy distributed across $f/f_n$. This is an indirect footprint of the irregular $\phi_m(t)$ and $\ddot{\theta}_m(t)$ as shown in figure 3.2a and 3.2c. The dominating frequencies in region 2 around $U^* \in [19 - 27]$ reflect the secondary velocity fluctuations of the prism pitching. While higher order harmonics are triggered with increasing $U^*$ (fig. 3.3c), their comparatively small amplitude result in reduced footprint in the spectra of figure 3.4.

### 3.2.2 Dynamics of the rectangular prism

We now explore the pitching and pendulum-like oscillation of the rectangular prism under laminar and high turbulence. Due to the higher aspect ratio, the dynamics of the prism is expected to be strongly coupled with the angle-of-attack. As such, the prism motions are characterized with the large face aligned and perpendicular to the flow.

Rectangular side facing the flow

Similar to the other prism, figure 3.5a shows the distribution of $\phi_m$ under the same flow conditions. A sharp jump occurs in the vicinity of $U^* = 22 \pm 1$ under laminar flow, which defines the limits of regions 1 and 2. Within region 1 and laminar flow, the prism motion is characterized by low $\phi_m$ and high $\ddot{\theta}_m$ (figure 3.5a,c). This suggests that the OD phenomenon governs the motion of the rectangular prism. In contrast, a sharp decline of $\ddot{\theta}_m$ and OD motion characterize region 2. The distribution of oscillation amplitude is very similar to that defining the 'upper' to 'lower' branch transition in vortex induced vibrations of slender cylinders [104, 105]. Further, [24] pointed out that within the 'upper' branch in the case of a square cylinder, the frequency of the oscillation and force due to vortex shedding synchronizes, and only $f_y$ (and harmonics) stands out in the frequency domain; this phenomenon is observed in figures 3.5d and 3.6a in region 1. It is worth noting that the increase of $\ddot{\theta}_m$ in region 1 under laminar flow results in slight departure of $f_y$ from $f_n$,which is accounted to the large-amplitude oscillations where $f_n = \frac{1}{2\pi}\sqrt{\frac{g}{l}}$ need to be revisited. Also, due to the negligible pitching, $f_p$ is modulated by $f_y$ as shown in the cubic prism. The suppression of the oscillation by pitching in region 2 is also reflected with lower $f_p$ and distribution of $f_y \to f_n$.

Distinctive behavior was observed under high $I_u$. Similar to the cubic prism, $\phi_m$ exhibits an increase with $U^*$, whereas no net growth occurs in region 2. The OD motion also becomes negligible under high $I_u$. This motion is a result of desynchronization between fluid force and oscillation; the fluctuating velocity with a wide spectrum of turbulent scales in the high $I_u$ might induce disturbances in the fluid-

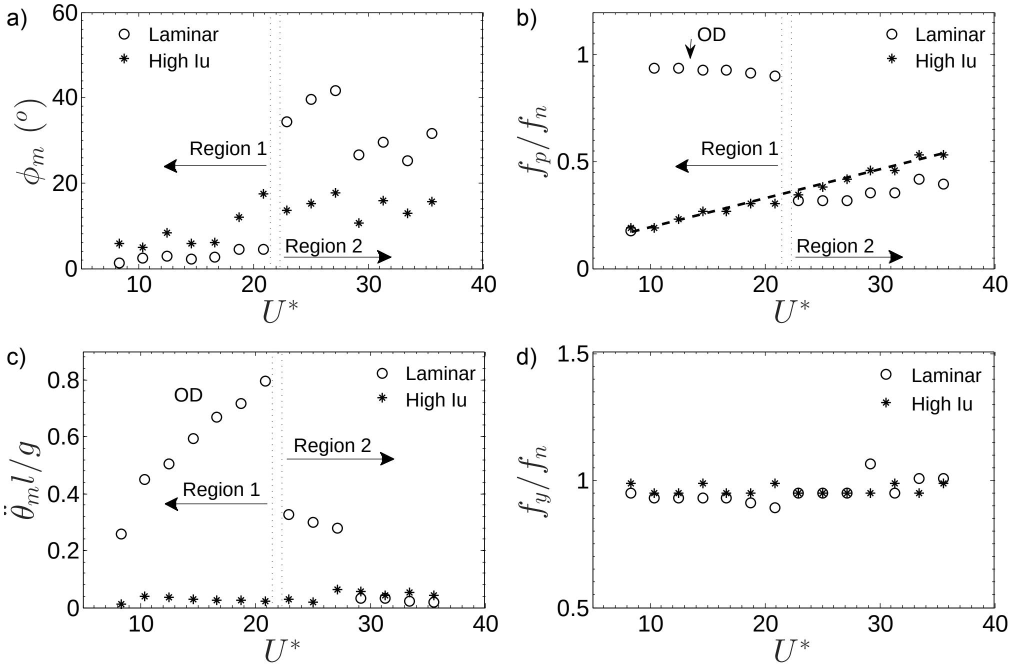

Figure 3.5: Dynamics of the rectangular prism with the large side facing the flow. a) Pitching amplitude $\phi_m$; b) dominating pitching frequency $f_p/f_n$; c) amplitude of pendulum-like oscillation $\ddot{\theta}_m l/g$; d) dominating frequency of oscillation $f_y/f_n$..

structure feedback and, consequently, suppress the synchronization. It is worth pointing that $f_p$ increases nearly linearly with $U$ as shown in figure 3.5b, which is also highlighted in the spectra of wake fluctuations in figure 3.6b. The growth rate characterized with the size of the prism $k = \Delta f_p b/\Delta U \approx 0.014$ is much smaller than the corresponding Strouhal number $St \approx 0.1$ [102]. Similar linear increase of the pitching frequency is reported for a flat plate [100], suggesting that the prism pitching can be approximated to a differential equation of the form:

$$I\ddot{\phi} + \beta\dot{\phi} + K\phi + M_w = 0 \tag{3.1}$$

where $\beta$ accounts for the damping of the system, $K$ represents the restoring torque provided by the suspension lines and $M_w$ embodies all the torques generated from wind-induced forces including angle-dependent moment $M_\phi$, vortex-shedding-induced moment $M_v$, among others. As a first-order estimation, we ignore the influences of damping, $M_v$ and suspension lines so that the expression is simplified as:

$$I\ddot{\theta} + M_\phi = 0 \tag{3.2}$$

Similar to the case of 2D flat plate, numerical [54] investigations have shown that with small $\phi$, $M_\phi \approx \frac{1}{2}\rho U^2 bS\gamma\phi$, where $\rho$ and $S$ are the density of air and characteristic area and $\gamma$ is a geometry dependent constant. Therefore, the frequency of pitching leads to:

$$f_p = \frac{1}{2\pi}\sqrt{\frac{1}{2}\rho U^2 bS\gamma/I} \propto U \tag{3.3}$$

It is worth pointing that for the laminar flow within region 2, there is a gradual increase of $f_p$ with $U^*$ but at a much lower rate. This further indicates the influences of turbulence on the aerodynamics of 3D structures as it does for 2D bodies.

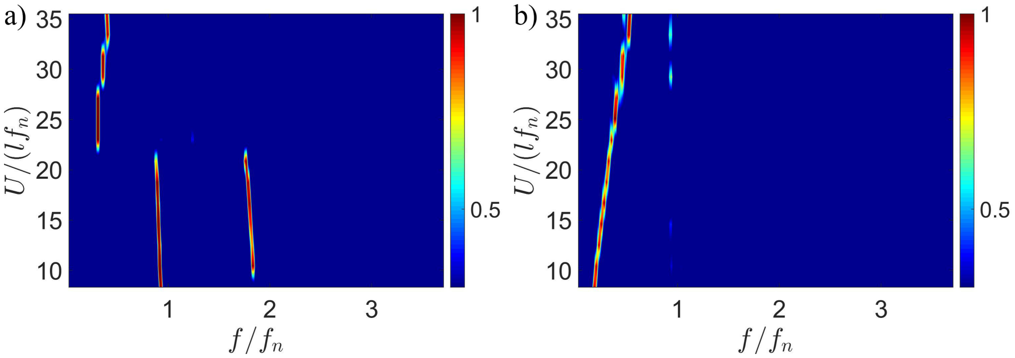

Figure 3.6: Velocity spectra $\Phi_u$ in the wake of the rectangular prism with the large side facing the flow. a) Laminar and b) high $I_u$ flow.

Square side facing the flow

Similar to § 3.2.1, $\phi_m$ exhibits distinctive behavior in two regions defined by a sudden change, as shown in figure 3.7a. Within region 1, $\phi_m$ increases with $U^*$ under laminar flow, whereas the changes are milder for high $I_u$. At $U^* \approx 16.5$, $\phi_m$ reaches the minimum regardless of the turbulence levels, which represents a quasi-static state (hereon QS) where the pendulum-like oscillation is small (figure 3.7c). In this particular condition, the equilibrium position of the prism is inclined with respect to the initial one (no flow).

Eq. 3.1 indicates that the pitching of the prism is influenced by the wind force as well as the restoring moment from suspension lines. Within region 1 and at low $U^*$, the pitching is modulated by the suspension lines, where the equilibrium position is that of its static state. However, similar to the 2D counterparts [33], the angle-dependent moment $M_\phi$ tends to keep the large side facing the flow, and the moments generated from suspension lines and $M_\phi$ reach the quasi-static balance at the QS condition. At sufficiently large $U^*$, the wind force dominates the dynamics of the prism leading to an equilibrium pitching with the square side facing the flow.

In this condition, the dynamics of the prism are very analogous to that described in § 3.2.1. This is evidenced with increase of $\phi_m$ and $\ddot{\theta}_m$ with $U^*$, as well as with the linear $f_p - U^*$ relation despite the turbulence levels (fig. 3.7b). Also noted that $f_y$ is 'locked in' ($f_n$) over the span of $U^*$ (fig. 3.7d).

Inspection of spectral content of the velocity fluctuation in the prism wake, for the laminar and high $I_u$ cases, reveal that the dominating pitching frequency (and harmonics) are the most energetic structures (fig. 3.8). The dynamics of the prism exhibits higher-amplitude pendulum-like oscillations and smaller pitching under high $U$ and $I_u$, which is reflected with the distinctive $f_y$ signature in the wake.

Similar phenomenon is also observed in figure 3.6 when the rectangular side of the prism faced (at $t = 0$) the flow. It is worth pointing that figure 3.8a also shows a weak frequency component at $f/f_n \sim 3.2$ when the prism is at the QS state. This corresponds to the periodic vortex shedding from the edge of the prism following the Strouhal relationship, which further verifies the quasi-static state of the prism under this specific case.

## 3.3 Conclusion and remarks

In this work, the dynamics of rectangular slung prisms were systematically studied under two aspect ratio $a/b$, turbulence levels $I_u$, and various incoming flow velocities $U$. The pendulum-like oscillations perpendicular to the incoming flow and pitching about the vertical axis of symmetry of the prims are the most distinctive patterns. For the cubic prism, regardless of turbulence levels, sufficiently high $U^*$ triggers secondary pitching velocity fluctuations and more rapid increase of pitching and oscillation amplitudes. In general, The dynamics of rectangular prism exhibits more complex motion due to the sensitivity with the angle-of-attack. With the large

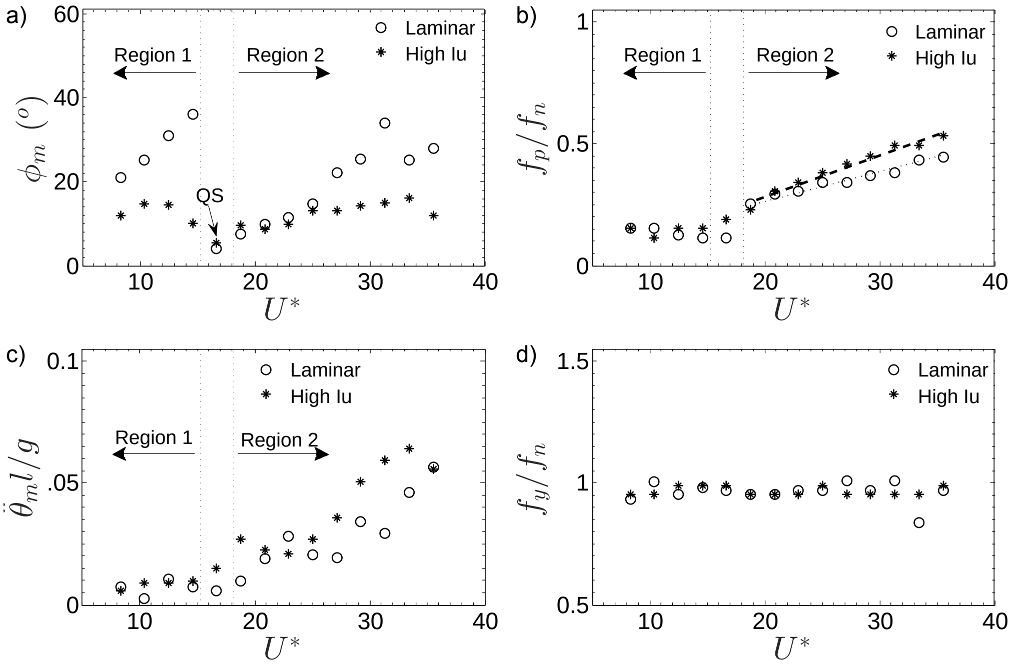

Figure 3.7: Dynamics of the rectangular prism with the square side facing the flow. a) Pitching amplitude $\phi_m$; b) dominating pitching frequency $f_p/f_n$; c) amplitude of pendulum-like oscillation $\ddot{\theta}_m l/g$; d) dominating frequency of oscillation $f_y/f_n$.

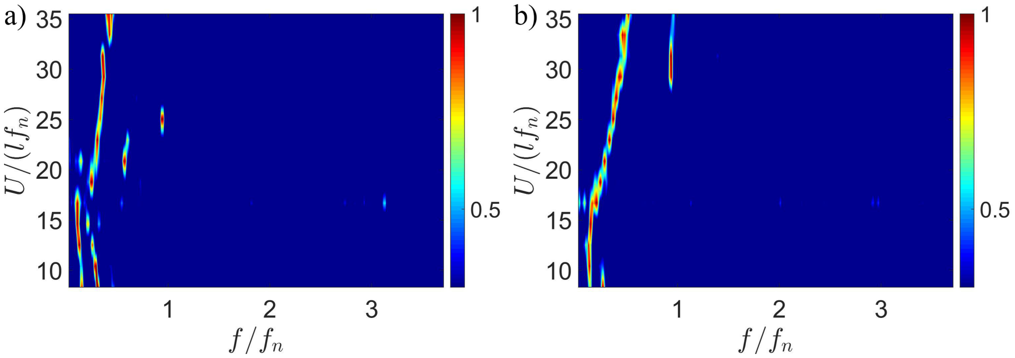

Figure 3.8: Velocity spectra $\Phi_u$ in the wake of the rectangular prism with the square side facing the flow. a) Laminar and b) high $I_u$ flow.

side facing the flow, the prism motion is dominated by large-amplitude oscillation under laminar flow and low $U^*$. Flow turbulence breaks the synchronization between vortex shedding and oscillation of the prism, and the pitching frequency shows linear relations with $U^*$. With the square side facing the flow, the restoring moment from the suspension lines contributes to maintain the equilibrium position of pitching coincident with its initial orientation for comparatively low $U^*$. This moment is gradually balanced by the wind force with increasing $U^*$, leading to a quasi-static state that eventually results in the rectangular side facing the flow under both laminar and turbulence flow. For all the tests, the dominating oscillation frequency is 'locked' close to the natural frequency of the pendulum-like oscillations.

The time necessary for reaching steady oscillation under OD in both cubic and rectangular prisms resulted orders of magnitude larger than that defined by the integral time scale of the turbulence or that defined by the mean flow and the scale of the setup in the laminar case. This is illustrated in Figure 3.9a,b with sample time series $t^* = tf_n$ of the dynamics of the rectangular prism under $U^* = 16.7$ and laminar flow; a distinctive transition of the dynamic occurs at $t^* \approx 230$ (fig. 3.9a). Before this time, the prism exhibited large amplitude and low frequency pitching regardless of turbulence levels (fig. 3.9c). A fast expansion of the pendulum-like oscillation takes place close to the transition, resulting in pitching weakening with its frequency modulated to the high-amplitude oscillations (fig. 3.9a,b). Similar transition occurring in the synchronization of FIV of a circular cylinder was also reported [106], suggesting that the initial conditions and nonlinear effects play significant role determining the transition time.

Compared to the angle-dependent moment $M_\phi$, the effects of vortex-shedding-induced moment $M_v$ is not distinctive in most of the cases except in the QS state,

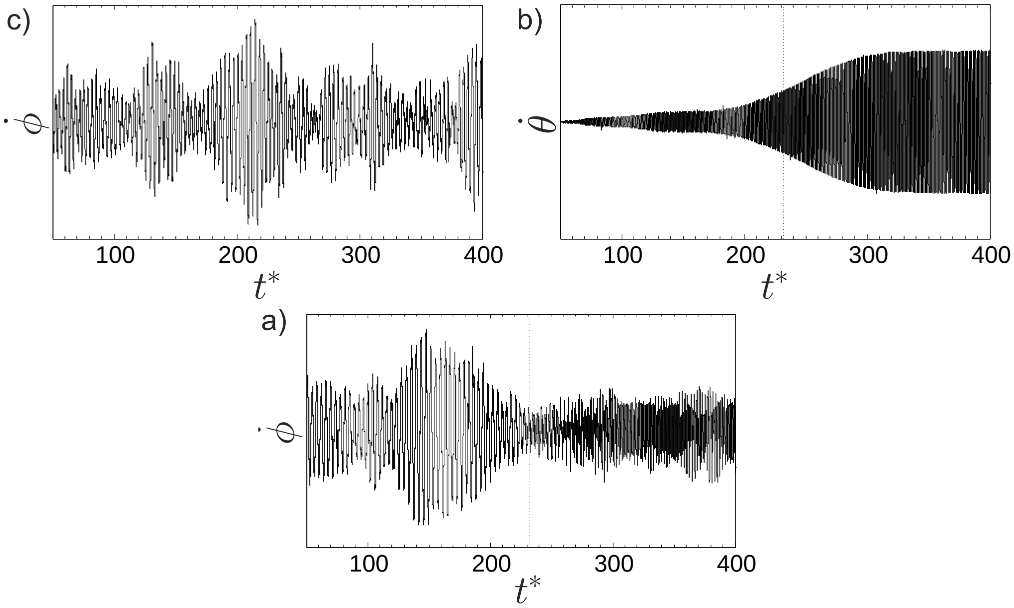

Figure 3.9: Time series of the motion of the rectangular prism with the large side facing the flow at $U^* = 16.7$. a) $\dot{\phi}(t)$ under laminar flow; b) $\dot{\theta}(t)$ under laminar flow; c) $\dot{\phi}(t)$ under high $I_u$.

where the corresponding Strouhal vortex shedding frequency is presented in the wake fluctuation. This is different from the flow passing a free-to-rotate square cylinder [102], where the vortex shedding frequency associated to fixed cylinder plays a significant role modulating the rotation. This can be accounted to the influences from the pendulum-like oscillations with its frequency 'locked in' $f_n$ that blocks the periodic vortex shedding based on $St$, as well as the restoring moments from suspension lines providing additional disturbances.

# CHAPTER 4

# PASSIVE CONTROL OF SPLITTERS IN THE WAKE OF ELLIPTIC CYLINDERS

This chapter is from the Journal articles: 1) Jin Y. and Chamorro L.P. ”Passive pitching of splitters in the trailing edge of elliptic cylinders”. ***J Fluid Mech***, 826: 363-375, 2017, and 2) Jin Y., Hayat, I. and Chamorro L.P., ”Modulation of aerodynamic force on a 2D elliptic body via passive splitter pitching under high turbulence”. ***J Fluid Struct***, 74: 205-213, 2017.

## 4.1 Experimental setup

In this work, the distinctive pitching of hinged splitters in the trailing edge of an elliptic cylinders was investigated at various angles of attack (AoA) of the cylinder, Reynolds numbers, splitter lengths and incoming turbulence levels. The experiment was conducted in the same wind tunnel.

An elliptic cylinder with semimajor axis of $a = 50$ mm, semiminor axis of $b = 30$ mm was vertically placed in the wind tunnel with the cross-section spanning from the bottom to the top walls. Two rigid flat plates with chords $c = 2a$ (short) and $c = 4a$ (long) were vertically hinged with the rotating axis at the trailing edge of the cylinder. The motion of the plates was investigated for various flow velocities ranging from $U$ =2.8 m s$^{-1}$ to 8.6 m s$^{-1}$, with the corresponding $Re = U2a/\nu \in (1.9, 5.7) \times 10^4$. For each velocity, the cylinder was placed with $AoA = 0^o, 30^o, 45^o$

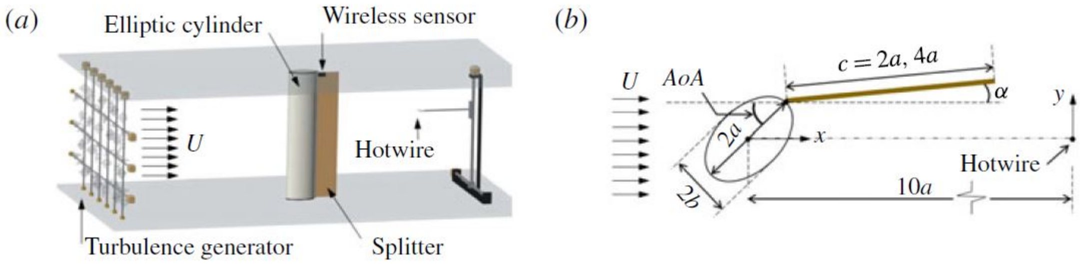

Figure 4.1: (a) Schematics of the elliptic cylinder and splitter system in the wind tunnel; (b) plain view with basic variables.

and $60^o$ (figure 4.1). The pitching of the plates were characterized under low and high turbulence levels with $I_u = 0.05\%$ and 10.5%. To measure the dynamics of the splitter, the same accelerometer was applied and attached at the top side of the splitter with frequency of 256Hz. Complementary measurements of the lift and drag forces on the elliptic cylinder were conducted with an ATI Gamma force sensor fixed at the top side of the elliptic cylinder at a frequency of f D1 kHz with an accuracy of 1 %. For each set-up, the accelerometer signatures were sampled for periods of 120 s only after the dynamics of the plate reached the steady state; this occurred at least 60 s after the constant flow was obtained in the tunnel.

## 4.2 Results

In this section, we describe and discuss the characteristic pitching of splitters triggered by the flow fluctuations as a function of the $Re$, $Iu$, $AoA$ and $c/a$ ratio.

### 4.2.1 Dynamics of the short splitter

This configuration is first characterized for low and high Iu at various $Re$ and $AoA$ of the cylinder. Here, the splitter exhibits small-amplitude oscillations ($< 8^o$, with the

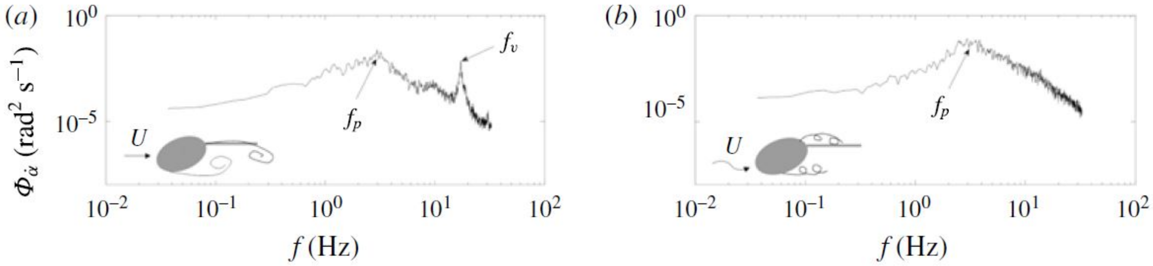

Figure 4.2: Spectra of angular velocity of the short splitter at $AoA = 30^o$ under a) low and b) high turbulence.

maximum achieved for the highest flow and turbulence levels) around the equilibrium position, which is nearly parallel to the direction of the mean flow. In general, the dynamics under low $I_u$ presents two distinctive modes, namely $f_p$ and $f_v$ as reflected in the spectrum in figure 4.2a, whereas $f_v$ is not observed in the high $I_u$ (figure 4.2b). For thin flat plates pitching in the flow, Jin *et at*. [100] reported that dynamics of the can be described by the equation:

$$I\ddot{\alpha} = -\beta\dot{\alpha} + M_W \tag{4.1}$$

where $\beta$ represents the damping term and $M_W$ includes the torque produced by wind. Here, $M_W$ can be decomposed into the contribution from mean velocity ($M_{\alpha u}$) and the fluctuating velocities ($M_{\alpha u'}$). For thin flat plates with small angle pitching, $M_{\alpha u} = 0.5C_m\rho_a\bar{u}^2c^2L$, where $C_m$ is the moment coefficient, $\rho_a$ is the air density, $L$ is the structure span and $\bar{u}$ is the effective velocity. For small angles, $C_m \approx -\pi/2$, and then we can rearrange the equation as:

$$I\ddot{\alpha} + \beta\dot{\alpha} + 1/4\pi\alpha\rho_a\bar{u}^2c^2L = M_{\alpha u'} \tag{4.2}$$

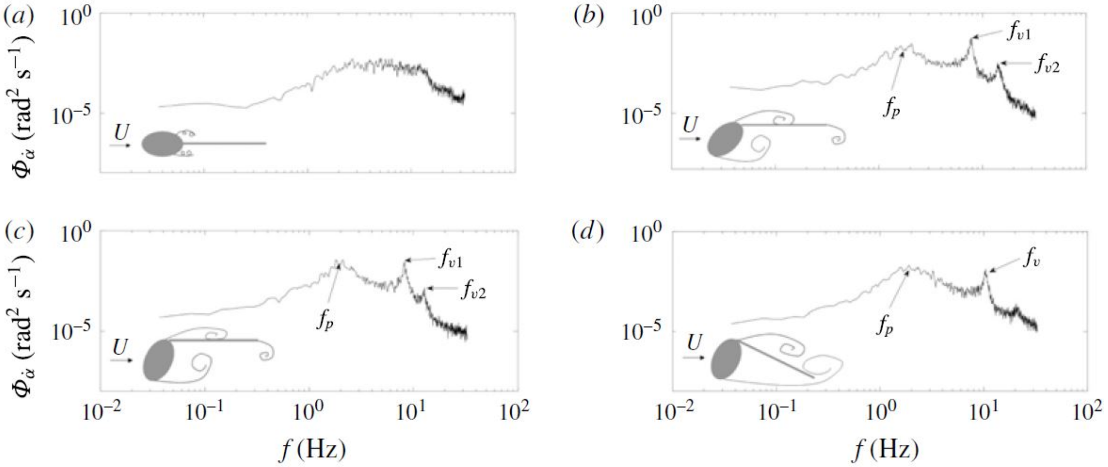

Figure 4.3: Spectra of angular velocity of the long splitter at low $I_u$ with the cylinder at a) $AoA = 0^o$ b) $45^o$, and c) $60^o$, d) $AoA = 60^o$ with splitter in inclined equilibrium.

In the Fourier domain, it can be rearranged as:

$$\hat{\alpha} = \frac{\hat{M_{\alpha u'}}}{1/4\pi\rho_a\bar{u}^2c^2L - (2\pi)^2 I f^2 + 2\pi i f \beta}. \tag{4.3}$$

With $f \to f_p = \sqrt{\pi\rho_a L/I}(c\bar{u}/4\pi)$, the norm of $\alpha$ is close to the local maximum, which lead to the frequency $f_p$ stand out. For the low $I_u$ cases, the vortex shedding from the elliptic cylinder is strong and that is reflected in the term $M_{\alpha u'}$ as the $f_v$ observed in the corresponding spectrum. However, this vortex shedding could be significantly suppressed under high $I_u$ [7], where this peak may disappear.

### 4.2.2 Dynamics of the long splitter

The increase of the splitter length to twice the semimajor axis of the cylinder leads to very distinctive motions; representative features are illustrated at $Re = 3.8 \times 10^4$ for the low $I_u$ in figure 4.3. Specifically, figure 4.3 (a) shows the power spectra of the splitter motions at $AoA = 0^o$. The motion is characterized by a comparatively broad frequency distribution with no dominant peak. In this condition, the splitter undergoes chaotic-like behavior with very small amplitude. Shukla *et al.* [107] reported that for splitters freely hinged in the center of the wake of a circular cylinder, the periodic vortex shedding is suppressed with a significant decrease of pitching amplitude for splitter larger than $\sim$3 cylinder diameters. It is worth noting that the ratio of chord length to the hydraulic diameter of the elliptic cylinder $D_H = 4A/P$, where $A$ and $P$ are the cross-sectional area and perimeter of the ellipse, is close to 3. In contrast, the high background turbulence increases the flow mixing in the wake resulting in higher $\bar{u}$; this leads to an increased influence of $M_{\alpha\bar{u}} \propto \bar{u}^2$, sufficient for the $f_p$ signature. More energetic vortex shedding from the cylinder occurs at larger $AoA$, and the dynamics of the splitter becomes highly influenced by $M_{\alpha\bar{u}}$ and $M_{\alpha u'}$. Figure 4.3(b) shows a representative spectrum of for $AoA = 45^o$. In addition to $f_p$, it shows two distinctive vortex shedding at frequencies $f_{v1}$ and $f_{v2}$. We noted that similar phenomenon occurred with the cylinder $AoA = 30^o$ and $AoA = 40^o$ for all $Re$. Knisely [108] experimentally investigated the body force fluctuations of a rectangular cylinder with aspect ratio $B/G = 2$, where $G$ and $B$ are the sides with the shorter one facing the flow. There, the fluctuating lift also exhibits multiple modes with two dominating peaks. Other studies with detailed flow visualizations such as Yu *et al.* [109] indicate that two vortex shedding modes coexist for the long splitter case. This is illustrated here in the subplot of figure 4.3(b); those modes correspond to a main vortex shedding starting close to the leading edge of the splitter from the cylinder ($f_{v1}$) and a secondary vortex close to the trailing edge of the splitter ($f_{v2}$). We further verified this with additional flow measurement in the vicinity of the leading edge of the splitter fixed parallel to the flow to exclude the influence of

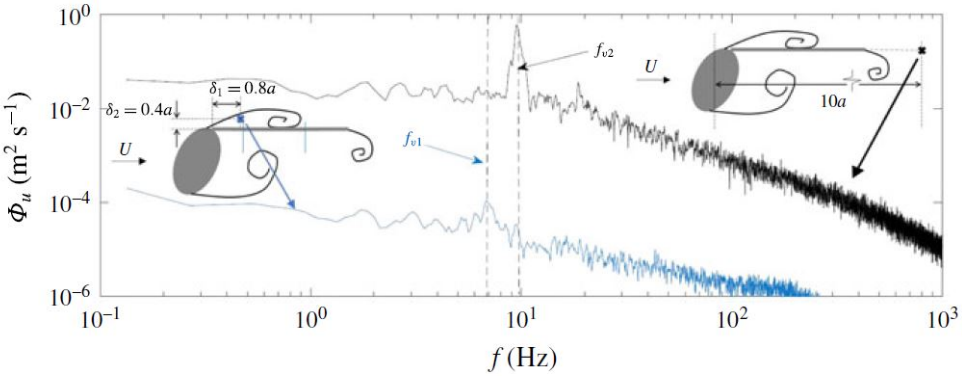

Figure 4.4: Velocity spectra close to the leading edge of the splitter (blue) and in wake region (black) at $AoA = 60^o$ highlighting distinctive vortex shedding modes

pitching. Figure 4.4 shows the lower vortex shedding frequency corresponding to the peak $f_{v1}$ close to the leading edge of the splitter; whereas the higher-frequency component $f_{v2}$ dominates in the wake region.

For the short splitters, the equilibrium position of the pitching is almost coincident with the direction of incoming flow. However, an other pitching equilibrium position was observed under sufficiently high $AoA$. Figure 4.3(c,d) illustrates the dynamics of the splitter with the cylinder at $AoA = 60^o$ and low incoming $I_u$ for the two equilibria. In the new equilibrium, the trailing edge of the splitter is almost aligned with the leading edge of the elliptic cylinder. Indeed, for the elliptic cylinder with large $AoA$ (larger than $45^o$), strong recirculation regions are formed in the wake of the cylinder [110], where a low pressure region is formed and able to stabilize the splitter. This phenomenon was further explored with the complementary measurements of the lift and drag forces of the cylinder in figure 4.5. The deflection of the splitter leads to a low pressure region compared to another equilibrium, leading to a larger drag force and lift force in the negative direction. It is noted that the high $I_u$ significantly reduces the recirculation region and induces flow disturbances [14, 111],

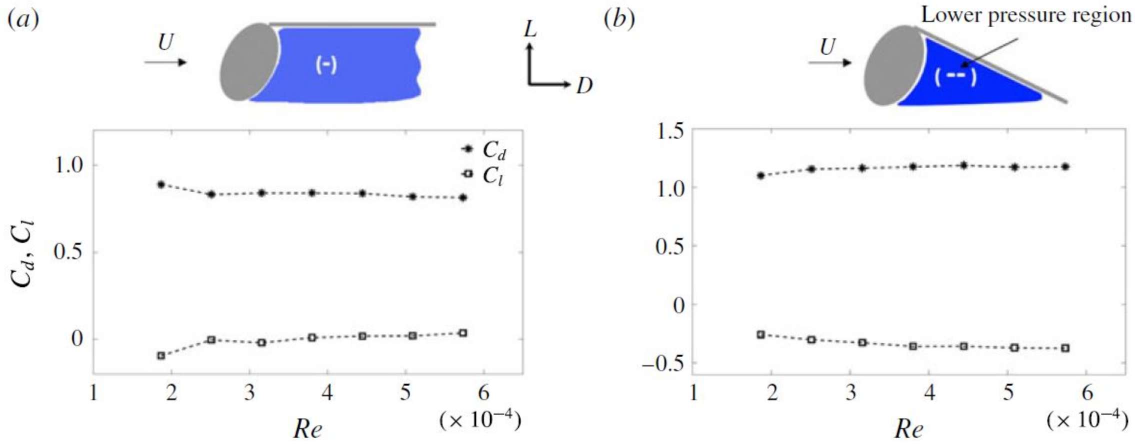

Figure 4.5: Drag and lift coefficients at $AoA = 60^o$ with the splitter equilibrium a) parallel to the flow and (b) inclined towards the cylinder leading edge.

which hinders the formation of an inclined equilibrium.

### 4.2.3 Modulation of aerodynamic forces

We first quantified the effect of the splitters on the mean drag $C_d = D/(\rho HbU^2)$ and lift $C_L = L/(\rho HbU^2)$ coefficients for various $Re$ and $AoA$ of the elliptic body. Here, $D$ and $L$ denote the drag and lift forces; whereas $H$ and $\rho$ indicates the span of the body and the density of the air. Figure 4.6 summarizes all the cases including the base cases with the bare elliptic body for reference. It is worth pointing that the $C_d$ obtained for the base cases matched very well with those reported by Modi *et al*. [65] for similar $Re$ (=6.8 $\times 10^4$) and low turbulence levels across $AoA$. This complementary testing performed with very low $I_u \approx 0.05\%$ serves to discard any offset of the instrumentation before conducting experiments with the splitters under high turbulence flow. It is also noted that high $I_u$ leads to reduced $C_d$ for the base cases across all the tested $AoA$, with more distinctive changes at lower $AoA$. Similar to the dynamics with circular cylinders [112], $I_u$ can effectively delay the boundary layer separation for small $AoA$; there, the surface pressure distribution is highly affected by this phenomenon. At comparatively high $AoA$, strong vortex shedding with large flow separation region occurs regardless of the background $I_u$.

In general, the splitter exhibited small-amplitude pitching of $<8^o$ around the equilibrium position, which was nearly parallel to the streamwise direction. Such motions were sufficient to disturb the wake and, consequently, the mean and unsteady forces on the elliptic body. Consistent with the case of circular cylinder [60], the splitters induced reduced $C_d$ on the elliptic body for all $AoA$. This occurred across $Re$ for cases with significant flow separation, i.e., large $AoA$ of $45^o$ and $60^o$; whereas this phenomenon was observed at $Re > 3 \times 10^4$ for the lower $AoA$ ($0^o$ and $30^o$). Note that the splitter pitching enhance wake mixing at sufficiently high $Re$; however, it might dampen the mixing by limiting the dynamics of vortex shedding at lower $Re$; this might explain the larger $C_d$ at $Re \leq 3 \times 10^4$ and lower values for higher $Re$. Remarkably, no significant difference in the mean aerodynamic force exerted on the elliptic body was observed between the two splitters. Previous studies on circular cylinder with splitters under low turbulence show a decrease of $C_d$ with the increase of splitter length [60]. Our results, however, show that the length of the splitter ($c/(2a)$ =1 or 2) does not play a significant role in the $C_d$ of the elliptic body under high $I_u$. This suggests that significant wake mixing occurs within $x/(2a) < 2$ promoted by the $I_u$ level. Then, a discrete increase of splitter length past this distance does not induce major changes. Also, $C_d$ is mostly insensitive to $Re$ at larger $AoA$ configurations; there, the splitter pitching has lower impact on the modulation of the flow characterized by comparatively intense turbulence and large $D$ on the structure. It is also worth pointing out that independent of the $AoA$, $C_d$ values plateau to ≈75%-80% of the bare body counterpart.

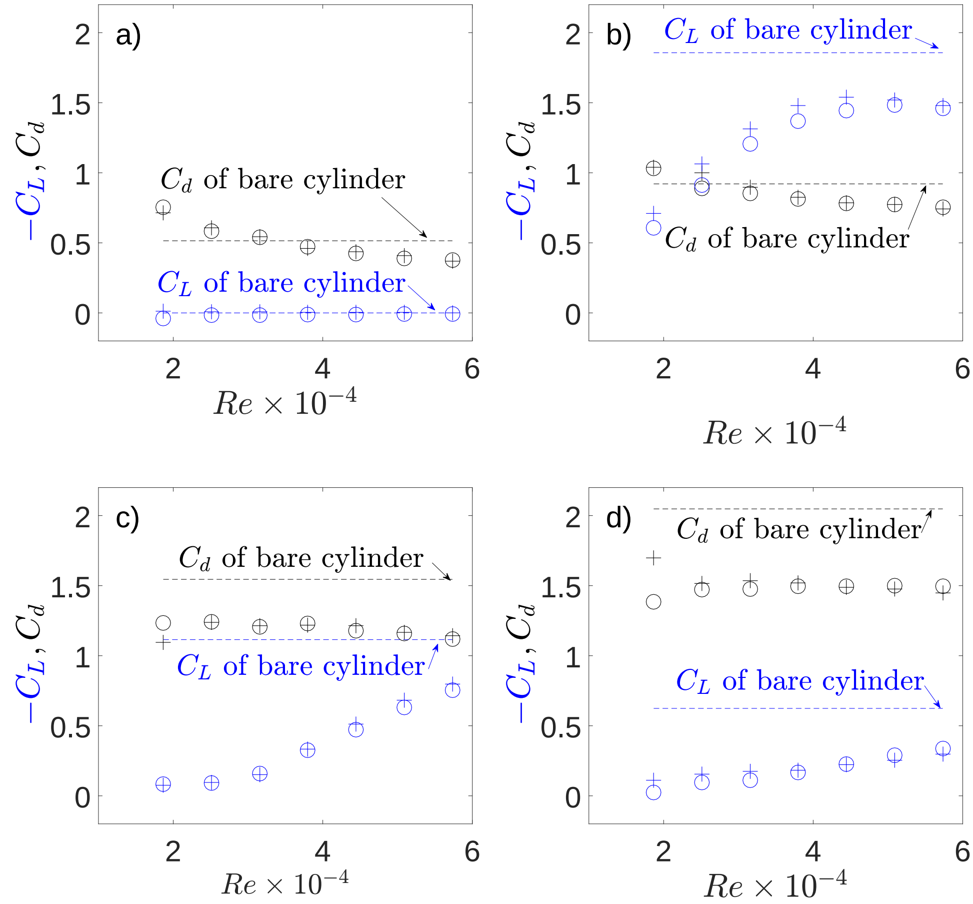

Figure 4.6: Mean lift ($C_L$) and drag ($C_d$) coefficients on the elliptic body for various $Re$ at $AoA$ = a) $0^o$; b) $30^o$; c) $45^o$; d) $60^o$. Symbols denote the elliptic body with splitter $c/(2a) = 1$ ($\circ$) and elliptic body with splitter $c/(2a) = 2$ (+). Dashed lines indicate the corresponding coefficients for the bare elliptic body. $C_L$ and $C_d$ are illustrated in blue and black colors for clarity.

The splitters modulate $C_L$ in a distinctive way that result in lower values across $Re$ and $AoA$; similar to $C_d$, such modulation is nearly independent of the splitter length. Compared to those used in e.g., planes, the hinged splitter experiencing passive pitching can be thought as *inverse flaps*. They redirect the wake towards the streamwise direction and reduce the lift. Except for the trivial case of $AoA = 0$, where $C_L = 0$ due to symmetry, $C_L$ exhibits substantial $Re$ dependence for large $AoA$. Specifically, this quantity grows monotonically with $Re$ at $AoA = 45^o$ and $60^o$.

Under sufficiently large $AoA$ with well-defined flow separation, the low-pressure region between the base of the elliptic body and the splitter facilitates a slightly inclined equilibrium position of splitter pitching. This phenomenon is more clear at relatively high $Re$. Qualitative video measurements, not shown here, illustrate this effect. As pointed by Lu *et al*. [71], small inclination of the splitter in the wake of a cylinder can effectively increase the magnitude of the lift, and reduce the base pressure [70, 66]. Additionally, high levels of $I_u$ help to delay the boundary layer separation, which leads to increased $C_L$ respect to the negligible $I_u$ counterpart across $AoA > 0$ for the bare elliptic body.

The instantaneous signature of the $D$ and $L$ forces for all the cases are further inspected via the normalized joint PDF distribution in figure 4.7. Note the dominant force fluctuations perpendicular to the major axis of the cylinder at $AoA = 0^o$ regardless of the configuration, i.e., with or without the splitters. This behavior is typical of circular cylinders, where the lift fluctuation from vortex shedding is dominant [113]. The magnitude, direction and distribution of the aerodynamics forces is, however, largely modulated by the splitters with the elliptic body inclined. Despite the major axis of the elliptic-like force (PDF) distribution being close to

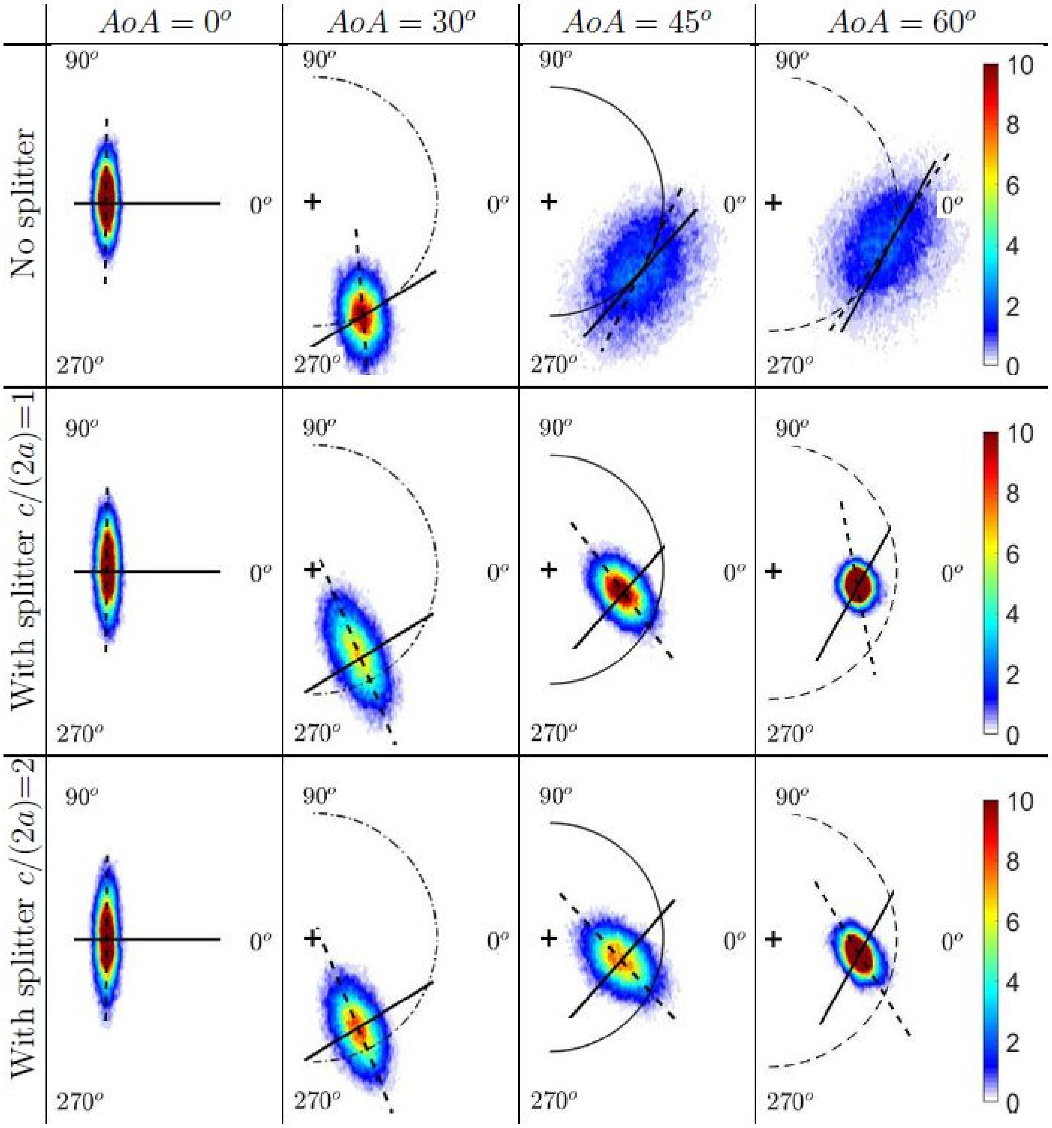

Figure 4.7: Joint PDF of the instantaneous lift and drag on the elliptic body for various $AoA$ and splitter configurations. The continuous lines on the joint PDF indicate the major axis of the elliptic body; whereas the dashed lines denote the preferential orientation of the joint PDF. Dotted-dashed, continuous and dashed semi circumferences denote sets sharing same $AoA$; their radii are defined to the mean force level of the bare case to aid the comparison.

the lift direction in the bare cylinder case at $AoA = 30^o$, a non-negligible counter-clockwise rotation of $\approx 17^o$ with respect to the mean lift direction occurs with the two splitters. This implies a dominant force fluctuations nearly perpendicular to the major axis of the cylinder with splitters and highlights the distinctive modulation of these structures.

## 4.3 Conclusion and remarks

The dynamics of a splitter in the trailing edge of an elliptic cylinder is significantly modulated by the mean and fluctuating velocities in the wake region under very low $I_u$. Turbulence can severely alter vortex shedding from the cylinder, and the coherence of the pitching from the unsteady flow may be reduced. For sufficiently long splitters (e.g. $c/(2a) \sim 2$), multiple vortex shedding modes coexist close to both the leading and trailing edges of the splitter. In such cases, a large recirculation region facilitates an inclined equilibrium for a splitter pitching. Splitters strongly modulate the mean and unsteady aerodynamic forces on an elliptic body in high turbulence flows common in atmospheric or marine environments. Such phenomenon was observed across $AoA$ and $Re$. These structures are specially effective in reducing force fluctuations on the elliptic body subject to large flow separation, i.e., large $AoA$. Background turbulence plays a significant role on the feedback between the elliptic body and splitters. In particular, higher lift and lower drag occurs in the bare body across $Re$ and $AoA$ with respect to the very low turbulence counterpart; however, the splitters lead to reduced lift and drag. Orientation of the aerodynamics force can be effectively manipulated by splitters and, consequently, reduce the overall force fluctuations. The cases studied bridge those of passive splitter pitching in the wake of circular cylinders and plates. The elliptic and splitter configurations also provide insight for animal locomotion, stability of structures and energy harvesting.

# CHAPTER 5

# ACTIVE PITCHING SPLITTERS IN THE DRAG AND WAKE OF A CIRCULAR CYLINDER

## 5.1 Experimental Setup

The experiments were performed in the freestream region of the Talbot wind tunnel at the University of Illinois. The Eiffel-type wind tunnel has a section 6 m long, 0.46 m high and 0.914 m wide.

A smooth circular cylinder of diameter $d = 0.1$ m was placed vertically near the inlet of the wind tunnel with its cross-section spanning from the bottom to the top walls, resembling a two-dimensional body (see figure 5.1a). Three rigid plates of chords $L/d = 1/4$, $1/2$ and $1$ (here on referred to as short, medium and long) and sharing the thickness $c = 2.5$ mm were placed vertically along the full span of the cylinder, and allowing a very minor gap with the cylinder. A variety of periodic, oscillatory motions were imposed on the plates with the center of oscillations coinciding with the axis of the cylinder; this way, the plates were always normal to the surface of the cylinder (see figure 5.1b). The motions of the plates were controlled with a steering gear system, where a high-resolution wireless accelerometer [100] was used to ensure minor deviations ($< 2\%$) of the resulting motions respect to the imposed theoretical oscillations. The cylinder-splitter assemblies were characterized under an incoming velocity of $U_0 = 2.4$ m s$^{-1}$ and negligible freestream turbulence intensity of 0.2%, resulting in a Reynolds number of $Re = U_0 d/\nu = 1.6 \times 10^4$, where

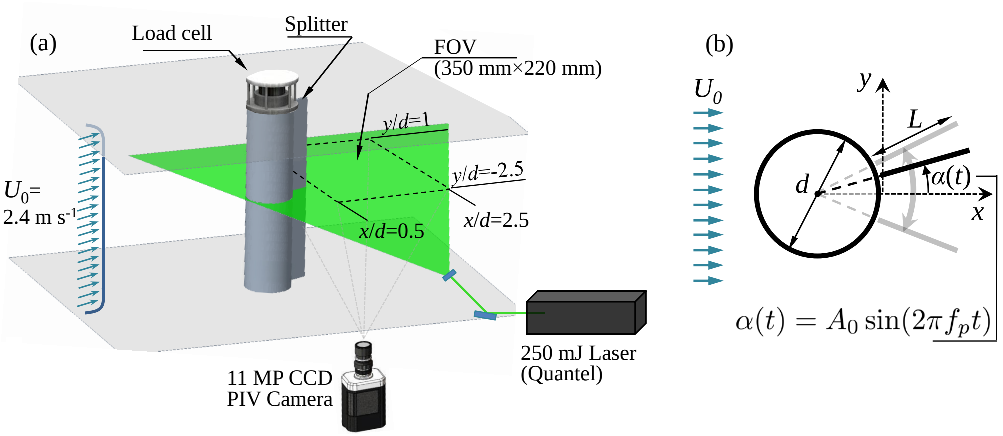

Figure 5.1: a) Schematic of the experimental setup illustrating a representative cylinder-splitter assembly and the field of view (FOV) of the PIV flow measurements. b) Plain view of the assembly showing basic parameters.

$\nu$ is the kinematic viscosity of air. The pitching oscillations of the plates were defined such that the relative angle of the plate with respect to the freestream flow was $\alpha(t) = A_0 \sin(2\pi f_p t)$, where $A_0$ and $f_p$ are the amplitude and pitching frequency. The flow field and mean drag of each of the three assemblies were characterized for $A_0 = 6^o$, $12^o$ and $18^o$, and non-dimensional pitching $f_p/f_v \in [1/4,\ 1]$ every $\Delta f_p/f_v = 1/8$. Here, $f_v$ is the associated vortex shedding frequency of the static assemblies ($\alpha = 0^o$); this resulted in Strouhal numbers of $S_t = f_v d/U_0 = 0.18$, 0.17 and 0.15 for the short, medium and long splitters. Overall, the parameter space of the experiments resulted in 63 distinctive cases.

The instantaneous drag of each assembly was obtained at a frequency of 2 kHz for 30 s with an uncertainty of 1% using a high-resolution ATI Gamma load cell connected at the top of the cylinder, and mounted outside of the test section [114]. In-plane velocity field measurements were acquired with a particle image velocimetry (PIV) system from TSI (figure 5.1a). The flow was seeded with 1 $\mu$m olive oil droplets generated by several Laskin nozzles placed upwind of the wind tunnel inlet. A 250 mJ pulse$^{-1}$ double-pulsed laser from Quantel was used to illuminate a field of view (FOV) of 350 mm × 220 mm, which covered a region of $x/d \in [0.5, 2.7]$ and $y/d \in [-2.5, 1]$ in the streamwise and spanwise directions. Here, the origin of the coordinate system was set at the rear side of the cylinder with the $x-$axis coincident with the direction of the mean incoming flow (figure 5.1b). For each case, two thousand image pairs were collected at a frequency of 1 Hz with a 11 MP (4000 × 2672) CCD camera. The image pairs were interrogated with a recursive cross-correlation method using Insight 4G software package from TSI. The final interrogation window resulted 24 × 24 pixels with 50% overlap, resulting in a final vector grid spacing $\Delta x = \Delta y = 1.25$ mm.

## 5.2 Results and discussion

### 5.2.1 Wake characteristics induced by the cylinder-splitter assemblies

The time-averaged and instantaneous features of the cylinder-splitter wake resulted very dependent on the relative length of the plates as well as the amplitude and frequency of their motions.

The impact of the active pitching on the streamwise velocity, $U/U_0$, is evidenced in figures 5.2−5.4 for selected cases. Each of them illustrates the effect of a single parameter, namely, $L/d$, $f_p/f_v$, and $A_0$. It is worth pointing out that $U/U_0$ is symmetric around $y = 0$ regardless of the case due to the symmetry of the motions and geometry of the assembly. In general, faster velocity recovery is induced with higher $L/d$, $f_p/f_v$, or $A_0$, independently. Each of these parameters imposed a dis-

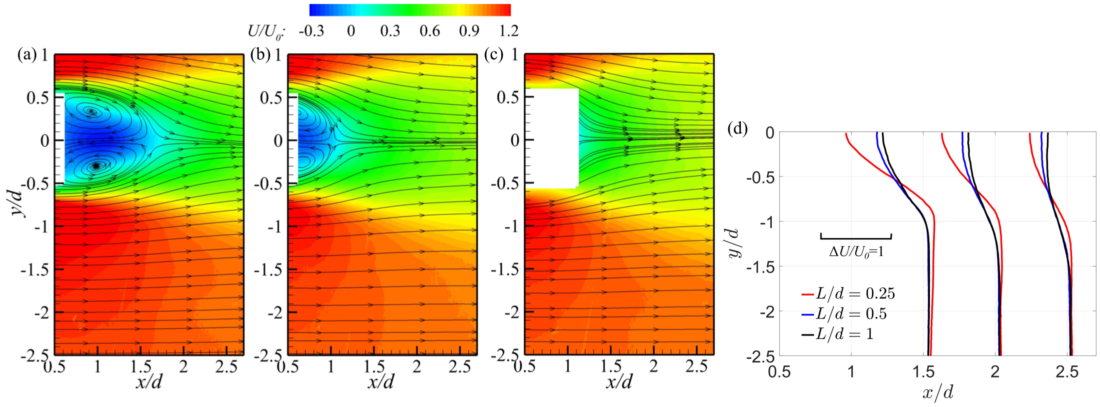

Figure 5.2: Time-averaged streamwise velocity distributions, $U/U_0$, past the cylinder-splitter assemblies sharing the oscillation patterns with $f_p/f_v = 1$ and $A_0 = 12^o$ but plate lengths of $L/d =$ a) 1/4, b) 1/2, and c) 1. d) Comparison of the spanwise velocity profiles at selected locations.

tinctive effect on the wake that resulted in enhanced mixing with respect to the base cases. In particular, figures 5.3 and 5.4 show a significant effect of $f_p/f_v$, and $A_0$ on the mean shear developed mostly within $|y/d| \in (0.5,\ 1)$; this effect, in turn, had a direct impact on the distribution of the kinematic shear stress (not shown for brevity).

Consistent with the modulation of the splitter dynamics on the mean velocity distribution, the flow fluctuations in the wake of the system also exhibited distinctive features. Bulk characterization of this quantity is given by the turbulence kinetic energy $TKE = \langle u'^2 + v'^2 \rangle / (2U_0^2)$, where $\langle\rangle$ is the temporal average operator, $u' = u - U$ and $v' = v - V$ are the streamwise and transversal velocity fluctuations. This is highlighted in Figure 5.5a-c for particular cases sharing the geometry ($L/d = 0.5$) and pitching frequency ($f_p/f_v = 1$) but varying $A_0$. It shows a $TKE$ increase with increasing $A_0$. This effect also occurred with $L/d$ and $f_p/f_v$, which are not shown here. Directional partition of the turbulence intensity in the streamwise ($I_u = \sigma_u/U_0$) and transversal ($I_v = \sigma_v/U_0$) directions, shown in figure 5.5d,e, reveals

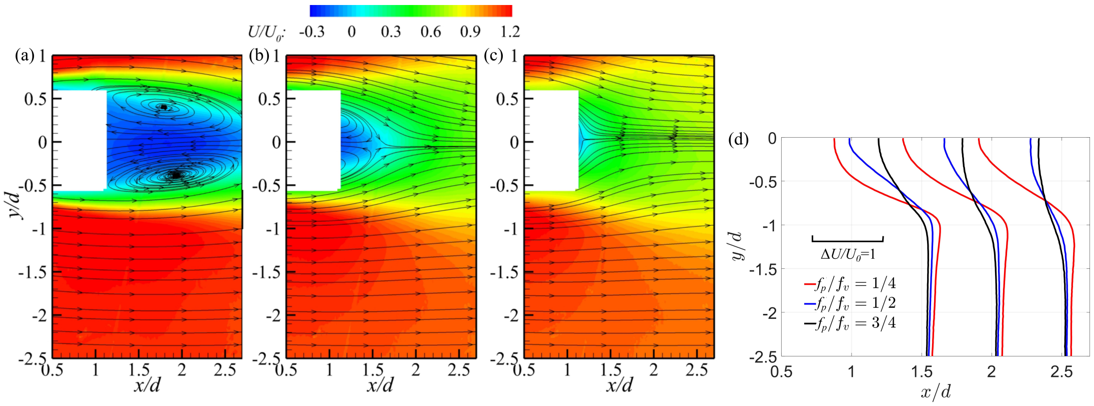

Figure 5.3: Time-averaged streamwise velocity distributions, $U/U_0$, past the cylinder-splitter assemblies sharing the $L/d = 1$ and $A_0 = 12^o$ but frequencies of $f_p/f_v =$ a) 1/4, b) 1/2, and c) 3/4. d) Comparison of the spanwise velocity profiles at selected locations.

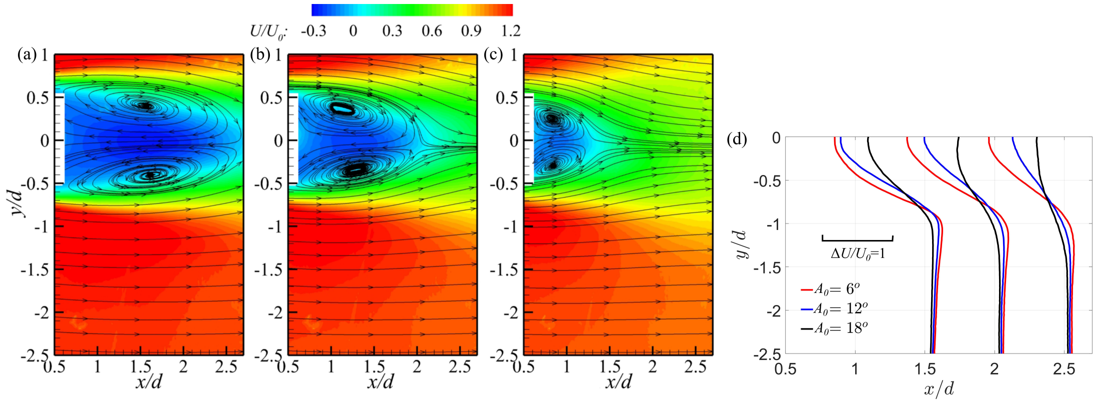

Figure 5.4: Time-averaged streamwise velocity distributions, $U/U_0$, past the cylinder-splitter assemblies sharing the $f_p/f_v = 0.75$ and $L/d = 0.5$ but $A_0 =$ a) $6^o$, b) $12^o$, and c) $18^o$. d) Comparison of the spanwise velocity profiles at selected locations.

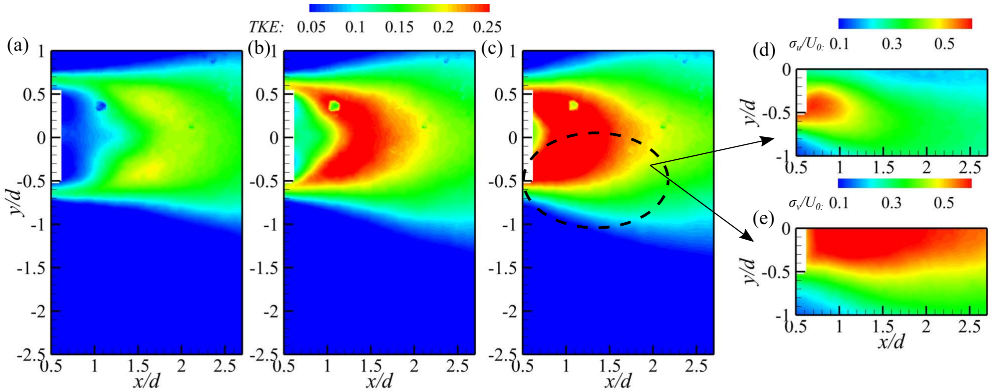

Figure 5.5: Turbulence kinetic energy, $TKE$, distribution past the cylinder-splitter assemblies sharing the $L/d = 0.5$ and $f_p/f_v = 1$ but $A_0 =$ a) $6^o$, b) $12^o$, and c) $A_0 = 18^o$. d-e) Turbulence intensity of the streamwise ($\sigma_u/U_0$) and transverse ($\sigma_v/U_0$) velocity fluctuations of case c).

the distinctive effect of each velocity fluctuations component in the $TKE$. Relatively strong transverse flow fluctuations dominated the near wake ($|y/d| \leq 0.5$), whereas this occurred only in the vicinity of $|y/d| \sim 0.5$ for the streamwise velocity fluctuations. Note that the tip velocity of the splitter is much larger in the transverse direction, with the maximum at $\alpha = 0$, resulting in significantly increased $I_v$ in the vicinity of the wake centerline.

The resulting turbulence levels in the system wake is a result of the active pitching modulation on the structure of the vortices; this is evidenced with representative snapshots of the out-of-plane signed swirling strength $\Lambda_{ci}$ [115, 116] normalized by $d/U_0$ in figure 5.6 for different cases. There, velocity vectors are superimposed to show the flow patterns. To highlight the influence of splitter motions, the snapshots share the splitter length ($L/d = 0.5$) and are taken at the instant coincident with $\alpha = 0^o$ and $d\alpha/dt > 0$, i.e., plate moving towards $y > 0$; the particular case with the static plate fixed at the wake centerline (figure 5.6a) is also added for comparison. In general, within a parameter space considering the $L/d \leq 1/2$, $A_0 \leq 12^o$ and

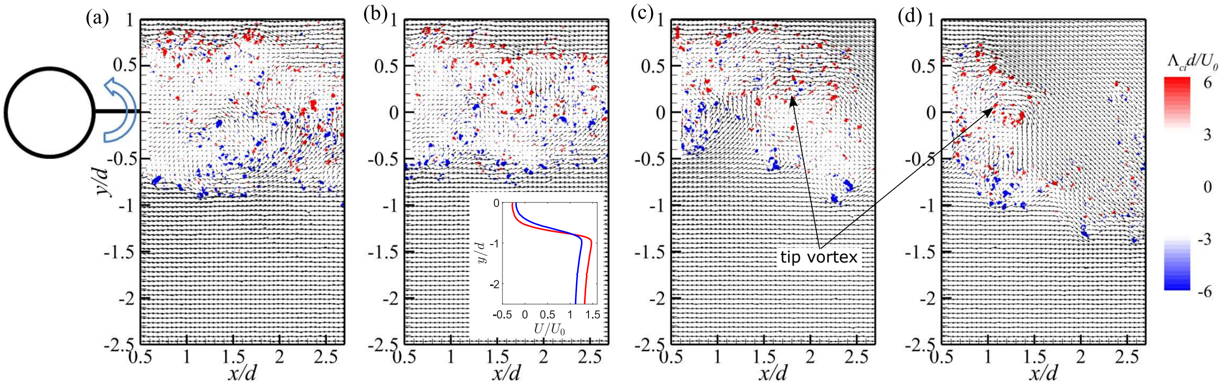

Figure 5.6: Snapshots of velocity fields with superimposed swirling strength with $L/d = 0.5$ and plates motions characterized by a) static plate; b) $A_0 = 12^o,\ f_p/f_v = 0.75$; c) $A_0 = 18^o,\ f_p/f_v = 0.75$; d) $A_0 = 12^o,\ f_p/f_v = 1$. The subplot in b) shows streamwise velocity $U/U_0$ profiles at $x/d = 1$ for the cases with the splitter static (red curve) and under pitching given by $A_0 = 12^o$ and $f_p/f_v = 0.75$ (blue curve).

$f_p/f_v \leq 0.75$, the general vortical structures in the wake exhibited similar patterns to those of the the base case (figure 5.6b). Secondary vortices of Kelvin-Helmholtz type shed from the cylinder rolled up to large-scale Von *Kármán* vortices. Note, however, that there are differences in the mean flow, as illustrated in the inset of figure 5.6b. At relative high pitching frequency and amplitude, the splitter induced distinctive wake meandering as illustrated in figure 5.6c,d. The maximum velocity of the splitter at the wake centerline induced significant velocity shear and momentum in the transverse direction; this is evidenced with the superimposed velocity vectors. These effects promoted the rolling-up of the coherent motions and the formation of large-scale wake meandering.

### 5.2.2 Mean drag of the system across splitter geometries and motions

The flow characteristics induced by the various active pitching resulted in distinctive drag coefficients, $C_d$, which varied with $L/d$, $f_p/f_v$, and $A_0$. This quantity is defined as

$$C_d = 2D/(\rho_a H d U_0^2), \tag{5.1}$$

where $D$ is the drag and $\rho_a$ is the air density. To explore a consistent relationship, we considered a form of the so-called amplitude-based Strouhal number, $St_A$, used in e.g., flapping foils [75]; it is essentially the product of the width-based Strouhal number $St_d = df_p/U$ and the dimensionless amplitude $A_D = 2A/d$, i.e.,

$$St_A = \frac{2Af_p}{U} \tag{5.2}$$

Here, $A$ is the tip amplitude of the foil and $U$ is the incoming velocity. As pointed out by [117], $St_A$ is central to describe the drag-thrust transition in flapping foils. In this cylinder-splitter system, the virtual length of the splitter with respect to the center of the oscillations is $L + d/2$; then, the equivalent $A = (L + d/2)\sin A_0$, and the dominant modulation of the cylinder suggests a velocity scale $U = f_v d$. It is worth to stress that $f_v$ is the vortex shedding frequency of the cylinder with fixed plate and changes with $L/d$.

Consequently, the corresponding system amplitude-based Strouhal number, $St_S$, that accounts for $f_p/f_v$, $L/d$ and $A_0$ may be expressed as follows:

$$St_S = \frac{f_p}{f_v}\frac{2(L + d/2)\sin A_0}{d}. \tag{5.3}$$

The $St_S$ results the product of the ratio of frequencies between the splitter pitching and vortex shedding (with static splitters), with the ratio between the transversal oscillation of the splitter tip and the cylinder diameter.

The associated drag coefficient $C_d$ for all the configurations as a function of $St_S$ are shown in figure 5.7a; those for the base cases with the splitter fixed at the wake centerline are also included for reference (dashed, horizontal lines). The distribution of $C_d$ exhibits particular features characterized by two regions limiting at $St_S \approx 0.2$. The first region, $R1$, defined by $St_S$ below this critical value, is characterized by approximately constant $C_d$; whereas the other region, $R2$, exhibits a linear relationship between $Cd$ and $St_S$. The constant value of $C_d$ within $R1$ indicates a minor influence of the splitter motions and wake characteristics similar to those of the fixed counterparts. In contrast, the behavior of $C_d$ in $R2$ reveals the substantial influence of the active plate pitching on the aerodynamics of the system.

To further explore the modulation of the active pitching on the wake characteristics and drag, we inspected the momentum integral equation [81], given by:

$$C_d = \frac{4}{d}\int_{y_w}^{0}\left[\frac{U}{U_0}(1-\frac{U}{U_0}) + \epsilon(1-\frac{U}{U_0}) + \frac{1}{2}(\frac{U_w^2}{U_0^2}-1) + \frac{\sigma_v^2-\sigma_u^2}{U_0^2}\right]dy. \tag{5.4}$$

The lower limit of the integral is taken at $y_w = -2.3d$; $U_w$ is the streamwise velocity at the limit of the integration $y = y_w$, and $\epsilon$ is defined as $\frac{1}{2}(U_0 + U_w) = (1-\epsilon)U_0$. Equation 5.4 uses the symmetry of the assembly and the velocity profile is taken at $x/d = 2.5$. Figure 5.7b shows the measured (solid symbols) and calculated (hollow symbols) $C_d$ for the cases in $R2$. In general, the estimated values agree well with the direct measurements of the drag. It is worth noting that integration at other locations also produced similar results, as seen in the subplot of figure 5.7b, which shows two examples sharing $L/d = 1$ and $A_0 = 12^o$ but $f_p/f_v = 0.625$

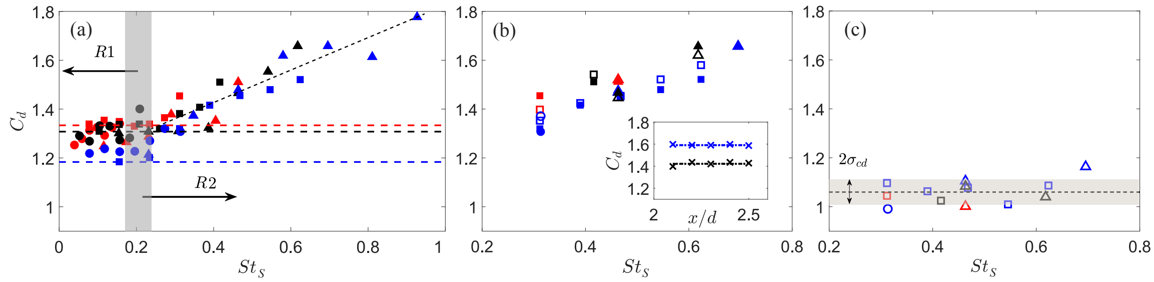

Figure 5.7: a) Distribution of the mean drag coefficient, $C_d$, as a function of the system amplitude-based Strouhal number $St_S$. The circle, square and triangles symbols represent cases with $A_0 = 6^o$, $12^o$ and $18^o$ with a variety of $L/d$ and $f_p/f_v$; whereas the red, black and blue symbols refer to $L/d = 0.25$, 0.5 and 1. The red, black and blue horizontal dashed lines correspond to the $C_d$ values of the static splitters with $L/d = 0.25$, 0.5 and 1. The inclined, dashed line in $R2$ denotes illustrates the basic trend. b) Comparison of the measured (filled symbols) and Eq. 5.4-calculated (empty symbols) $C_d$ within $R2$. The subplot illustrates examples of the $C_d$ calculated using the momentum integral equation at various locations for the cases sharing $L/d = 1$ and $A_0 = 12^o$ but $f_p/f_v = 0.625$ (black symbols) and $f_p/f_v = 1$ (blue symbols). c) Estimation of $C_d$ neglecting the flow fluctuation contribution.

(black symbols) and $f_p/f_v = 1$ (blue symbols). In the cases with static structures, the first term in the right-hand side of equation 5.4, i.e., mean flow, provides a good estimation of the drag [81, 118]. However, the high modulation of the active pitching leads to significant contribution of the flow fluctuations (fig. 5.5) in the momentum integral and, consequently, drag. There, the contribution from $\sigma_u$ and $\sigma_v$ are dominant. Such influence is illustrated in figure 5.7c, where the estimation of $C_d$ does not consider the term $(\sigma_v^2 - \sigma_u^2)/U_0^2$. Interestingly, despite the variations of $L/d$, $f_p/f_v$ and $A_0$, the $C_d$ resulted similar across $St_S$, within a standard deviation of $\sigma_{C_d}/C_d \approx 4\%$ (shown in the gray area of fig. 5.7c). This suggests the dominant role of the flow fluctuation on the increase of $C_d$ with $St_S$ in $R2$.

It is worth pointing out that the first three terms in equation 5.4 are determined by the distribution of $U(y)/U_0$; this indicates that the mean velocity profiles may share similar characteristics within $R2$ regardless of the splitter pitching. Figure 5.8a exhibits the distribution of $U/U_0$ along the wake centerline ($y = 0$) at $St_S = 0.16$ (with $L/d = 1, f_p/f_v = 0.5, A_0 = 12^o$), 0.23 (with $L/d = 0.25, f_p/f_v = 1, A_0 = 18^o$) and 0.31 (with $L/d = 0.5, f_p/f_v = 1, A_0 = 18^o$); clearly, those with larger $St_S$ leads to faster wake recovery and therefore higher $U/U_0$. However, very minor differences are observed when $U(y)$ is compared with profiles sharing similar streamwise velocity at the centerline $U(x, 0)$. For instance, figure 5.8b,d show the comparison of profiles of cases with distinctive pitching but with the same $U(x, 0)/U_0 = 0$ and 1/2. It suggests that the high-intensity splitter pitching induced an offset of the streamwise location of a given mean velocity profile $U(x_0, y)/U_0$. In contrast, the flow fluctuations term of the integral momentum equation, $(\sigma_v^2 - \sigma_u^2)$, exhibits distinctive differences dependent on the splitter motions (figure 5.8c,e). This leads to the variation of $C_d$ as shown in figure 5.7a,b. Finally, note that for cases under the

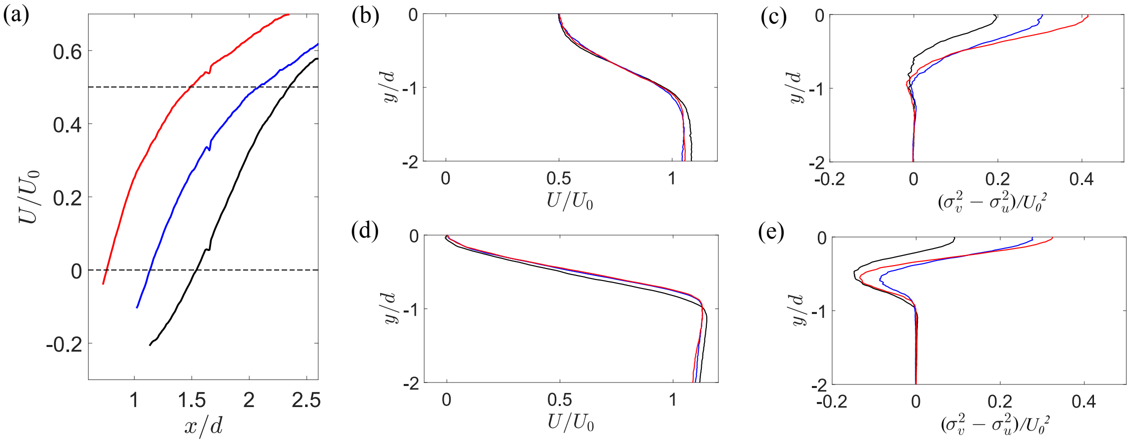

Figure 5.8: a) Selected streamwise profiles of the streamwise velocity, $U/U_0$, along the centerline ($y=0$). (b-c) Transverse profiles of $U/U_0$ and $(\sigma_v^2-\sigma_u^2)/U_0^2$ at streamwise locations sharing $U(x,0)/U_0=0.5$. (d-e) Same as (b-c) but with $U(x,0)/U_0=0$. The black, blue and red lines correspond to cases with $(L/d=1, f_p/f_v=0.5, A_0=12^o)$, $(L/d=0.25, f_p/f_v=1, A_0=18^o)$ and $(L/d=0.5, f_p/f_v=1, A_0=18^o)$.

same $St_S$, the velocity of the splitter tips $v_p=A_0(L+d/2)2\pi f_p\cos(2\pi f_p t)$ had similar standard deviation, which induce comparable wake fluctuations and, therefore, similar $C_d$. It is worth noting that at sufficiently high $St_S$, the wake may undergo comparatively fast flow recovery and eventually, there may be jet-like flow similar to the case of a single airfoil, where $C_d$ might eventually decrease with $St_S$. This possible phenomenon deserves further inspection.

## 5.3 Conclusion and remarks

The active pitching of splitters may induce distinctive modulation on the wake and flow patterns including meandering as well as on the drag of cylinder-splitter systems. This modulation may be set with combinations of the relative length of the splitter, amplitude and frequency of the pitching. By defining a system amplitude-based Strouhal number, $St_S$, that accounts for the geometry of the system and characteristics of the plate motions, we were able to express the drag coefficient, $C_d$, as a function of $St_S$. By doing this, it is possible to note distinctive trends of $C_d$ which are defined by a critical $St_S \approx 0.2$, which is remarkably similar to the basic Strouhal number value describing the oscillating flow past a cylinder over a wide range of Reynolds numbers.

The study provides specific insight for describing the impact of active plate pitching in the rear side of a cylinder, and the interdependence between wake features and drag of the system. The impact of Reynolds number, and very high $St_S$ in complex flows deserve close attention for inspecting the development of multipurpose flow-control strategies in a variety of environments.

# CHAPTER 6

# FLOW-INDUCED OSCILLATION OF A SINGLE WALL-MOUNTED FLEXIBLE PLATE

This chapter is from the Journal article: Jin Y., Kim J-T. and Chamorro L.P. "Instability-Driven Frequency Decoupling between Structure Dynamics and Wake Fluctuations". ***Phys Rev Fluids***, 3(4): 044701, 2018.

## 6.1 Experimental set-up

We first characterized the oscillation of four flexible structures fixed under uniform flow. The samples were placed in the freestream region of the Talbot Laboratory wind tunnel of the University of Illinois at Urbana-Champaign, which has a test section of 0.914 m wide, 0.45 m high and 6.1 m long. Two of them consisted on rectangular plates with different aspect ratios (henceforth wide and slender plates); the other two were made with triangular and trapezoidal shapes (fig. 6.1a). The plates shared the height $L = 240$ mm, thickness $c = 1$ mm, Young's Modulus $E = 2.7$ GPa and density $\rho = 1200$ kg m$^{-3}$. The plates were vertically mounted as a cantilever beam with the frontal area facing the incoming flow, where the boundary effect was negligible ($\sigma_U/U \sim 1\%$ across the sample height). The dynamics of each plate was characterized at various Reynolds numbers $Re = Ub/\nu \in [0.3\ 3.0] \times 10^4$, where $\nu$ is the kinematic viscosity of the fluid and $b$ is the base width of the plates.

A particle tracking velocimetry (PTV) system was used to track instantaneous

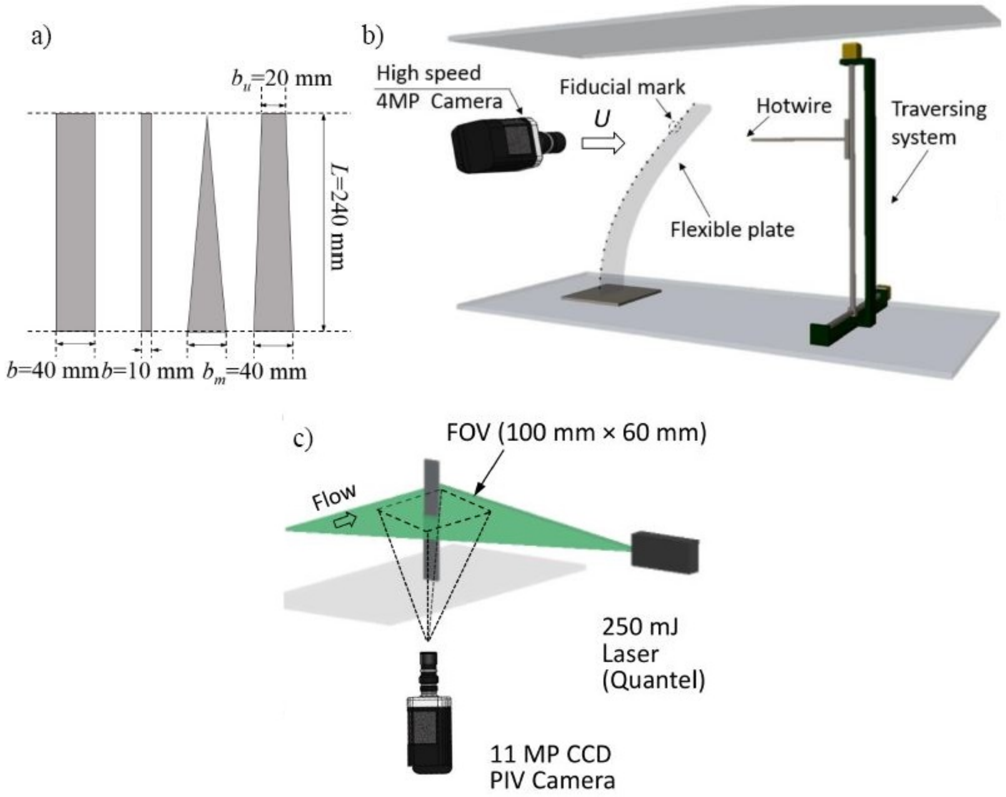

Figure 6.1: (a) Geometries of the four acrylic plates; (b) Schematic of experimental setup in the wind tunnel; (c) Schematic of experimental setup in the RIM flume.

motions of the fiducial points distributed along one side of the plates at a frequency of 300 Hz for periods of 30 s (fig. 6.1b). The flexible structures were illuminated by three Stanley Lithium Ion Halogen Spotlights and captured within an interrogation area of 260 mm by 160 mm using a Mikrotron EoSens 4CXP MC4082 high-speed camera at 4 MP resolution. A Nikon AF Micro-Nikkor 60 mm lens with a focal ratio f/2.8 was used to maximize the focus on the selected interrogation volume. The PTV data was processed using the open source software, OpenPTV (www.openptv.net). A hotwire anemometry was used to obtain vertical profiles of the flow along the central span of the plates at $x/L = 0.6$ downstream from the base. The probe is made of 5 mm tungsten wire and operated at a sampling frequency of 10 kHz for a period of 60 s in each location. The hotwire calibration was conducted against a pitot tube. The temperature was kept within $\pm 0.5^o$C to avoid errors due to thermal drift through the calibration and experiment. The anemometer was moved with a Velmex traversing system with position accuracy of 0.03% [119].

Complementary experiments were conducted in a 2.5 m long refractive-index-matching (RIM) flume with 112.5 mm × 112.5 mm cross section to inspect the influence of mass ratio. A NaI aqueous solution with density $\rho_f = 1800$ kg m$^{-3}$ and kinematic viscosity $\nu = 1.1 \times 10^{-6}$ m$^2$ s$^{-1}$ was used as the working fluid. A small rectangular flat plate of width $b = 10$ mm, height $L = 24$ mm, thickness $c = 0.125$ mm and the same Young's Modulus and density as those tested in the wind tunnel, resulting in very low mass ratio of 0.65. The instantaneous dynamics of the flexible plate was tracked at the tip using the PTV system across various $Re \in [2.7, 6.8] \times 10^3$. In addition, a high-resolution planar particle image velocimetry (PIV) from TSI was used to illustrate the wake characteristics of a rigid flat plate of width $b = 10$ mm (fig. 6.1c), which aided the discussion. A field of view (FOV)

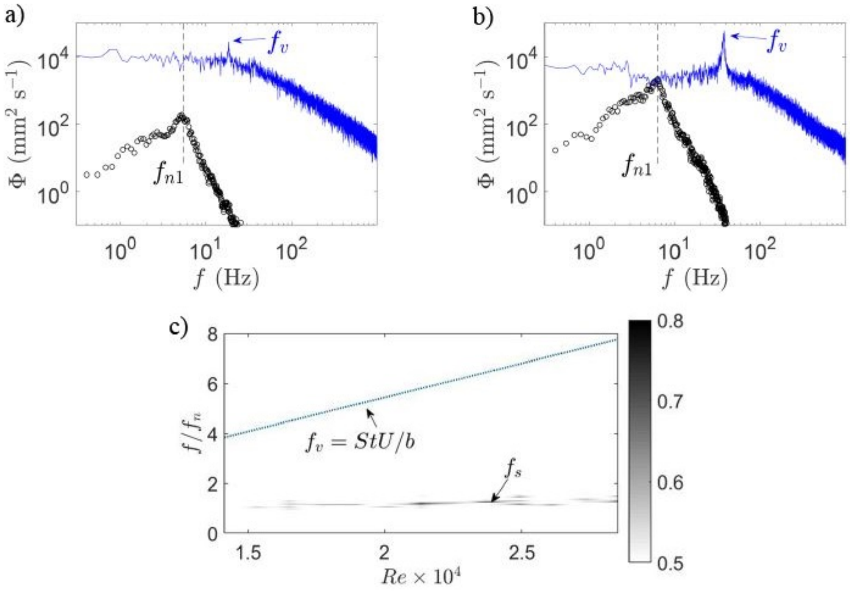

Figure 6.2: (a) Spectra of the streamwise velocity motion of the wide plate under $Re = 1.4 \times 10^4$ (○) and the wake fluctuations (−); (b) same as (a) under $Re = 2.9 \times 10^4$; (c) 2D spectrum of the structure motion highlighting the dominant oscillation frequency of the plate across various flow velocities. The blue dashed line indicates the vortex shedding frequency following $St = 0.145$.

of 100 mm × 60 mm was illuminated using a 1 mm thick laser sheet generated by a 250 mJ/pulse double-pulsed laser from Quantel. Two thousand image pairs were collected at $Re = 3.2 \times 10^3$ and a frequency of 1 Hz by an 11 MP CCD camera (fig. 6.1c). The interrogation window had a size of 24×24 pixels with 50% overlap, resulting in a vector grid spacing $\Delta x = \Delta y = 370$ $\mu$m.

## 6.2 Results

The motion of the wide rectangular plate is first characterized for various $Re$ to highlight the decoupling phenomenon. The oscillatory motions are defined respect to the equilibrium position, which undergoes monotonic deformation with increasing

$Re$. The body oscillations exhibit multi-scale features evidenced from the streamwise velocity spectrum of the motions, $\Phi(f_s)$. This is illustrated in figure 6.2a,b near the plate tip at $s/L = 0.9$, for two arbitrary $Re$; here $s$ is the intrinsic distance along the plate from the base. Note that despite one of the $Re$ doubles the other, each $\Phi$ exhibits a close dominant oscillation $f_{n1}$, which corresponds to the first-order natural frequency of the structure within the air medium. Inspection of the minor variation of the dominant frequency shows a mild increase with $Re$, which is much lower than that from the Strohal relation; this is clear from figure 6.2c.

The associated spectral distribution of the wake fluctuations $\Phi(f_w)$ is also presented in figure 6.2a,b. It reveals a distinctive dominating frequency $f_v$ much higher than $f_{n1}$ at both $Re$ with $f_v b/U \approx 0.145$ and following the Strouhal number reported by Knisely [108] and Norberg [120] for rectangular cylinders. It is worth pointing that similar phenomenon was observed across heights in all the investigated $Re$. The higher vortex shedding frequency compared to that of the structure oscillation indicates distinctive frequency decoupling; this motivates a revisit of the classic concept of coupling between flow and structures. Similar measurements were performed for the slender rectangular plate, triangular and trapezoid counterparts to test the general character of this phenomenon on thin, flexible structures. Figures 6.3a-c show selected spectra to demonstrate the concept. Like the case of the wide rectangular plate, the first-order natural frequency dominates the structure motion in all configurations, which is entirely decoupled from the dominating vortex shedding frequency measured in the wake (fig. 6.3d-f). It is worth pointing that the dominating vortex shedding frequency varies along the height of the triangular and trapezoidal plates due to the narrowing of the local width.

The governing equation of the dynamics of flexible structures oscillating in the

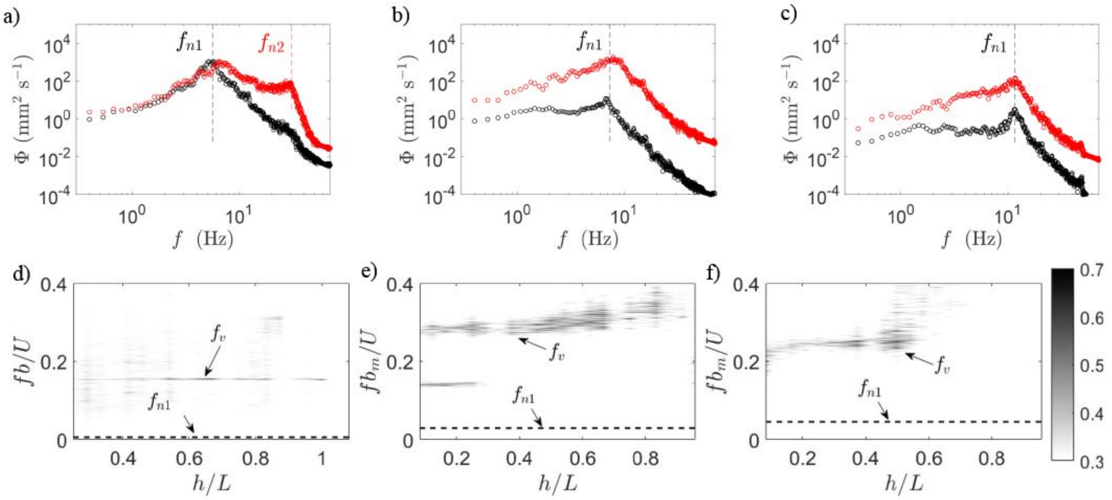

Figure 6.3: Streamwise velocity spectra under $U = 5.2$ m s$^{-1}$ (○) and $U = 10.2$ m s$^{-1}$ (○) for the (a) slender rectangular plate; (b) trapezoidal plate; (c) triangular plate. 2D pre-multiplied wake spectra for $U = 10.2$ m s$^{-1}$ along the height of the (d) rectangular, (e) trapezoidal and (f) triangular plates. The dashed lines indicate the dominating oscillation frequency of the plate from (a)-(c).

streamwise direction, around the equilibrium, can be approximated as:

$$\begin{gathered}\frac{\partial^2}{\partial s^2}(EI\frac{\partial\theta(s,t)}{\partial s}) + \rho_f A\frac{\partial x(s,t)^2}{\partial t^2} + \\ \beta\frac{\partial x(s,t)}{\partial t} = F(s,t)\end{gathered} \tag{6.1}$$

where $E$ is the Young modulus, $I$ is the second moment of area, $\theta = arcsin(\partial x/\partial s)$ represents the local bending angle relative to the vertical, $x(s,t)$ is the displacement in the flow direction, $\beta$ is the damping coefficient and $F$ is the external force. Here, we consider small oscillations around the equilibrium with $\frac{\partial\theta}{\partial s} \approx \frac{\partial^2 x}{\partial s^2}/\sqrt{1 - \langle\frac{\partial x}{\partial s}\rangle^2}$, where $\langle\cdot\rangle$ denotes time averaging. The solution of equation 6.1 can then be expressed in a discrete form as $[M]\ddot{\vec{x}} + [B]\dot{\vec{x}} + [K]\vec{x} = \vec{F}(t)$, where $[M]$, $[B]$ and $[K]$ are the mass, damping and stiffness matrices. With the modal analysis, the dynamics of the plates can be decoupled into their natural frequencies leading to:

$$\begin{aligned} \vec{x} &= [Q]\vec{\hat{x}} \text{ and} \\ \ddot{\hat{x}}_r + \gamma_r \dot{\hat{x}}_r + (2\pi f_{nr})^2 \hat{x}_r &= \hat{F}_r(t)/M_r, \end{aligned} \tag{6.2}$$

where $f_{nr}$ is the $r$th order natural frequency, $[Q]$ is the form matrix of the inherent oscillation modes and $\hat{x_r}$, $\gamma_r = Q^{(r)T}[B][Q]^{(r)}/M_r$, $\hat{F}_r(t) = [Q]^{(r)T}\vec{F}(t)$, $M_r = Q^{(r)T}[M][Q]^{(r)}$ are the corresponding displacement, damping coefficient, external force and mass in the decoupled system. The spectral characteristics of the oscillation velocity $\dot{\hat{x}}$ can be inferred with the Fourier transform ($\mathcal{F}$) of equation 6.2 as

$$|\mathcal{F}(\dot{\hat{x}})|^2 = (\frac{2\pi}{M_r})^2 \frac{|\mathcal{F}(\hat{F}_r)|^2 f^2}{[(2\pi f_{nr})^2 - (2\pi f)^2]^2 + (2\pi f \gamma_r)^2}. \tag{6.3}$$

Note that the oscillations in Fourier domain (eq. 6.3) are determined by the external forces (numerator) and the characteristics of the structure (denominator). For $f \to f_{nr}$, the denominator reaches the local minimum, indicating the dominant role of this frequency component. This is reflected by the distinctive first-order natural frequency $f_{n1}$ observed in figures 6.2 and 6.3. Note that for a relatively high $U$, the increasing $\theta$ leads to higher tension in the plate, resulting in the growth of $f_n$ for all configurations.

Clearly, the vortex shedding frequency detected in wake fluctuations is not directly reflected in the numerator of equation 6.3 for the structure oscillations. Govardhan & Williamson [10] pointed out that for VIV of circular cylinders, the mass ratio (between structure and fluid) could significantly influence the synchronization between the structure and wake; the dominating oscillation frequency can either be 'locked' close to the natural frequencies (high mass ratio) or approximately follow the Strouhal relation (low mass ratio) within the synchronization region. This factor was explored with additional measurements in the RIM flume. Figure 6.4a shows the streamwise velocity spectra for a rectangular plate under various incoming velocities. Despite the significant decrease of mass ratio, the dominant frequency also shows minor variation in the vicinity of $f_{n1}$ (note that $f_{n1}$ is modulated by the surrounding medium acting as added mass). This further suggests that periodic Strouhal-like wake fluctuations are plausible without the structure responding to such forcing; in contrast, the oscillations might be driven by flow instability. The high mean shear in the vicinity of the body induces flow instability that usually is followed by the well-known K*á*rm*á*n vortex shedding across various geometries [121, 111, 122]. This phenomenon is illustrated with wall-parallel PIV measurements around the structure (fig. 6.4b). It shows instantaneous vortical structures via the signed swirling strength $\Lambda_{ci}$, which is the magnitude of the imaginary part of complex eigenvalues of the local velocity gradient tensor [115]. Strong wake instability due to high velocity shear are dominant at $x/c \leq 2$, which modulates the streamwise structure oscillation. For $x/c \leq 2.5$, distinctive vortex shedding following the Strouhal relations occurs and does not directly influence the structure streamwise oscillation.

So far, we have shown that the footprint of the vortex shedding frequency following Strouhal relation on flexible structures oscillating in the streamwise direction for various geometries, $Re$ and mass ratio might be absent in the structure dynamics. It is worth pointing out that for most structures under uniform flow, the force fluctuations triggered by vortex shedding are more distinctive in the spanwise direction [113, 109], which results in classical VIV or galloping phenomena with wake-structure coupling. Here, we performed additional wind tunnel experiments with a circular cylinder over a short flexible plate parallel and perpendicular to

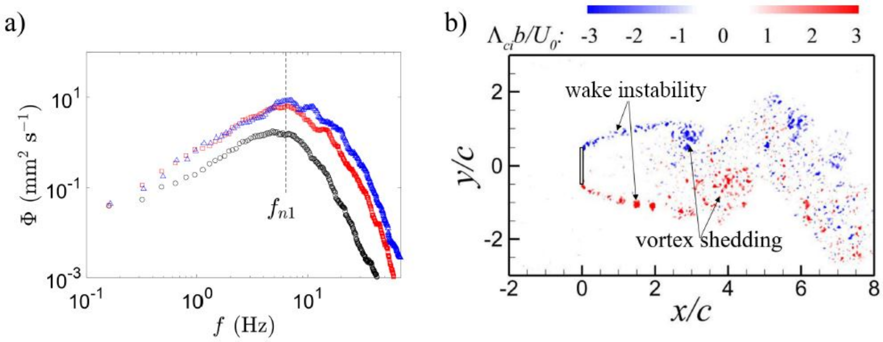

Figure 6.4: (a) Streamwise velocity spectra of the small rectangular plate with low-mass ratio at $Re = 3.4 \times 10^3$ (○), $4.8 \times 10^3$ (□) and $6.1 \times 10^3$(△). (b) Snapshot of the normalized swirling strength $\Lambda_{ci}b/U_0$ past the plate.

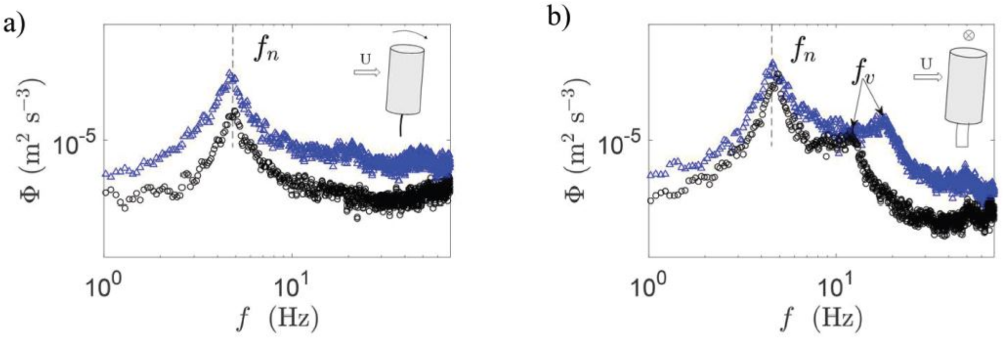

Figure 6.5: (a) Spectra of the oscillations of a circular cylinder under $U = 6.2$ (○) and 9.5 (△) m s$^{-1}$ with a support with a relative low stiffness in the streamwise direction. (b) Same case as (a) but low-stiffness support in the spanwise direction.

the flow to further investigate the effect of directional stiffness on the motion of structures. In this case, the cylinder was made with cardboard; it had a height of 250 mm, diameter 83 mm and average density of $\rho_m = 176$ kg m$^{-3}$. The supports consisted of comparatively short flexible plates of 60 mm length 35 mm wide and 6 mm thick. This allowed inspecting the motion with directional stiffness, one was to be order of magnitude larger than its perpendicular counterpart. The dynamics of the cylinder was recorded with a low weight, small accelerometer embedded inside the structure [123]. For the case with lower stiffness in the streamwise direction, the spectra of the cylinder motion exhibit similar behavior with one dominating frequency $f_n$ across $U$ (fig. 6.5a). In contrast, an additional dominant peak associated to the vortex shedding frequency following the Strouhal relation ($f_v$), as classical VIV cases, occurs with the lower stiffness in the spanwise direction (fig. 6.5b). Under this configuration, the strong vortex-induced force in the spanwise direction affects the motion of the structure. The coexistence of both $f_n$ and $f_v$ well reflects the influence of structure characteristics and Strouhal-type vortices; this is accounted in the numerator of equation 6.3. It is worth pointing out that the distinctive spanwise oscillation coupled with vortices might, in turn, enhance the wake fluctuations at $f_v$ in the vicinity of the structure. In 2D VIV cases, the streamwise oscillation also shows the footprint at $\sim 2f_v$ thus leading the well-known '8' shape of the structure trajectory [32, 105].

## 6.3 Conclusions and Remarks

The results presented here indicate that for the FIM cases restricted to move in the streamwise direction, wake instability plays a more significant role than the vortex shedding in the structure motion, where the wake-structure decoupling occurs. This phenomenon of common occurrence in natural systems might be explored in more detail in engineering. In many slender vegetation under strong wind, high-frequency vortex shedding following Strouhal relation might easily lead to structural fatigue; the decoupling of oscillations 'locked-in' their natural frequencies might help them to by-pass extreme conditions. For energy harvesting with flexible structures, the highlighted natural frequencies during oscillations shed light into the optimal design via resonance to maximize the power output. A recent study by Jin *et al.* [124] showed that body oscillations under high turbulence level ($I_u$), the structure motions are strongly modulated by the energy-containing eddies and inertial subrange of the incoming velocity spectrum, which is reflected in $\mathcal{F}(\hat{F}_r)$ of equation 6.3. Here, the oscillations with low $I_u$ also present power law decay behavior under various $Re$; this implies that the wake instability at the vicinity of structures might induce related effects, which provides potential for the prediction of the general structure response under various configurations. Finally, the quantitative prediction for the occurrence of high-order natural frequencies, and their modulation on the power law decay motivates further inspection of the phenomenon.

# CHAPTER 7

# COUPLE DYNAMICS OF WALL-MOUNTED FLEXIBLE PLATES IN TANDEM

This chapter is from the Journal article: Jin Y., Kim J-T., Mao Z. and Chamorro L.P. ”On the couple dynamics of wall-mounted flexible plates in tandem”. ***J Fluid Mech (rapids)***, 852: R2, 2018.

## 7.1 Experimental Setup

Two rectangular, flexible plates were mounted vertically at the bottom wall of a 2.5 m long, 112.5 mm × 112.5 mm cross-section refractive-index-matching (RIM) flume. The structures were placed facing the flow in tandem configuration at the centerline and near the entrance of the fume. There, the incoming flow was nearly uniform with negligible turbulence. A NaI aqueous solution with density of $\rho_f = 1800$ kg m$^{-3}$ and kinematic viscosity $\nu = 1.1 \times 10^{-6}$ m$^2$ s$^{-1}$ was used as the working fluid. This allowed index matching between the flume walls, structures and solution fine-tuned via temperature control, which resulted in measurements very close to the surface of plates. More details about RIM technique can be found in Bai & Katz [125]. The plates were made from acrylic and had the same height $h = 40$ mm, width $b = h/4$, thickness $c = 0.125$ mm, Young's Modulus $E = 2.7$ GPa and density $\rho_m = 1200$ kg m$^{-3}$.

The coupled dynamics of the structures and flow was studied for three spacings

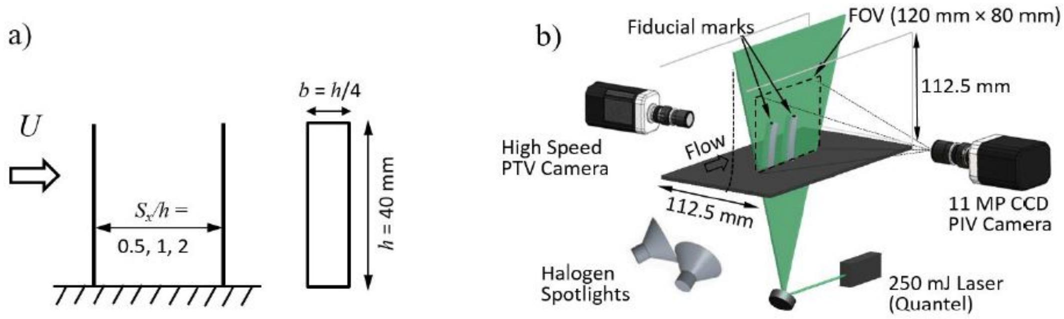

Figure 7.1: a) Layout and geometry of the flexible plates; b) basic schematic of the experimental setup.

$s_x = \Delta x/h = 0.5$, 1 and 2 (henceforth small, intermediate and large separations, see Fig. 7.1a) at various incoming velocities $U_0 \in [0.24, 0.54]$ m s$^{-1}$ every $\Delta U_0 = 0.05$ m s$^{-1}$, which corresponded to $Re = U_0 b/\nu \in [2.2, 5] \times 10^3$ or Cauchy numbers $Ca = \rho_f b U_0^2 h^3/(EI) \in [15, 77]$ [86]. Here, $I = bc^3/12$ is the second moment of the area. For each setup, the motion of the plates was tracked synchronously at a frequency of 300 Hz for sampling periods over 30 s (i.e., over 9000 instants) with a particle tracking velocimetry (PTV) system. It used a Mikrotron EoSens 4CXP MC4082 camera at 2 MP resolution, a Nikon AF Micro-Nikkor 28mm lens that maximized the focus of an interrogation area of 120 mm by 60 mm and illumination provided by two Stanley Lithium Ion Halogen Spotlights. A fiducial point was carefully marked at the center of each plate tip to track the motions. The PTV calibration was carried out with a pixel to distance ratio of 0.06 mm/pixel, and data were processed with the open source software, OpenPTV. Figure 7.1b illustrates the basic setup of the two-plate system.

The flow in the vicinity of the two plates was characterized with a high-resolution planar PIV from TSI within a wall-normal plane coinciding with the center of both plates. A field of view (FOV) of 120 mm × 80 mm was illuminated with a 1 mm thick laser sheet induced by a 250 mJ/pulse double-pulsed laser from Quantel. For each case, two thousand image pairs were collected at a frequency of 1 Hz with a 11 MP CCD camera. A recursive cross-correlation method was applied to interrogate the image pairs via Insight 4G software from TSI. The final interrogation window had a size of 24 pixels × 24 pixels with 50% overlap, resulting in a vector grid spacing of $\Delta x = \Delta y = 420$ $\mu$m.

## 7.2 Results

In this section, we characterize and analyze the distinctive dynamics of the plates and induced flow as a function of $Ca$ and $s_x$. For all the cases studied, the plates exhibited oscillations in the streamwise direction due to the relatively low aspect ratio of the structures and the much lower stiffness in the direction of the mean flow; here, torsional and spanwise motions were absent. For clarity, the description is split in terms of $s_x$ due to its role on the distinctive coupling of the plates.

### 7.2.1 Interaction of the plates with small separation, $s_x = 0.5$.

A first-order assessment of the plates motion as a function of $Ca$ is given with the time-averaged position of the tips $\vec{X}_0 = (X_0, Y_0) = \langle x, y \rangle_{tip}$ in figure 7.2a. The downstream plate (hereon $P_d$) underwent lower mean deformations due to the locally reduced incoming flow. This is illustrated with the streamwise velocity distribution $U/U_0$ in figure 7.2b,c for two $C_a$; there, streamlines are included to better visualize the mean flow features. Most of the $P_d$ was located within the back-flow region, i.e., $U(x, y) \leq 0$, induced by the upstream plate (hereon $P_u$). Only the vicinity of the tip was exposed to the nearly undisturbed flow. The relatively short gap between

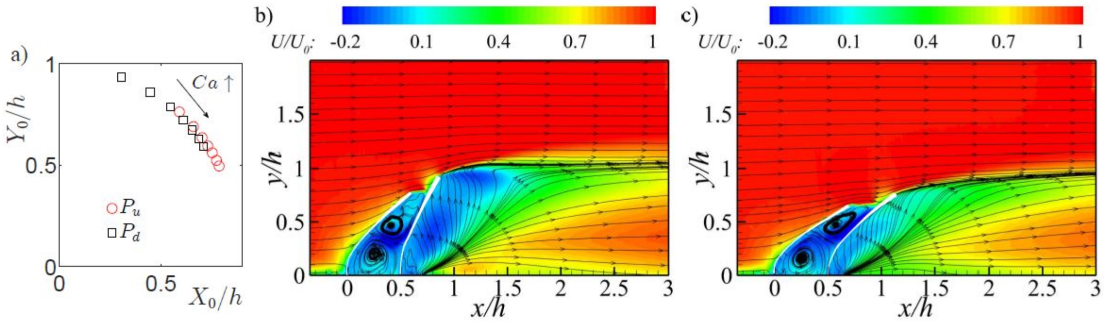

Figure 7.2: a) Time-averaged tip position $(X_0, Y_0)$ of the upstream $(P_u)$ and downstream $(P_d)$ plates for $Ca \in [15,\ 77]$; b) streamwise velocity distribution $U/U_0$ at $Ca = 15$; c) $U/U_0$ at $Ca = 30$. Cases with $s_x = 0.5$.

the plates also promoted the formation of two recirculation regions, which was not present with larger $s_x$ (shown later).

Bulk characterization of the dynamics of the plates was obtained via the intensity of the tip displacements $I_{tip} = ||\vec{x}(t) - \vec{X}_0||/h$, where $||\cdot||$ denotes the $L^2$-norm and $\vec{x}$ is the instantaneous location of the tips. Notably, both plates exhibited very similar $I_{tip}$, which increased monotonically with $Ca$ (see Fig. 7.3a). The plates also showed high degree of coupling, as evidenced by the cross-correlation of the tips $\gamma_{p_u,p_d}(\tau) = \langle x_{p_u}(t)x_{p_d}(t+\tau)\rangle$ in figure 7.3b for three $Ca$. Indeed, peak values resulted $\gamma_{p_u,p_d}(\tau = t_a) > 0.65$, with higher values at lower $Ca$. The characteristic time shift $t_a$ is associated to the mean advection of the footprint of $P_u$ on $P_d$ and, consequently, decreased with increasing $Ca$.

The dominant modes of oscillation of the plates across $Ca$ are shown in figure 7.3c,d with the compensated spectra $f\Phi/max\{f\Phi\}$ of the streamwise displacements of the tip. In general, the upstream plate presented roughly similar features across $Ca$ with the dominating modes close to its first-order natural frequency $f_{n1}$; however, energetic modes at higher frequencies occurred in the downstream structure. The fundamental frequency $f_{n1}$ is modulated by the surrounding medium acting as added

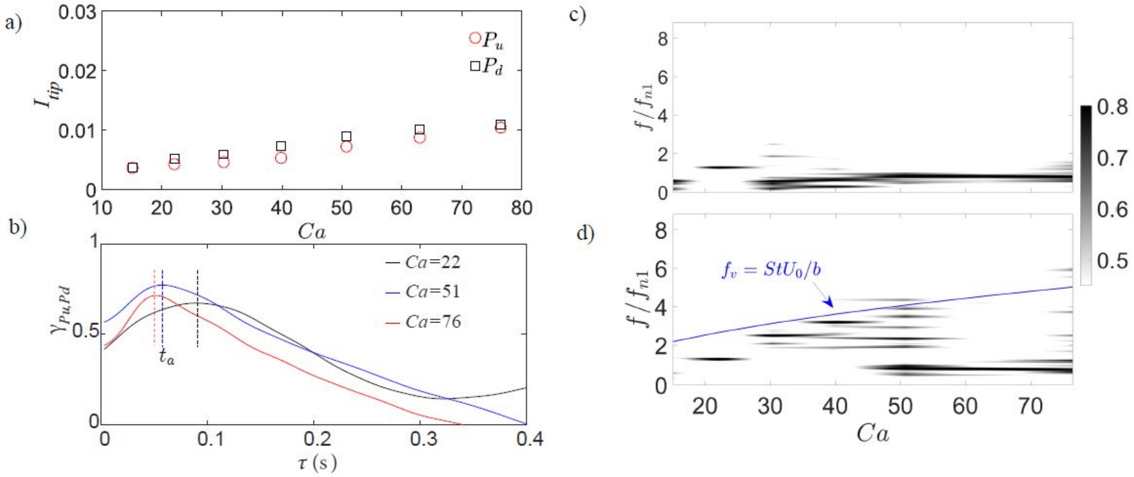

Figure 7.3: a) Intensity of the tip motions $I_{tip}$ across $Ca$ for the two plates; b) cross-correlation function $\gamma_{p_u,p_d}(\tau)$ for selected $Ca$; c) 2D compensated spectra of the tip displacements of the $P_u$ plate; d) same as c) for the $P_d$ plate; Cases with $s_x = 0.5$.

mass and damping; it is given by:

$$f_{n1}/f_{n1o} = \sqrt{1-\xi^2}, \text{ where } f_{n1o} = \frac{0.56}{h_{rec}^2}\sqrt{\frac{EI}{\rho_m bc + \rho_f C_m \pi b^2/4}}. \tag{7.1}$$

Here, $C_m = 1$ [86], $\xi$ is the damping ratio determined by the dominant oscillation frequency of a single plate under uniform flow. Our experiments indicate that $\xi = 0.43$ is a good estimation. Evidence indicates that for structures in tandem with sufficiently small separation, von Kármán vortex shedding can be induced only in the wake of the downstream structure [126, 127, 92, 128]. There, the gap may be dominated by small-scale Kelvin-Helmholtz ($K - H$) instability [129, 130]. A similar phenomenon occurred with the plates for the $s_x = 0.5$ cases, where the dynamics of $P_u$ were governed by $f_{n1}$ [124, 123]. Distinctive vortex shedding was induced in the very near wake of the downstream structure, whose footprint is observed in figure 7.3d. The vortex shedding frequency ($f_v$) did not strictly follow

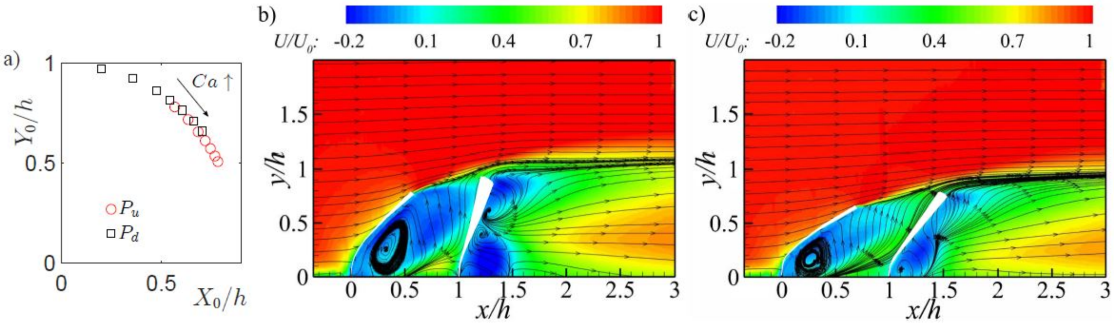

Figure 7.4: Time-averaged tip position $(X_0, Y_0)$ of the upstream ($P_u$) and downstream ($P_d$) plates for $Ca \in [15,\ 77]$; b) streamwise velocity distribution $U/U_0$ at $Ca = 15$; c) $U/U_0$ at $Ca = 30$. Cases with $s_x = 1$.

the Strouhal relation $St = f_v U_0/b = 0.15$ (blue curve in Fig. 7.3d) suggested by Knisely [108] and Norberg [120] for rigid plates. The differences on $St$ were likely due to the changes of the gap between the two plates across $Ca$. Finally, it is worth pointing out that for sufficiently low $Ca$ ($\leq 30$), the $P_d$ was able to induce some backward modulation on $P_u$, as suggested in figure 7.3c. This may be attributed to the comparatively smaller tip distance between the plates, shown in figure 7.2a. The increase of $s_x$ is expected to severely condition the strong coupling of the structures and the turbulence-induced forcing on $P_d$; this is explored as follows.

### 7.2.2 Interaction of the plates with intermediate separation, $s_x = 1$.

The increase of the plate separation to $s_x = 1$ or, equivalently, 4 times the plate's width, led to very distinctive motions. Despite that $P_u$ exhibited similar levels of deformation across $Ca$ as those of the $s_x = 0.5$ cases (Fig. 7.4a), $P_d$ underwent smaller bending. This interesting phenomenon is explained by inspecting the streamwise velocity distribution shown in figure 7.4b,c. Despite that the larger separation allowed a recovery of the bulk flow impinging $P_d$, the flow in the vicinity of the $P_d$ tip was

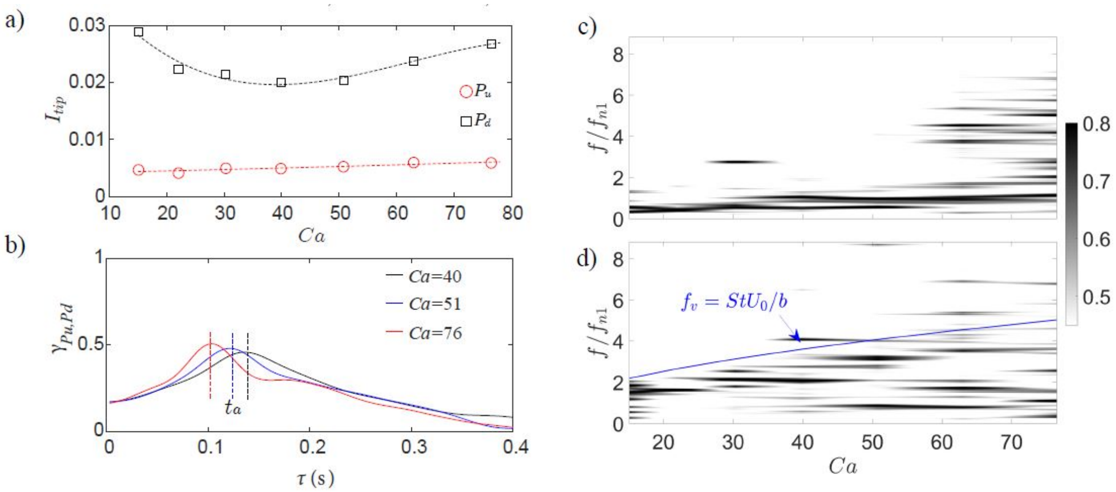

Figure 7.5: a) Intensity of the tip motions $I_{tip}$ across $Ca$ for the two plates; b) cross-correlation function $\gamma_{p_u,p_d}(\tau)$ for selected $Ca$; c) 2D compensated spectra of the tip displacements of the $P_u$ plate; d) same as c) for the $P_d$ plate; Cases with $s_x = 1$.

significantly lower due to the vertical diffusion of the wake. This stresses the dominant role of the flow near the tip region. Note also that, compared to the $s_x = 0.5$ cases, the velocity deficit distributed more uniformly at the location of $P_d$. Similar to cylinders in tandem [126, 128], larger $s_x$ facilitates the production of vortices within the gap of the two plates; consequently, the $P_d$ structure is more susceptible to vortex-induced fluctuations. This resulted in a large impact on $I_{tip}$, $\gamma_{p_u,p_d}(\tau)$ and the dominant modes of oscillation. Indeed, the $I_{tip}$ of $P_d$ exhibited distinctive trend compared to the $s_x = 0.5$ cases characterized by a concave distribution with a local minimum at intermediate $Ca$ (see Fig. 7.5a); analysis of this phenomenon will be elaborated below. Also, loss of coupling between $P_u$ and $P_d$ is evident from a reduction in the peak of $\gamma_{p_u,p_d}(\tau)$ (see Fig. 7.5b). The direct impingement of the vortex shedding from $P_u$ induced a strong footprint on the dynamics of $P_d$ approximately following $St = 0.15$ (Fig. 5d). Comparatively, the oscillations of $P_u$ presented clear

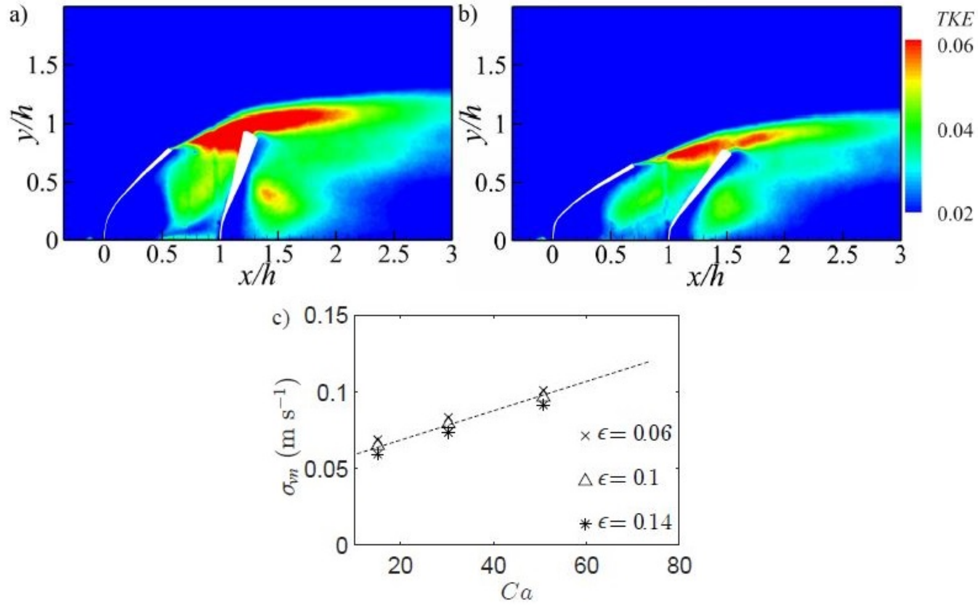

Figure 7.6: a) Turbulence kinetic energy ($TKE$) distribution for $Ca = 15$; b) same as a) but $Ca = 30$; c) average intensity of the velocity normal to the plate within a circular region centered at the tip with radius $R = \epsilon h$ for various $\epsilon$. Cases with $s_x = 1$.

signature near $f_{n1}$ across $Ca$ (Fig. 5c). Usually for structures under uniform flow, the von Kármán vortex shedding triggers more distinctive force fluctuations in the spanwise direction [113, 109, 22], where its footprint is comparatively minor in the streamwise-dominated oscillations. There, Kelvin-Helmholtz ($K - H$) instability within the very near wake of $P_u$ may govern the plate dynamics. Note, however, that larger amplitude of oscilation of $P_d$ may eventually alter the dynamics of $P_u$, as noted in the compensated spectrum of the tip motion in Fig. 7.5c for high $Ca$.

The concave distribution of the tip intensity deserves a close inspection due its impact on various natural and engineering systems. The dynamics of structures in the wake of other bodies is substantially modulated by the velocity fluctuations and the structure stiffness. In particular, comparatively higher turbulence kinetic energy

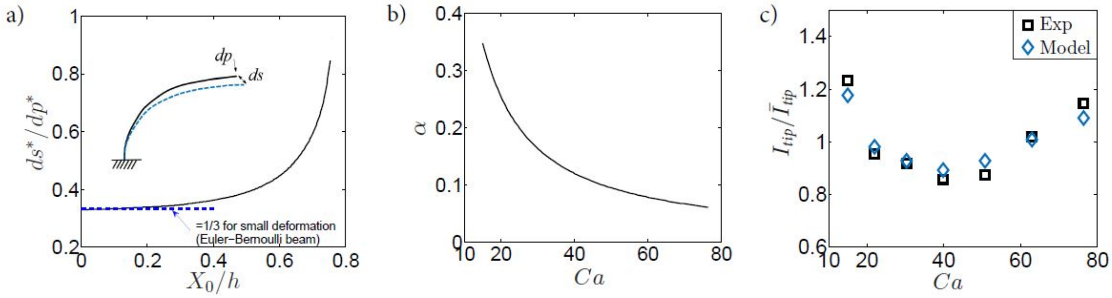

Figure 7.7: a) Local bending stiffness $ds^*/dp^*$ as a function of $X_0/h$; b) driven-harmonic-oscillator frequency response function $\alpha$ for the plate across $Ca$; c) modeled and measured tip oscillation intensity $I_{tip}/\bar{I}_{tip}$. Cases with $s_x = 1$.

$TKE = \frac{1}{2}\langle u'^2 + v'^2 \rangle / U_0^2$ in this two-plate system is located in the vicinity of the tip of $P_d$ (see two examples in Fig. 7.6a,b). Here, the streamwise ($u'$) and vertical ($v'$) components of the velocity fluctuations may significantly affect the oscillations of $P_d$. If we consider that the dynamics of this plate is driven by the velocity fluctuations perpendicular to the tip vicinity $v_n$ (namely, normal to the tangent vector of the plate approaching to the tip), a bulk effect is given by the standard deviation $\sigma_{vn}$ within a region around the tip; i.e., $\langle q \rangle \propto \sigma_{vn}^2$, where $q$ is the fluctuating force. A region around the tip may be considered as a circular domain centered at the tip with radius $R = \epsilon h$ with $\epsilon \ll 1$. Here, $\epsilon = 0.1 \pm 0.04$ resulted in very consistent trend for estimating $\sigma_{vn}$, which increased linearly with $Ca$ (see Fig. 7.6c).

Now, the model by Chen [131] shows that for sufficiently large external forcing, a cantilever beam may undergo large deformation with strong nonlinear behavior of the tip displacements. This model is used to estimate the differential tip displacement $ds$ as a result of a differential force $dp$ normal to the tip ($ds/dp$) for a given mean streamwise deformation of the structure $X_0$. This is illustrated in figure 7.7a in non-dimensional form; i.e., $ds^*/dp^* = ds/dp(EI/h^3)$ as a function of $X_0/h$. Note that for small plate deformation $ds^*/dp^* \to 1/3$, which agrees with that from the

Euler-Bernoulli beam theory. It is also worth stressing the distinctive increase of $ds^*/dp^*$ for $X_0/h > 0.5$, which facilitates the occurrence of large-amplitude oscillations. As inferred from figure 7.5d, the dynamics of $P_d$ is strongly modulated by the vortex shedding frequency from $P_u$. This modulation may be thought as a case of a driven harmonic oscillator ($DHO$); consequently, the frequency shedding defines the response function of the steady-sate solution of the $DHO$, as follows:

$$\alpha = \frac{1}{\sqrt{(1-\gamma^2)^2 + (2\xi\gamma)^2}} \tag{7.2}$$

where $\gamma = f_v/f_{n1o} \approx StU_0b/f_{n1o}$ is the frequency ratio. Then, as $f_v$ departs from $f_{n1o}$ with increasing $Ca$, the response function $\alpha$ decreases monotonically (Fig. 7.7b). Hence, the combined effect of the flow fluctuations, structure stiffness and dominant shedding frequency on $I_{tip}$ of $P_d$ can be approximated to:

$$I_{tip|P_d} \propto \sigma_{vn}^2 \frac{ds^*}{dp^*} \alpha \tag{7.3}$$

Figure 7.7c illustrates the estimated and measured $I_{tip}$, normalized with mean value $\bar{I}_{tip}$ across $Ca$. It shows a good trend which explain the concave behavior of $I_{tip}$; namely, for relatively low $Ca$, $dI_{tip}/dCa < 0$ is governed by the comparatively fast reduction of $\alpha$, whereas for relatively high $Ca$, $dI_{tip}/dCa > 0$ is modulated by non-linear effects of the structure bending ($ds^*/dp^*$).

### 7.2.3 Interaction of the plates with large separation, $s_x = 2$.

Larger plate separation to $s_x = 2$ resulted in substantial recovery of the flow impinging $P_d$; as a result, both plates exhibited minor differences in $\vec{X}_0$ across $Ca$ (see Fig. 7.8a). Like the $s_x = 1$ cases, the $P_d$ was fully within the wake (Fig. 7.8b,c).

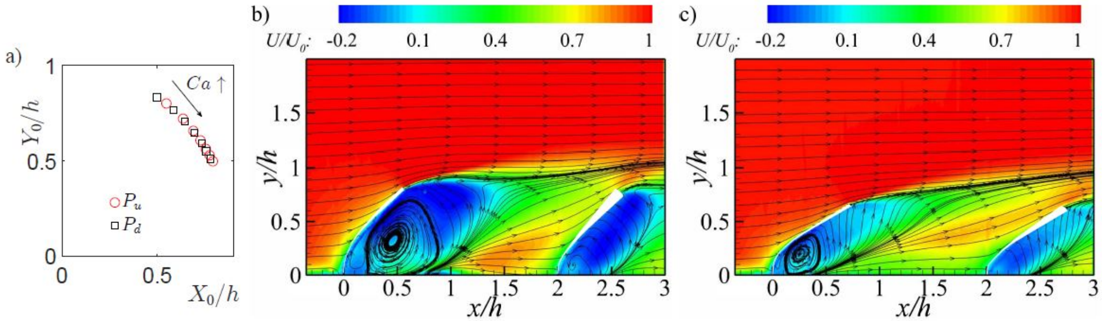

Figure 7.8: a) Time-averaged tip position $(X_0, Y_0)$ of the upstream $(P_u)$ and downstream $(P_d)$ plates for $Ca \in [15,\ 77]$; b) streamwise velocity distribution $U/U_0$ at $Ca = 15$; c) $U/U_0$ at $Ca = 30$. Cases with $s_x = 2$.

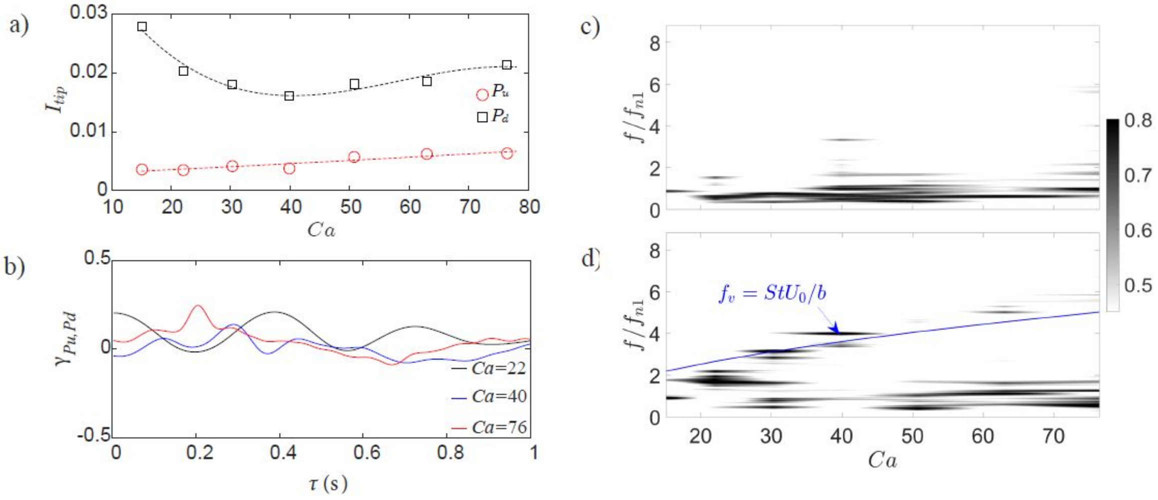

Figure 7.9: a) Intensity of the tip motions $I_{tip}$ across $Ca$ for the two plates; b) cross-correlation function $\gamma_{p_u,p_d}(\tau)$ for selected $Ca$; c) 2D compensated spectra of the tip displacements of the $P_u$ plate; d) same as c) for the $P_d$ plate; Cases with $s_x = 2$.

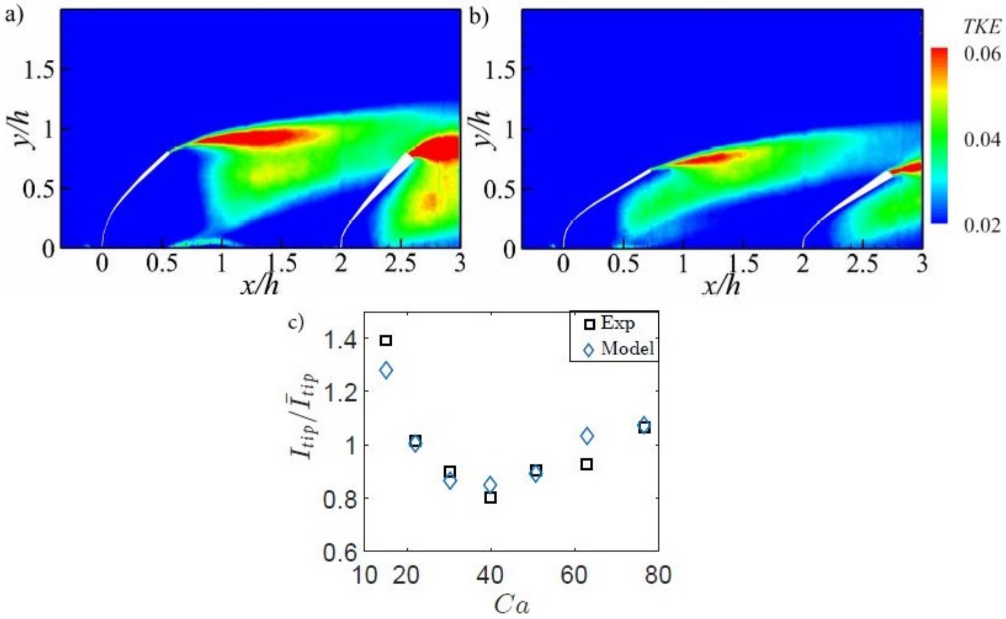

Figure 7.10: a) Turbulence kinetic energy ($TKE$) distribution for $Ca = 15$; b) same as a) but $Ca = 30$; c) modeled and measured tip oscillation intensity $I_{tip}/\bar{I}_{tip}$. Case with $s_x = 2$.

In general, the distinctive trends of $I_{tip}$ for $P_u$ and $P_d$ are similar to those of the $s_x = 1$ cases (Fig. 7.9). However, that for $P_d$ resulted lower at relatively high $Ca$ due to a reduced effect of the wake fluctuations $\sigma_{vn}$ near the tip. Indeed, distinctive differences of the $TKE$ near the tips are evident in Figs. 7.10a and 7.10b; this phenomenon is also predicted by the model based on equation 7.3 (Fig. 7.10c). The large separation equivalent to 8 times the plate width resulted in very weak coupling dynamics between $P_u$ and $P_d$ (Fig. 7.9b). Like the other configurations, $P_u$ was dominated by frequencies around $f_{n1}$ across $Ca$ (Fig. 7.9c). This evidences that flow instability in the very near wake region of the flexible plate is more significant than the vortex shedding in streamwise-dominated oscillations. Comparatively, $P_d$ was modulated by both vortex shedding and the natural frequency (Fig. 7.9d).

## 7.3 Conclusions and Remarks

Inspection of the plate motions and surrounding flow provided new qualitative and quantitative elements towards uncovering the complex dynamics of flexible structures in tandem. The analysis revealed the distinctive modulation of the upstream plate on the dynamics of the downstream one. For the various $Ca$ and $s_x$ explored, the oscillations of the upstream plate were, in general, governed by its natural frequency, whereas the downstream plate also presented clear footprint of vortex shedding. Interestingly, the downstream plate exhibited an oscillation intensity with concave distribution as a function of $Ca$ for intermediate and large separations ($s_x = 1, 2$). This is due to a combination of multiple factors, including the velocity fluctuations, vortex shedding and substantial changes on the structure stiffness induced by large-amplitude deformation. This is explained via a simple model. As pointed out by Luhar & Nepf [5], the aspect ratio, stiffness and mass ratio are also important factors defining the dynamics of flexible structures. The characteristic impact of each of these factors in the unsteady dynamics of structures is out of the scope of this work and deserves close inspection.

# CHAPTER 8

# FLUTTERING, TWISTING AND ORBITAL MOTIONS OF FLEXIBLE PLATES

This chapter is from the Journal article: Jin Y., Kim J-T., Fu S. and Chamorro L.P. "Flow-induced motions of flexible plates: fluttering, twisting and orbital modes". ***J Fluid Mech***, 864: 273-285, 2019.

## 8.1 Experimental Setup

Selected laboratory experiments were conducted in the freestream region of the Talbot wind tunnel at the University of Illinois. The wind tunnel has a test section 6 m long, 0.46 m high and 0.914 m wide.

A flexible flat plate made of acrylic was mounted over a Velmex rotary table and vertically hanged at the top wall of the wind tunnel as a cantilever beam (figure 8.1a). The elastic plate was fixed near the entrance of the wind tunnel, at 0.7 m from the inlet, where the boundary layer effects are negligible. The plate has a height $L$ = 240 mm, width $b$ = 60 mm, thickness $c$ = 0.5 mm, Young's modulus $E$ = 2.4 GPa, and density $\rho_m = 1180$ kg m$^{-3}$. The unsteady dynamics of the plate was characterized at 35 incoming velocities $U_0 \in [3.2, 11.1]$ m s$^{-1}$ every $\Delta U_0 \approx 0.23$ m s$^{-1}$, resulting in Reynolds numbers $Re = U_0 b/\nu \in [1.3, 4.4] \times 10^4$, or Cauchy numbers $Ca = \rho_f b L^3 U_0^2/(EI) \in [8, 83]$ [71]; here $I = bc^3/12$. For each velocity, the plate was placed at an inclination angle $\alpha = 0^o, 30^o$ and $45^o$ controlled by the rotary table with an accuracy of 100 arcsec. The angle $\alpha = 0^o$ refers to the plate facing the incoming flow (See figure 8.1b).

The instantaneous flow-induced force acting on the elastic plate was measured at a frequency of 1kHz for periods of 30 s using an high-resolution ATI Gamma load cell connected at the plate base, which was mounted outside of the test section [119, 114]. Dynamics of the plate tips were tracked using a 3D particle tracking velocimetry (PTV) system at a frequency of 300 Hz for periods of 30 s with camera views at the bottom and one side of the plate to track instantaneous 3D motions (figure 8.1a). The plate was illuminated with two Stanley Lithium Ion Halogen Spotlights and captured within an investigation volume of 240 mm × 160 mm × 160 mm using two 4 MP Mikrotron EoSens 4CXP MC4082 high-speed cameras. Nikon AF Micro-Nikkor 50 mm lens with a focal ratio $f/2.8$ were used to maximize the focus on the selected investigation volume. The centroid of illuminated fidicual points were detected at sub-pixel level and tracked using the Hungarian algorithm and linked by performing a three-frame gap closing to obtain linked trajectories. A robust calibration is required to minimize the position error of detected points. The investigation volume was calibrated using a 200 mm × 200 mm planar target containing 342 fiducial points placed 10 mm apart. The rms of the recognized calibration points was $\approx 2 \times 10^{-4} L$. The calibration process was performed for each case by carefully placing the calibration target in the vicinity of the plate oscillation center to account for the change in pixel/mm ratio along the camera view. To further reduce the error of velocity estimation, the PTV data were smoothed by using the least-squares spline method. To minimize any initial transient effect, the force fluctuations and tip motions were sampled after the steady state was reached (waiting time of at least 60 s).

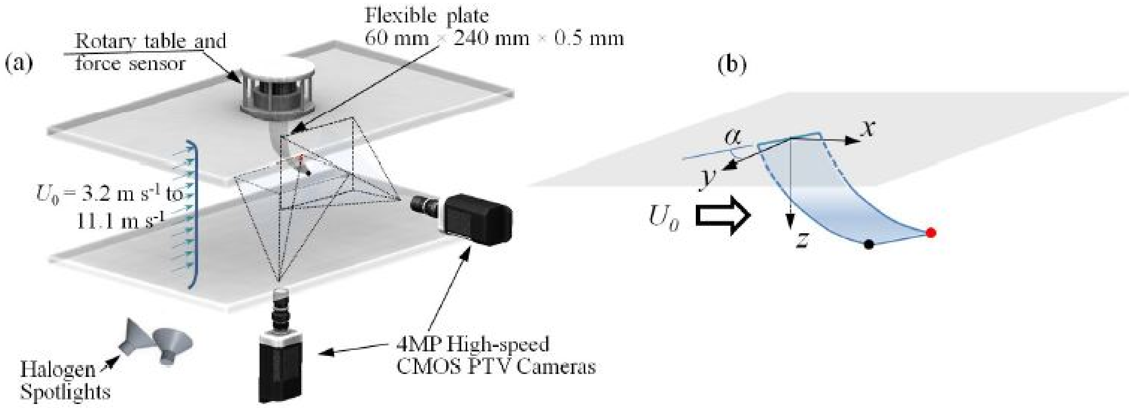

Figure 8.1: (a) Schematic of the experimental setup illustrating the force sensor, rotary table and PTV system. (b) Basic definitions; the origin of the coordinate system is fixed at the center of the plate base, the black and red fiducial points denote the tips used in other figures, and $\alpha$ is the inclination angle at the plate base respect to the mean flow $U_0$.

## 8.2 Results

### 8.2.1 Aerodynamic force fluctuations and plate dynamics

Characterization of the plate motions and fluctuations of the aerodynamic force across $Ca$ and $\alpha$ revealed distinctive patterns. Bulk quantification of the plate dynamics can be obtained with the intensity of the force fluctuations. In particular, distributions of the component normal to the base of the plate $I_N$ ($= \frac{2\sigma_N}{\rho_f U_0^2 bL}$, where $\sigma_N$ is the standard deviation of the force) as a function of $Ca$ are illustrated in figure 8.2(a). It shows negligible differences between plate inclinations for sufficiently low $Ca$, and abrupt increase of the force fluctuations past a critical $Ca = Ca_c$ threshold that depended on the inclination angle. Such critical condition occurred at $Ca_c = 34$ and 22 for $\alpha = 30^o$ and $45^o$ cases but it was absent at $\alpha = 0^o$. To highlight the sharp change on the force fluctuations, figure 8.2(b-c) illustrates a sample time series of the normal force at the plate base $F_N$ for the case $\alpha = 45^o$ right before ($Ca = 20.5$)

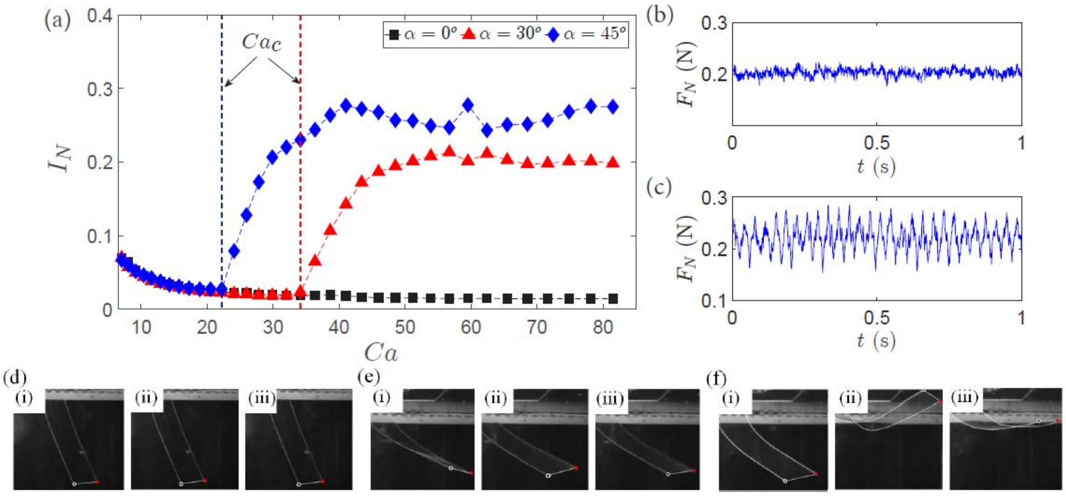

Figure 8.2: (a) Intensity of the normal force fluctuations ($I_N$) across various $Ca$ and $\alpha$. (b-c) Sample time series of the normal force $F_N$ at the plate base right below ($Ca = 20.5$ for (b)) and above ($Ca = 24$ for (c)) $Ca_c$ at $\alpha = 45^o$. (d-f) Snapshots of plate dynamics at $\alpha = 45^o$ and various $Ca$: (d) $Ca = 9$; (e) $Ca = 32$, and (f) $Ca = 68$. Here (i), (ii) and (iii) are instants highlighting dominant modes of tip motions.

and after ($Ca = 24$) $Ca_c$. Despite the similar averaged values, distinctive, high-amplitude periodic oscillations occurred right within $Ca > Ca_c$ implying the onset of a different oscillation mode.

Instantaneous snapshots shown in figure 8.2(d-f) provide a basic linkage of the force fluctuation and distinctive dynamics of the plate motions for the particular case with $\alpha = 45^o$. At $Ca < Ca_c$ (figure 8.2d), the plate exhibited small-amplitude fluttering around the bending equilibrium. The increase of $Ca$ over $Ca_c$ (figure 8.2e) resulted in twisting oscillations around a relatively larger bending. At sufficiently high $Ca$, the plate tips exhibited comparatively large-scale orbital motions; this condition happened at $Ca \leq 40$ ($\alpha$=45$^o$). There, the tip was dominated by counter-clockwise orbits coupled with twisting oscillations, as illustrated in figure 8.2(f).

The trajectories of the tip motions for various $Ca$ and $\alpha$ illustrate the dominant

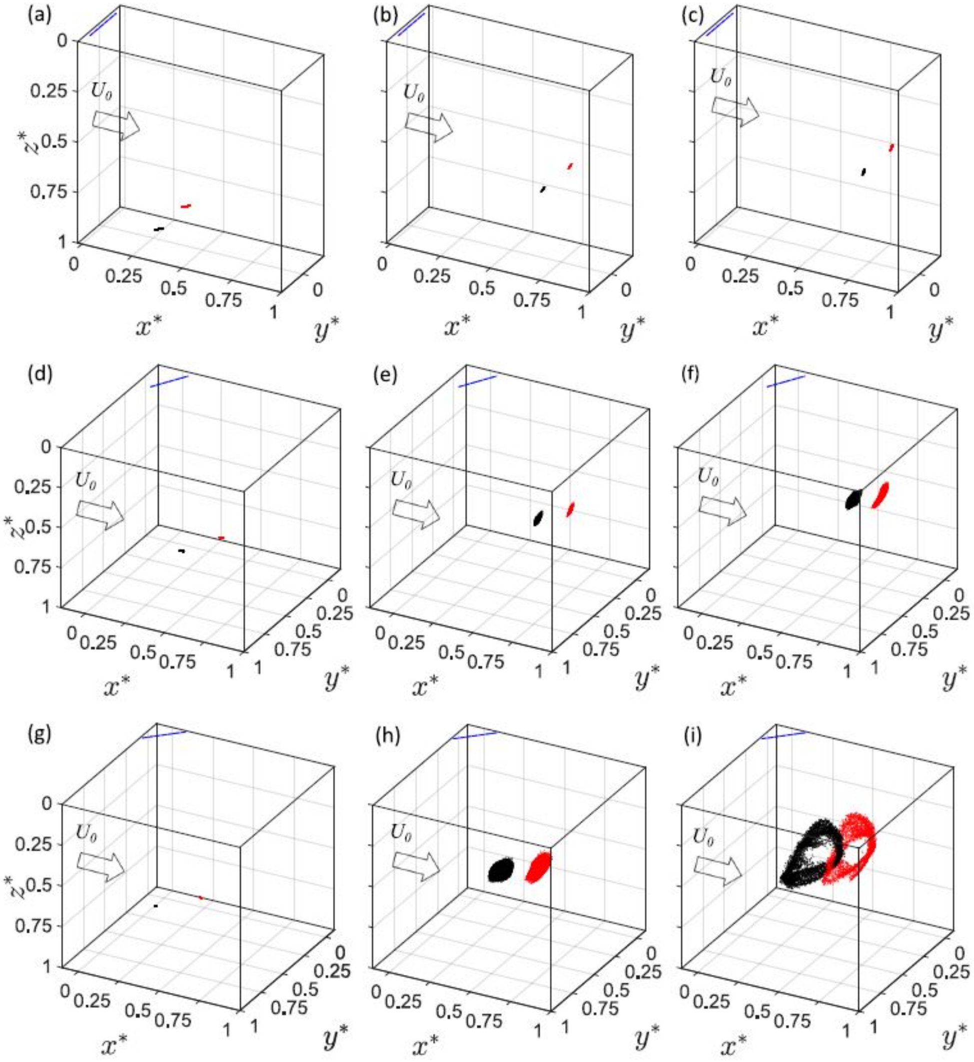

Figure 8.3: Trajectories of the tips for various $\alpha$ and $Ca$. (a-c) $\alpha = 0^o$ with $Ca = 8$, 42 and 68; (d-f) same as (a-c) with $\alpha = 30^o$; (g-i) same as (a-c) with $\alpha = 45^o$. $x^* = x/L$, $y^* = y/L$ and $z^* = z/L$ denote the normalized tip locations. The blue lines represent the location of the plate base.

modes of oscillations. Indeed, figure 8.3a-c shows minor fluttering corresponding to low $I_N$ around the bending equilibrium for $\alpha = 0^o$. Such mode is also observed under $\alpha = 30^o$ and $45^o$ within $Ca < Ca_c$ (figure 8.3d,g). At $Ca_c$, the plate experienced onset of twisting oscillations. This resulted in stronger tip motions and, consequently, increased $I_N$ (figure 8.3e,f,h,i). As expected, the intensity of tip oscillations increased with $Ca$ and $\alpha$. Dominant 3D orbital motions occurred at a specific threshold, which is the case in figure 8.3(i) at $Ca = 68$ and $\alpha = 45^o$. It is worth noting that such 3D dynamics led to significant deviations of the plate tips from the bending equilibrium; in this case the orbits from each tip overlapped.

Specific insight on the distinctive modes of oscillations is obtained by examining the representative trajectories and spectra of the tip velocity. In the fluttering-like mode, the bending deformation dominates the reconfiguration of the elastic plate where the tip is nearly parallel to the base. As noted in figure 8.4(a), the streamwise velocity spectrum $\Phi^*$ of one of the tip edges evidences the modulation of the first- and second-order natural frequencies of the bending; these are given by $f_{b,r} = \frac{j_r}{L^2}\sqrt{\frac{EI}{\rho_m bc}}$ where $j_1 = 0.56$ and $j_2 = 3.51$. As reported in previous works [67, 65, 33, 111], for a thin flat plate inclined with respect to the mean flow, the aerodynamic load produces a torque $M$ that tends to twist the frontal surface perpendicular to the freestream flow. Its magnitude is given by:

$$M = \frac{1}{2} C_M(\alpha) \rho_f U_e^2 A b \tag{8.1}$$

where $C_M(\alpha)$ is the moment coefficient, $U_e$ is the effective wind speed and $A$ represents a characteristic area of the structure. An increase of the velocity results in an increment of the torque and the likelihood of tip twisting, which is controlled by the body stiffness. Such modulation, however, is continuously disturbed by the wake fluctuations resulting in twisting oscillations (figure 8.4b). The height difference between the tips ($\Delta z_t^*$) leads to the tip not parallel to the base. In such cases, the tip velocity was substantially higher than the fluttering-like mode and exhibited semi-periodic variations. This is reflected by the dominating frequency component $f_t$ in the spectral domain. It is worth noting that $f_t$ remains nearly constant within all the twisting configurations, indicating that it is determined only by the characteristics of the structure.

Unlike the abrupt occurrence of twisting mode from fluttering with $Ca$, the transition from twisting to 3D orbits is comparatively a gradual process, where $I_N$ remains approximately constant. An example of this case is shown in the sample trajectories of figure 8.4(c) at $Ca = 42$ and $\alpha = 45^o$ characterized by the twisted 3D orbital motions. Indeed, the associated tip velocity spectrum reveals both dominant effects of the twisting mode ($f_t$) and the frequency of the orbital motion $f_r$. The distinctive mode of the 3D orbits is a result of the coupling between plate twisting and bending as a three-stage process illustrated in figure 8.4(d) and figure 8.5 with instantaneous tip heights. The flow-induced torque at sufficiently high $Ca$ and $\alpha$ leads to distinctive twisting of the plate near the tip such that the local projected area to the incoming flow increases (stage 1); this induces an abrupt increase of the aerodynamic load in the vicinity of the tip and substantial structure bending as highlighted by the decrease of $z^*$ of both tips (stage 2). As depicted in figure 5.7(f,ii), relatively high load can substantially deform the elastic plate; local bending angle of the plate near the tip relative to the vertical axis can reach or even be larger than $90^o$. In this scenario (stage 3), the tip aerodynamic load drops significantly due to the reduced projected area. The structure restoring force governs the motion of the plate, pushing the tip back to the posture at stage 1, which completes an orbital cycle. Similar

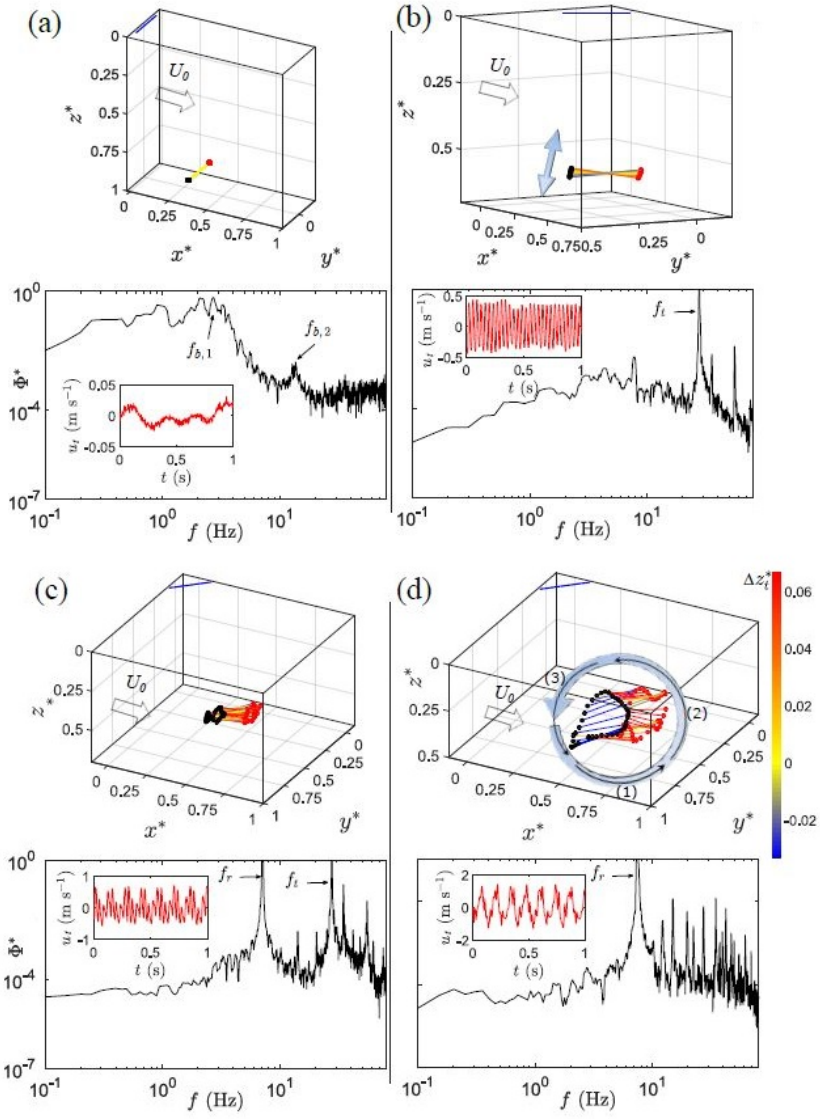

Figure 8.4: Sampled tip trajectories and normalized streamwise velocity spectra $\Phi^* = \Phi/max\{\Phi\}$ of a tip under (a) $Ca = 8$ and $\alpha = 0^o$; (b) $Ca = 42$ and $\alpha = 30^o$; (c) $Ca = 42$ and $\alpha = 45^o$; (d) $Ca = 68$ and $\alpha = 45^o$. The colorbar indicates the normalized height difference between the tips ($\Delta z_t^*$). The two-way, blue arrow in (b) denotes the twisting oscillations, whereas the counter-clockwise arrow in (d) indicates the 3D orbital motion of the tips composed of 3 stages. The subplots show the (red) tip streamwise velocity $u_t$.

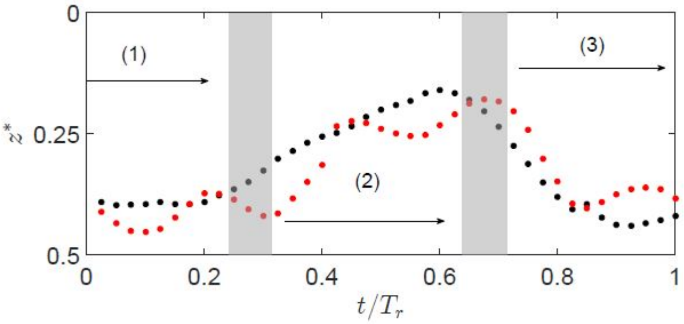

Figure 8.5: Instantaneous tip heights $z^* = z/L$ during one representative orbital cycle under $Ca = 68$ and $\alpha = 45^o$; here $T_r = 1/f_r$ is the period of orbital motion. The black and red points denote each tip.

to the twisting mode, $f_r$ is independent of $Ca$ within the inspected configurations, despite the significant variation of the intensity of the orbital motions.

### 8.2.2 Theoretical estimation of the critical $Ca$ or $Ca_c$

An uncovered key quantity is the threshold $Ca_c$ that defines the condition of abrupt increase of force fluctuations leading to substantial unsteady loading. The aerodynamic load of an elastic structure undergoing simultaneous bending and twisting involves a number of physical processes; to tackle this problem quantitatively, we consider that the plate experiences minor deformation in a portion close to the tip. This assumption is well supported by the tracking of plate postures under $Ca < Ca_c$ (figure 5.7d) and previous studies [30]. Also, the plate dynamics shows that the plate remain nearly parallel to its base before the occurrence of the twisting mode. Hence, as a first-order approximation, we focus our analysis on the plate tip region with a constant local bending angle ($\theta$) and inclination angle $\alpha$ relative to the freestream flow at equilibrium, as illustrated in figure 7.7(a). There, the governing equation of the twisting dynamics of the plate can be characterized by:

$$I_w \frac{d^2\hat{\alpha}}{dt^2} + c_w \frac{d\hat{\alpha}}{dt} + k_w \hat{\alpha} = -\frac{1}{2} C_M|_{\hat{\alpha}_e} \rho_f U_e^2 A b \tag{8.2}$$

where $\hat{\alpha}$ is the modified inclination angle due to plate bending, $I_w, c_w$ and $k_w$ represent the polar moment of inertia, damping coefficient and torsional stiffness corresponding to the section under inspection, and $\hat{\alpha}_e$ is the effective inclination angle modulated by the plate angular velocity. Here, the positive $M$ is defined to induce a decrease of $\hat{\alpha}$. For an inclined bended plate, the effective wind speed $U_e$ is taken as the velocity component normal to the plate span (figure 7.7a), whereas the modified inclination angle at the equilibrium ($\hat{\alpha}_s$) is defined between $U_e$ and the normal vector $\vec{n}$ of the plate surface at the equilibrium bending position, as follows:

$$\begin{aligned} U_e &= U_0 \sqrt{1 - \cos^2\alpha \sin^2\theta} \\ \sin\hat{\alpha}_s &= \frac{\sin\alpha}{\sqrt{1 - \cos^2\alpha \sin^2\theta}} \end{aligned} \tag{8.3}$$

The effective inclination angle $\hat{\alpha}_e$ is influenced by the instantaneous angular velocity of the plate. Following the linear quasi-steady analysis characterizing the torsional instability [132], we consider an instant where the plate is in a given $\hat{\alpha}$ with an instantaneous angular velocity $\frac{d\hat{\alpha}}{dt}$ (figure 7.7b). To represent the varying relative flow velocity along the width, we define a reference radius $b\xi$ such that the plate velocity is considered as $v = \frac{d\hat{\alpha}}{dt} b\xi$ of the cross section [133, 134] and assumed to undergo minor variations within the investigated inclination angles [96]. This leads

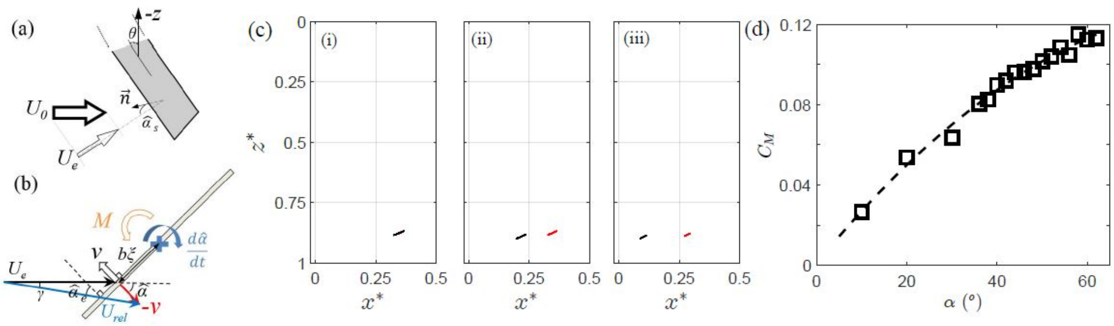

Figure 8.6: (a) Schematic illustrating parameters near plate tip region with bending angle $\theta$. (b) Schematic of the cross section of the plate undergoing twisting motion under the influence of instantaneous angular velocity. The '+' symbol denotes the plate center. (c) Distribution of the plate tips projected in $x-z$ plane under $Ca = 8$ and (i) $\alpha = 0^o$; (ii) $\alpha = 30^o$; (iii) $\alpha = 45^o$. (d) Distribution of $C_M = 2M/(\rho_f U_0^2 b^2 L)$ with $\alpha$ of a rigid plate with the same geometry.

to the relative wind velocity ($\vec{U}_{rel}$) and effective inclination angle as:

$$\begin{aligned} \vec{U}_{rel} &= \vec{U}_e - \vec{v} \\ \hat{\alpha}_e &= \hat{\alpha} - \gamma. \end{aligned} \tag{8.4}$$

For relatively small $\gamma$ (small plate velocity compared to $U_e$) and low-amplitude twisting around the equilibrium:

$$\begin{aligned} U_{rel} &\simeq U_e \\ \gamma &\simeq \frac{v}{U_e}\sin\hat{\alpha} \simeq \frac{v}{U_e}\sin\hat{\alpha}_s, \end{aligned} \tag{8.5}$$

and, therefore:

$$\hat{\alpha}_e = \hat{\alpha} - \frac{\xi b}{U_e}\frac{d\hat{\alpha}}{dt}\sin\hat{\alpha}_s \tag{8.6}$$

Then, using Taylor's expansion, the moment coefficient can be approximated as:

$$C_M|_{\hat{\alpha}_e} = C_M|_{\hat{\alpha}_s} + \frac{\partial C_M}{\partial \alpha}|_{\hat{\alpha}_s}(\hat{\alpha}_e - \hat{\alpha}_s) \tag{8.7}$$

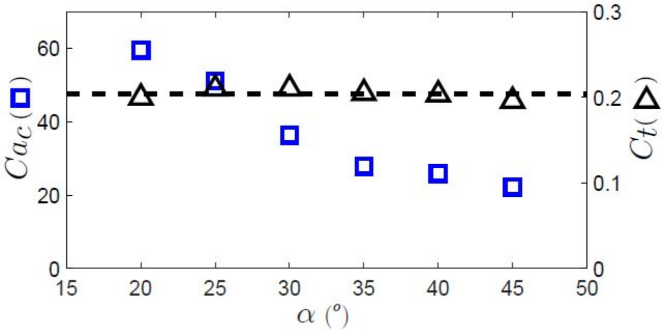

Figure 8.7: $Ca_c$ and dimensionless quantity $C_t$ (Eq. 8.9) characterizing the threshold of twisting motions; the dashed line marks the averaged value of $C_t$ across $\alpha$.

The condition leading to sudden increase of twisting motion denotes the loss of the system stability, which occurs when damping vanishes, i.e., the terms in $d\hat{\alpha}/dt$ (combining Eqs. 8.2, 8.6 and 8.7) is zero:

$$\frac{\partial C_M}{\partial \alpha}|_{\hat{\alpha}_s} U_e \sin \hat{\alpha}_s = \frac{2c_w}{\xi b^2 \rho_f A} = C \tag{8.8}$$

where $C$ is a constant. Key for evaluating the model is the estimation of the plate tip bending angle $\theta$ and, thus, $\hat{\alpha}_s$ at each $Ca_c$. Despite the variation of $\alpha$, the equilibrium tip height resulted very close at a given $Ca$ within $Ca < Ca_c$ (see example in figure 8.6c) indicating similar plate bending; therefore, $\theta$ can be inferred from the case with $\alpha = 0$ at each $Ca_c$ directly from the PTV measurements. To determine $\frac{\partial C_M}{\partial \alpha}|_{\hat{\alpha}_s}$, the aerodynamic torque of a rigid metallic plate with same geometry of the elastic counterpart was measured across various $\alpha$ as shown in figure 8.6(d), where the distribution of $C_M$ follows a power-law function with $\alpha$ (see dashed line with power 1/2). Noting that $Ca \propto U_0^2$ for a given structure and combing Eqs. 3.3 and 8.8, we can then define a dimensionless quantity $C_t$ characterizing the threshold of $Ca_c$:

$$C_t = \frac{\partial C_M}{\partial \alpha}|_{\hat{\alpha}_s} \sqrt{Ca_c} \sin \alpha \tag{8.9}$$

Additional experiments were conducted to test equation 8.9, with the plate under various $\alpha$. As shown in figure 8.7, $Ca_c$ decreased monotonically with $\alpha$; remarkably, $C_t \approx 0.2 \pm 0.005$ across all investigated $\alpha$. It should be noted that for flexible plates with different geometry and material, the parameters at right hand side of equation 8.8 may vary and lead to different $C_t$; however, the critical $Ca_c$ should still follow equation 8.9 for a given structure. That is, the abrupt force fluctuations are triggered by instability mechanisms in an inclined, bended plate relative to the mean flow.

## 8.3 Conclusions

Overall, we have shown the distinctive force fluctuations and dynamics of inclined, flexible plates under various flows. Our experiments revealed a sharp increase of the unsteady force, where the plate tip motions shifted from small-amplitude fluttering to twisting oscillations past a critical $Ca$. Further increase of the incoming velocity or $Ca$ under sufficient $\alpha$ led to distinctive 3D orbital dynamics induced by the coupled twisting and bending deformations. The agreement between our theoretical arguments and experiments demonstrates the dominating role of the dynamic instability in triggering twisting oscillations. These findings provide novel insights for examining the reconfiguration and, particularly, the large-amplitude 3D orbital motions of elastic structures under complex flow fields. Theoretical inspection of the onset of abrupt force fluctuations may be used to determine conditions for structure fatigue and design various engineering structures and processes exposed to flows.

# CHAPTER 9

# REMARKS AND FUTURE DIRECTIONS

## 9.1 Conclusions

Turbulence-structure interaction is a ubiquitous phenomenon of high relevance in engineering systems. During the past decades, substantial research has focused on characterizing the dynamics of structures under a variety of flows; however, the quantitative description of the non-linear, multiscale interaction between structure dynamics and turbulence remains as an outstanding open problem in science and engineering. Uncovering dominant mechanisms modulating the dynamics of flow and structures would allow to significantly improve the design, reliability and life span of a wide range of systems ranging from deep-sea pipelines to underwater vehicles and wind farms, as well as environmental and industrial processes such as mixing and heat transfer, among others.

My Ph.D work focused on three distinct problems: 1) turbulence-structure feedback of 2D and 3D bodies; 2) active and passive flow control strategies for complex flows; 3) flow-induced dynamics of wall-mounted flexible structures. Using theory and state-of-the-art flow diagnostic tools including PIV, PTV, hotwire and telemetry, my research provided new formulations that quantitatively describe the underlying role of turbulence on the unsteady forces and dynamics of various structures. The impact of the finding are instrumental for many applications including energy harvesting, locomotion and control of dynamic loading, among others.

## 9.2 Future research directions

My long-term research goals are aimed at unraveling the dominant mechanisms modulating the turbulence-structure feedback in aero- and hydrodynamics applications. Special topics of interest include the following:

- Design of energy efficient propulsion of underwater vehicles. Optimized designs of underwater vehicles are possible by taking advantage of the distinctive fluid-structure feedback in a given environment. I plan to i) explore passive/active controlling mechanism for underwater vehicles to improve the maneuverability, ii) investigate optimum designs of bio-inspired concepts for achieving efficient propulsion, and iii) develop advanced feedback loops to efficiently handle flow perturbations
- Uncover structure dynamics under complex flows. The dynamics of elastic structures are ubiquitous in nature and engineering. My research will explore the oscillation and unsteady force of engineering structures under complex flow fields using theory and laboratory measurements taking into account the influence of turbulence intensity, integral length scale, and local flow direction. I will focus on general frameworks to quantify extend the life span of structures.
- Explore challenges in offshore wind energy. The high non-linear dynamics dominant in offshore wind energy poses major challenges to the advancement of this technology. My future work will explore in detail the coupled interaction between waves and airflow on floating platforms. Using novel experiments with hybrid concepts and theory as well as collaboration with industry, I plan to significantly improve the design and operation of floating wind turbines.

# REFERENCES

[1] Q. Zhu, “Energy harvesting by a purely passive flapping foil from shear flows,” *J Fluid Struct*, vol. 34, pp. 157–169, 2012.

[2] K. Hirata, K. Shimizu, K. Fukuhara, K. Yamauchi, D. Kawaguchi, and J. Funaki, “Aerodynamic characteristics of a tumbling plate under free flight,” *J Fluid Sci Tech, Japan*, vol. 4(1), pp. 168–187, 2009.

[3] D. I. Greenwell, “Geometry effects on autorotation of rectangular prisms,” *J Wind Eng Ind Aerodyn.*, vol. 132, pp. 92–100, 2014.

[4] L. Cicolani, C. Ivler, C. Ott, R. Raz, and A. Rosen, “Rotational stabilization of cargo container slung loads,” *J Am Helicopter Soc*, vol. 60, no. 4, pp. 1–13, 2015.

[5] M. Luhar and H. M. Nepf, “Flow-induced reconfiguration of buoyant and flexible aquatic vegetation,” *Limnol Oceanogr*, vol. 56, no. 6, pp. 2003–2017, 2011.

[6] K. Sand-Jensen, “Drag and reconfiguration of freshwater macrophytes,” *Freshwater Biol*, vol. 48, no. 2, pp. 271–283, 2003.

[7] T. Tamura and T. Miyagi, “The effect of turbulence on aerodynamic forces on a square cylinder with various corner shapes,” *J Wind Eng Ind Aerodyn.*, vol. 83, no. 1, pp. 135–145, 1999.

[8] H. Noda and A. Nakayama, “Free-stream turbulence effects on the instantaneous pressure and forces on cylinders of rectangular cross section,” *Exp Fluids*, vol. 34, no. 3, pp. 332–344, 2003.

[9] S. Pastò, “Vortex-induced vibrations of a circular cylinder in laminar and turbulent flows,” *J Fluid Struct*, vol. 24, no. 7, pp. 977–993, 2008.

[10] R. Govardhan and C. H. K. Williamson, “Modes of vortex formation and frequency response of a freely vibrating cylinder,” *J Fluid Mech*, vol. 420, pp. 85–130, 2000.

[11] L. P. Chamorro, M. Guala, R. E. A. Arndt, and F. Sotiropoulos, "On the evolution of turbulent scales in the wake of a wind turbine model," *J Turbul*, vol. 13, pp. 1–13, 2012.

[12] R. Gardon and J. C. Akfirat, "The role of turbulence in determining the heat-transfer characteristics of impinging jets," *Int J Heat Mass Tran*, vol. 8, no. 10, pp. 1261–1272, 1965.

[13] B. E. Lee, "The effect of turbulence on the surface pressure field of a square prism," *J Fluid Mech*, vol. 69, no. 2, pp. 263–282, 1975.

[14] M. Naimul Haque, H. Katsuchi, H. Yamada, and M. Nishio, "Investigation of flow fields around rectangular cylinder under turbulent flow by les," *Eng Appl Comp Fluid*, vol. 8, no. 3, pp. 396–406, 2014.

[15] M. S. Fonseca and J. S. Fisher, "A comparison of canopy friction and sediment movement between four species of seagrass with reference to their ecology and restoration," *Mar Eco Prog Ser*, vol. 29, no. 1, 1986.

[16] S. Alben, M. Shelley, and J. Zhang, "Drag reduction through self-similar bending of a flexible body," *Nature*, vol. 420, no. 6915, p. 479, 2002.

[17] S. Alben, M. Shelley, and J. Zhang, "How flexibility induces streamlining in a two-dimensional flow," *Phys Fluids*, vol. 16, no. 5, pp. 1694–1713, 2004.

[18] F. Gosselin, E. De Langre, and B. A. Machado-Almeida, "Drag reduction of flexible plates by reconfiguration," *J Fluid Mech*, vol. 650, pp. 319–341, 2010.

[19] C. Py, E. De Langre, and B. Moulia, "A frequency lock-in mechanism in the interaction between wind and crop canopies," *J Fluid Mech*, vol. 568, pp. 425–449, 2006.

[20] T. Sarpkaya, "A critical review of the intrinsic nature of vortex-induced vibrations," *J Fluid Struct*, vol. 19, no. 4, pp. 389–447, 2004.

[21] C. H. K. Williamson and R. Govardhan, "Vortex-induced vibrations," *Ann Rev Fluid Mech*, vol. 36(1), pp. 413–455, 2004.

[22] M. Zhao, "Flow-induced vibrations of square and rectangular cylinders at low reynolds number," *Fluid Dyn Res*, vol. 47, no. 2, p. 025502, 2015.

[23] A. Nemes, J. Zhao, D. L. Jacono, and J. Sheridan, "The interaction between flow-induced vibration mechanisms of a square cylinder with varying angles of attack," *J Fluid Mech*, vol. 710, pp. 102–130, 2012.

[24] J. Zhao, J. S. Leontini, D. L. Jacono, and J. Sheridan, “Fluid–structure interaction of a square cylinder at different angles of attack,” *J Fluid Mech*, vol. 747, pp. 688–721, 2014.

[25] T. Theodorsen, “General theory of aerodynamic instability and the mechanism of flutter,,” 1935, nASA technical report 496; (1935).

[26] T. Von Karman, “Airfoil theory for non-uniform motion.” *J Aeronaut Sci*, vol. 5(10), pp. 379–390, 1938.

[27] R. T. Jantzen, K. Taira, K. O. Granlund, and M. V. Ol, “Vortex dynamics around pitching plates,” *Phys Fluids*, vol. 26(5), p. 053606, 2014.

[28] Y. S. Baik, L. P. Bernal, K. Granlund, and M. V. Ol, “Unsteady force generation and vortex dynamics of pitching and plunging aerofoils,” *J Fluid Mech*, vol. 709, pp. 37–68, 2012.

[29] A. Nemes, J. Zhao, D. L. Jacono, and J. Sheridan, “The interaction between flow-induced vibration mechanisms of a square cylinder with varying angles of attack,” *J Fluid Mech*, vol. 710, pp. 102–130, 2012.

[30] L. Schouveiler, C. Eloy, and P. Le Gal, “Flow-induced vibrations of high mass ratio flexible filaments freely hanging in a flow,” *Phys Fluids*, vol. 17, no. 4, p. 047104, 2005.

[31] S. E. Spagnolie, L. Moret, M. J. Shelley, and J. Zhang, “Surprising behaviors in flapping locomotion with passive pitching,” *Phys Fluids*, vol. 22(4), p. 041903, 2010.

[32] R. Bourguet, G. E. Karniadakis, and M. S. Triantafyllou, “Vortex-induced vibrations of a long flexible cylinder in shear flow,” *J Fluid Mech*, vol. 677, pp. 342–382, 2011.

[33] K. Onoue, A. Song, B. Strom, and K. S. Breuer, “Large amplitude flow-induced oscillations and energy harvesting using a cyber-physical pitching plate,” *J Fluid Struct*, vol. 55, pp. 262–275, 2015.

[34] R. M. So and S. D. Savkar, “Buffeting forces on rigid circular cylinders in cross flows,” *J Fluid Mech*, vol. 105, pp. 397–425, 1981.

[35] L. Carassale, A. Freda, and M. Marrè-Brunenghi, “Effects of free-stream turbulence and corner shape on the galloping instability of square cylinders,” *J Wind Eng Ind Aerod*, vol. 123, pp. 274–280, 2013.

[36] R. M. So, X. Q. Wang, W. C. Xie, and J. Zhu, "Free-stream turbulence effects on vortex-induced vibration and flow-induced force of an elastic cylinder," *J Fluid Struct*, vol. 24(4), pp. 481–495, 2008.

[37] S. J. Daniels, I. P. Castro, and Z. T. Xie, "Numerical analysis of freestream turbulence effects on the vortex-induced vibrations of a rectangular cylinder," *J Wind Eng Ind Aerod*, vol. 153, pp. 13–25, 2016.

[38] H. D. Akaydin, N. Elvin, and Y. Andreopoulos, "Energy harvesting from highly unsteady fluid flows using piezoelectric materials," *J Intel Mat Syst Str*, vol. 21(13), pp. 1263–1278, 2010.

[39] J. D. Hobeck and D. J. Inman, "Artificial piezoelectric grass for energy harvesting from turbulence-induced vibration," *Smart Mater Struct*, vol. 21(10), p. 105024, 2012.

[40] J. D. Hobeck and D. J. Inman, "A distributed parameter electromechanical and statistical model for energy harvesting from turbulence-induced vibration," *Smart Mater Struct*, vol. 23(11), p. 115003, 2014.

[41] M. M. A. Bhutta, N. Hayat, A. U. Farooq, Z. Ali, S. R. Jamil, and Z. Hussain, "Vertical axis wind turbine–a review of various configurations and design techniques," *Renew Sust Energ Rev*, vol. 16(4), pp. 1926–1939, 2012.

[42] M. Kinzel, D. B. Araya, and J. O. Dabiri, "Turbulence in vertical axis wind turbine canopies," vol. 27, p. 115102, 2015.

[43] E. H. Smith, "Autorotating wings: an experimental investigation," *J Fluid Mech*, vol. 50.03, pp. 513–534, 1971.

[44] J. D. Iversen, "Autorotating flat-plate wings: the effect of the moment of inertia, geometry and reynolds number," *J Fluid Mech*, vol. 92(02), pp. 327–348, 1979.

[45] C. Luo, B. Shen, and B. Ooi, "Strategies to smooth wind power fluctuations of wind turbine generator," *IEEE Transactions on Energy Conversion*, vol. 22(2), pp. 341–349, 2007.

[46] J. Apt, "The spectrum of power from wind turbines," *J of Power Sources*, vol. 169, pp. 369–374, 2007.

[47] L. P. Chamorro, S. J. Lee, D. Olsen, C. Milliren, J. Marr, R. E. A. Arndt, and F. Sotiropoulos, "Turbulence effects on a full-scale 2.5 mw horizontal-axis wind turbine under neutrally stratified conditions," *Wind Energy*, vol. 18(2), pp. 339–349, 2015.

[48] N. Tobin, H. Zhu, and L. P. Chamorro, “Spectral behaviour of the turbulence-driven power fluctuations of wind turbines,” *J Turbul*, vol. 16(9), pp. 832–846, 2015.

[49] P. Milan, M. Wächter, and J. Peinke, “Turbulent character of wind energy,” *Phys Rev Lett*, vol. 110(13), p. 138701, 2013.

[50] R. Fail, J. A. Lawford, and R. C. W. Eyre, “Low speed experiments on the wake characteristics of flat plates normal to an airstream.” 1957, aeronautical research council, reports and memoranda no. 3120.

[51] J. C. Manwaring, G. A. Conway, and L. C. Garrett, “Epidemiology and prevention of helicopter external load accidents,” *J Safety Res*, vol. 29, no. 2, pp. 107–121, 1998.

[52] R. Raz, A. Rosen, L. S. Cicolani, and J. Lusardi, “Using wind tunnel tests for slung-load clearance, part 1: The conex cargo container,” *J Am Helicopter Soc*, vol. 59, no. 4, pp. 1–12, 2014.

[53] R. Raz, A. Rosen, A. Carmeli, J. Lusardi, L. S. Cicolani, and D. Robinson, “Wind tunnel and flight evaluation of stability and passive stabilization of cargo container slung load,” *American Helicopter Society 64th Annual Forum, Montreal, Canada*, 2008.

[54] D. T. Prosser and M. J. Smith, “Numerical characterization of three-dimensional bluff body shear layer behaviour,” *J Fluid Mech*, vol. 799, pp. 1–26, 2016.

[55] D. T. Prosser and M. J. Smith, “A physics-based, reduced-order aerodynamics model for bluff bodies in unsteady, arbitrary motion,” *J Am Helicopter Soc*, vol. 60, no. 3, pp. 1–15, 2015.

[56] K. Liu, J. Deng, and M. Mei, “Experimental study on the confined flow over a circular cylinder with a splitter plate,” *Flow Meas Instrum*, vol. 51, pp. 95–104, 2016.

[57] X. Wu, F. Ge, and Y. Hong, “A review of recent studies on vortex-induced vibrations of long slender cylinders,” *J Fluid Struct*, vol. 28, pp. 292–308, 2012.

[58] M. C. Thompson, A. Radi, A. Rao, J. Sheridan, and K. Hourigan, “Low-reynolds-number wakes of elliptical cylinders: from the circular cylinder to the normal flat plate,” *J Fluid Mech*, vol. 751, pp. 570–600, 2014.

[59] A. Roshko, “On the wake and drag of bluff bodies,” *J. Aeronaut. Sci.*, vol. 22, pp. 124–132, 1955.

[60] C. J. Apelt and G. S. West, "The effects of wake splitter plates on bluff-body flow in the range $10^4 <$ R$< 5 \times 10^4$. part 2," *J Fluid Mech*, vol. 71, no. 01, pp. 145–160, 1975.

[61] J. Y. Hwang and K. S. Yang, "Drag reduction on a circular cylinder using dual detached splitter plates," *J Wind Eng Ind Aerodyn.*, vol. 95, no. 7, pp. 551–564, 2007.

[62] M. S. Mat Ali, C. J. Doolan, and V. Wheatley, "Low reynolds number flow over a square cylinder with a splitter plate," *Phys Fluids*, vol. 23, no. 3, p. 033602, 2011.

[63] A. R. Ogunremi and D. Sumner, "The influence of a splitter plate on the mean wake of a surface-mounted finite-height circular cylinder," 2013, proceedings of the 24th CANCAM, Saskatoon, Saskatchewan, Canada, June 2-6, 2013.

[64] M. T. Nair and T. K. Sengupta, "Unsteady flow past elliptic cylinders," *J Fluid Struct*, vol. 11, no. 6, pp. 555–595, 1997.

[65] V. J. Modi, E. Wiland, A. K. Dikshit, and T. Yokomizo, "On the fluid dynamics of elliptic cylinders," in *The Second International Offshore and Polar Engineering Conference*. International Society of Offshore and Polar Engineers, 1992.

[66] U. Lācis, N. Brosse, F. Ingremeau, A. Mazzino, F. Lundell, H. Kellay, and S. Bagheri, "Passive appendages generate drift through symmetry breaking," *Nat Commun*, vol. 5, 2014.

[67] A. Fage and F. C. Johansen, "On the flow of air behind an inclined flat plate of infinite span," vol. 116(773), pp. 170–197, 1927, proceedings of the Royal Society of London. Series A, Containing Papers of a Mathematical and Physical Character.

[68] A. Pelletier and T. J. Mueller, "Low reynolds number aerodynamics of low-aspect-ratio, thin/flat/cambered-plate wings," *J Aircraft*, vol. 37(5), pp. 825–832, 2000.

[69] X. Amandolese, S. Michelin, and M. Choquel, "Low speed flutter and limit cycle oscillations of a two-degree-of-freedom flat plate in a wind tunnel," *J Fluid Struct*, vol. 43, pp. 244–255, 2013.

[70] F. Gu, J. S. Wang, X. Q. Qiao, and Z. Huang, "Pressure distribution, fluctuating forces and vortex shedding behavior of circular cylinder with rotatable splitter plates," *J Fluid Struct*, vol. 28, pp. 263–278, 2012.

[71] L. Lu, X. L. Guo, G. Q. Tang, M. M. Liu, C. Q. Chen, and Z. H. Xie, "Numerical investigation of flow-induced rotary oscillation of circular cylinder with rigid splitter plate," *Phys Fluids*, vol. 28, no. 9, p. 093604, 2016.

[72] G. R. Assi, P. W. Bearman, and N. Kitney, "Low drag solutions for suppressing vortex-induced vibration of circular cylinders," *J Fluid Struct*, vol. 25, no. 4, pp. 666–675, 2009.

[73] S. Bagheri, A. Mazzino, and A. Bottaro, "Spontaneous symmetry breaking of a hinged flapping filament generates lift," *Phys Rev Lett*, vol. 109, no. 15, p. 154502, 2012.

[74] U. Lācis, S. Olivieri, A. Mazzino, and S. Bagheri, "Passive control of a falling sphere by elliptic-shaped appendages," *Phys Rev Fluids*, vol. 2, no. 3, p. 033901, 2017.

[75] A. Andersen, T. Bohr, T. Schnipper, and J. H. Walther, "Wake structure and thrust generation of a flapping foil in two-dimensional flow," *J Fluid Mech*, vol. 812, 2017.

[76] P. T. Tokumaru and P. E. Dimotakis, "Rotary oscillation control of a cylinder wake," *J Fluid Mech*, vol. 224, pp. 77–90, 1991.

[77] S. Choi, H. Choi, and S. Kang, "Characteristics of flow over a rotationally oscillating cylinder at low reynolds number," vol. 14, no. 8, pp. 2767–2777, 2002.

[78] O. Cetiner and D. Rockwell, "Streamwise oscillations of a cylinder in steady current. part 2. free-surface effects on vortex formation and loading," *J Fluid Mech*, vol. 427, pp. 29–59, 2001.

[79] Y. Delaunay and L. Kaiktsis, "Control of circular cylinder wakes using base mass transpiration," vol. 13, no. 11, pp. 3285–3302, 2001.

[80] M. Amitay, B. Smith, and A. Glezer, "Aerodynamic flow control using synthetic jet technology," in *36th AIAA Aerospace Sciences Meeting and Exhibit*, 1998, p. 208.

[81] D. G. Bohl and M. M. Koochesfahani, "Mtv measurements of the vortical field in the wake of an airfoil oscillating at high reduced frequency," *J Fluid Mech*, vol. 620, pp. 63–88, 2009.

[82] A. W. Mackowski and C. H. K. Williamson, "Direct measurement of thrust and efficiency of an airfoil undergoing pure pitching," *J Fluid Mech*, vol. 765, pp. 524–543, 2015.

[83] T. Schnipper, A. Andersen, and T. Bohr, "Vortex wakes of a flapping foil," *J Fluid Mech*, vol. 633, pp. 411–423, 2009.

[84] H. Huang, H. Wei, and X.-Y. Lu, "Coupling performance of tandem flexible inverted flags in a uniform flow," *J Fluid Mech*, vol. 837, pp. 461–476, 2018.

[85] J. C. Mullarney and S. M. Henderson, "Wave-forced motion of submerged single-stem vegetation," *J Geophys Res-Oceans*, vol. 115, no. C12, 2010.

[86] M. Luhar and H. M. Nepf, "Wave-induced dynamics of flexible blades," *J Fluid Struct*, vol. 61, pp. 20–41, 2016.

[87] A. S. Thom, "Momentum absorption by vegetation," *Q J Roy Meteor Soc*, vol. 97, no. 414, pp. 414–428, 1971.

[88] Y. Brunet, J. J. Finnigan, and M. R. Raupach, "A wind tunnel study of air flow in waving wheat: single-point velocity statistics," *Boundary-Layer Meteorol.*, vol. 70, no. 1-2, pp. 95–132, 1994.

[89] M. D. Novak, J. S. Warland, A. L. Orchansky, R. Ketler, and S. Green, "Wind tunnel and field measurements of turbulent flow in forests. part i: uniformly thinned stands," *Boundary-Layer Meteorol.*, vol. 95, no. 3, pp. 457–495, 2000.

[90] S. Barsu, D. Doppler, J. J. S. Jerome, N. Rivière, and M. Lance, "Drag measurements in laterally confined 2d canopies: Reconfiguration and sheltering effect," vol. 28, no. 10, p. 107101, 2016.

[91] F. J. Huera-Huarte and P. W. Bearman, "Vortex and wake-induced vibrations of a tandem arrangement of two flexible circular cylinders with near wake interference," *J Fluid Struct*, vol. 27, no. 2, pp. 193–211, 2011.

[92] I. Borazjani and F. Sotiropoulos, "Vortex-induced vibrations of two cylinders in tandem arrangement in the proximity–wake interference region," *J Fluid Mech*, vol. 621, pp. 321–364, 2009.

[93] E. Wang, Q. Xiao, Q. Zhu, and A. Incecik, "The effect of spacing on the vortex-induced vibrations of two tandem flexible cylinders," vol. 29, no. 7, p. 077103, 2017.

[94] L. Ristroph and J. Zhang, "Anomalous hydrodynamic drafting of interacting flapping flags," *Phys. Rev. Lett.*, vol. 101, no. 19, p. 194502, 2008.

[95] S. Kim, W.-X. Huang, and H. J. Sung, "Constructive and destructive interaction modes between two tandem flexible flags in viscous flow," *J Fluid Mech*, vol. 661, pp. 511–521, 2010.

[96] L. Tadrist, K. Julio, M. Saudreau, and E. De Langre, “Leaf flutter by torsional galloping: experiments and model,” *J Fluid Struct*, vol. 56, pp. 1–10, 2015.

[97] K. M. Lam, “Phase-locked eduction of vortex shedding in flow past an inclined flat plate,” vol. 8, no. 5, pp. 1159–1168, 1996.

[98] K. M. Lam and M. Y. H. Leung, “Asymmetric vortex shedding flow past an inclined flat plate at high incidence,” *Eur J Mech B-Fluid*, vol. 24, pp. 33–48, 2005.

[99] S. Mirzaeisefat and A. C. Fernandes, “Stability analysis of the fluttering and autorotation of flow-induced rotation of a hinged flat plate,” *J Hydrodyn*, vol. 25(5), pp. 755–762, 2013.

[100] Y. Jin, S. Ji, B. Liu, and L. P. Chamorro, “On the role of thickness ratio and location of axis of rotation in the flat plate motions,” *J Fluid Struct*, vol. 64, pp. 127–137, 2016.

[101] Y. Jin, H. Liu, R. Aggarwal, A. Singh, and L. P. Chamorro, “Effects of freestream turbulence in a model wind turbine wake,” *Energies*, vol. 9, no. 10, p. 830, 2016.

[102] T. G. Zaki and M. Gad-El-Hak, “Numerical and experimental investigation of flow past a freely rotatable square cylinder,” *J Fluid Struct*, vol. 8(7), pp. 555–582, 1994.

[103] M. Tatsuno, T. Takayama, H. Amamoto, and K. Ishi-i, “On the stable posture of a triangular or a square cylinder about its central axis in a uniform flow,” *Fluid Dyn Res*, vol. 6, pp. 201–207, 1990.

[104] A. Khalak and C. H. K. Williamson, “Motions, forces and mode transitions in vortex-induced vibrations at low mass-damping,” *J Fluid Struct*, vol. 13, no. 7, pp. 813–851, 1999.

[105] F. Flemming and C. H. K. Williamson, “Vortex-induced vibrations of a pivoted cylinder,” *J Fluid Mech*, vol. 522, pp. 215–252, 2005.

[106] S. Mittal, “Lock-in in vortex-induced vibration,” *J Fluid Mech*, vol. 794, pp. 565–594, 2016.

[107] S. Shukla, R. N. Govardhan, and J. H. Arakeri, “Flow over a cylinder with a hinged-splitter plate,” *J Fluid Struct*, vol. 25, no. 4, pp. 713–720, 2009.

[108] C. W. Knisely, “Strouhal numbers of rectangular cylinders at incidence: a review and new data,” *J Fluid Struct*, vol. 4(4), pp. 371–393, 1990.

[109] D. Yu, K. Butler, A. Kareem, J. Glimm, and J. Sun, "Simulation of the influence of aspect ratio on the aerodynamics of rectangular prisms," *J Eng Mech-ASCE*, vol. 139, no. 4, pp. 429–438, 2012.

[110] I. Paul, K. Arul Prakash, and S. Vengadesan, "Numerical analysis of laminar fluid flow characteristics past an elliptic cylinder: A parametric study," *Int J Numer Method H*, vol. 24, no. 7, pp. 1570–1594, 2014.

[111] B. Liu, A. M. Hamed, Y. Jin, and L. P. Chamorro, "Influence of vortical structure impingement on the oscillation and rotation of flat plates," *J Fluid Struct*, vol. 70, pp. 417–427, 2017.

[112] K. C. Kwok, "Turbulence effect on flow around circular cylinder," *J Eng Mech-ASCE*, vol. 112, no. 11, pp. 1181–1197, 1986.

[113] R. Gopalkrishnan, "Vortex-induced forces on oscillating bluff cylinders," 1993, (No. WHOI-92-38). Woods Hole Oveanographic Institution MA.

[114] Y. Jin, I. Hayat, and L. P. Chamorro, "Modulation of aerodynamic force on a 2d elliptic body via passive splitter pitching under high turbulence," *J Fluid Struct*, vol. 74, pp. 205–213, 2017.

[115] J. Zhou, R. J. Adrian, S. Balachandar, and T. Kendall, "Mechanisms for generating coherent packets of hairpin vortices in channel flow," *J Fluid Mech*, vol. 387, pp. 353–396, 1999.

[116] Y. Wu and K. T. Christensen, "Population trends of spanwise vortices in wall turbulence," *J Fluid Mech*, vol. 568, pp. 55–76, 2006.

[117] M. S. Triantafyllou, G. S. Triantafyllou, and R. Gopalkrishnan, "Wake mechanics for thrust generation in oscillating foils," *Phys Fluids*, vol. 3, no. 12, pp. 2835–2837, 1991.

[118] W. Tian, A. Bodling, H. Liu, J. C. Wu, G. He, and H. Hu, "An experimental study of the effects of pitch-pivot-point location on the propulsion performance of a pitching airfoil," *J Fluid Struct*, vol. 60, pp. 130–142, 2016.

[119] Y. Jin and L. P. Chamorro, "Passive pitching of splitters in the trailing edge of elliptic cylinders," *J Fluid Mech*, vol. 826, pp. 363–375, 2017.

[120] C. Norberg, "Flow around rectangular cylinders: pressure forces and wake frequencies," *J Wind Eng Ind Aerodyn.*, vol. 49(1), pp. 187–196, 1993.

[121] A. M. Hamed, Y. Jin, and L. P. Chamorro, "On the transient dynamics of the wake and trajectory of free falling cones with various apex angles," *Exp Fluids*, vol. 56(11), pp. 1–10, 2015.

[122] G. M. Ozkan, E. Firat, and H. Akilli, “Control of vortex shedding using a screen attached on the separation point of a circular cylinder and its effect on drag,” *J Fluids Eng*, vol. 139, no. 7, p. 071107, 2017.

[123] Y. Jin and L. P. Chamorro, “On the dynamics of three-dimensional slung prisms under very low and high turbulence flows,” *J Fluid Mech*, vol. 816, pp. 468–480, 2017.

[124] Y. Jin, S. Ji, and L. P. Chamorro, “Spectral energy cascade of body rotations and oscillations under turbulence,” *Phys Rev E*, vol. 94, no. 6, p. 063105, 2016.

[125] K. Bai and J. Katz, “On the refractive index of sodium iodide solutions for index matching in piv,” *Exp Fluids*, vol. 55, pp. 1–6, 2014.

[126] C. Lin and W. Glendening, “Large eddy simulation of an inhomogeneous atmospheric boundary layer under neutral conditions,” *J. Atmos. Sci.*, vol. 59, pp. 2479–2497, 2002.

[127] J.-C. Lin, Y. Yang, and D. Rockwell, “Flow past two cylinders in tandem: instantaneous and averaged flow structure,” *Journal of Fluids and Structures*, vol. 16, no. 8, pp. 1059–1071, 2002.

[128] M. Y. Younis, M. M. Alam, and Y. Zhou, “Flow around two non-parallel tandem cylinders,” vol. 28, no. 12, p. 125106, 2016.

[129] B. Liu, A. M. Hamed, and L. P. Chamorro, “On the kelvin–helmholtz and von kármán vortices in the near-wake of semicircular cylinders with flaps,” *J. of Turbul.*, vol. 19, no. 1, pp. 61–71, 2018.

[130] I. Khabbouchi, H. Fellouah, M. Ferchichi, and M. S. Guellouz, “Effects of free-stream turbulence and reynolds number on the separated shear layer from a circular cylinder,” *J Wind Eng Ind Aerodyn.*, vol. 135, pp. 46–56, 2014.

[131] L. Chen, “An integral approach for large deflection cantilever beams,” *Int J Nonlin Mech*, vol. 45, no. 3, pp. 301–305, 2010.

[132] M. P. Païdoussis, S. J. Price, and E. De Langre, *Fluid-structure interactions: cross-flow-induced instabilities.* Cambridge University Press, 2010.

[133] J. E. Slater, “Aeroelastic instability of a structural angle section,” Ph.D. dissertation, University of British Columbia, 1969.

[134] R. D. Blevins, *Flow-induced vibration.* New York, NY (USA); Van Nostrand Reinhold Co., Inc., 1990.